

SMART
DEPLOYABLE
SPACE
STRUCTURES

Thomas Sinn

Doctoral Thesis

Glasgow, 2016

This thesis is the result of the author's original research. It has been composed by the author and has not been previously submitted for examination which has led to the award of a degree.

The copyright of this thesis belongs to the author under the terms of the United Kingdom Copyright Acts as qualified by University of Strathclyde Regulation 3.50.

Due acknowledgement must always be made of the use of any material contained in, or derived from, this thesis.

Signed:

A handwritten signature in black ink, appearing to be 'J. H. ...', written over a light grey circular stamp or watermark.

Date: 21st of August 2016

Preface

The work presented in this thesis was carried out at the Department of Mechanical and Aerospace Engineering of the University of Strathclyde between October 2010 and August 2016.

I thank my supervisor Prof. Massimiliano Vasile for his guidance, continuous support and the encouragement to be involved in several experiments (REXUS12 Suaineadh, REXUS13/15: StrathSat-R and BEXUS16's iSEDE) and studies (NIAC Space Based Solar Power, UK Space Agency Hybrid Cube Satellite Propulsion and the WISCER inflatable antenna experiment). A big thank you also to my second supervisor Prof. Colin McInnes for his encouraging talks and his extensive knowledge on advanced concepts.

During my PhD I had the great opportunity to be the team leader of the REXUS12 Suaineadh experiment. I would like to thank my team mates Malcolm McRobb from the University of Glasgow, Adam Wujek, Jerker Skogby, Fredrik Rogberg, Menghi Zhang and Yunyi Wang from KTH in Stockholm as well as Johannes Weppler from the University of Stuttgart for their amazing work to get the experiment ready to fly on a sounding rocket in March 2012. I would also like to thank Fredrik Rogberg, my brother Michael Sinn and Jeremy Molina that they came with me to search for the lost experiment in August 2012.

I also would like to thank all the team members of the REXUS13/REXUS15 StrathSat-R team which did an amazing job to launch the SAM deployable into microgravity. Thank you very much Ruaridh Clark, Nathan Donaldson, Iain Dolan, Daniel Garcia Yarnoz, Christopher Lowe, Thomas Parry, Charlotte Bewick and Russell Bewick.

A big thank you also goes to the BEXUS16 iSEDE team whose hard work made it possible to launch an inflatable adaptive satellite with disaggregated electronics on a

stratospheric balloon in October 2013. Thank you very much Tiago Queiroz, Frazer Brownlie, Larissa Leite, Andrew Allan, Jonathan Gillespie and Adam Rowan.

Being involved in three sounding rocket or stratospheric balloon experiments was an amazing experience with many useful lessons learned. I would like to thank the organisers from the REXUS/BEXUS programme organisers, the European Space Agency (ESA), the Deutsche Zentrum für Luft- und Raumfahrt (DLR) and the Swedish National Space Board (SNSB), for giving us the opportunity to test our ideas in a space like environment. A special thank you to the head of the programme Natacha Callens (ESA) our payload managers Mark Fittock (DLR), Mark Uitendaal (SSC), Mikael Inga (SSC) and Alexander Schmidt (DLR) as well as the REXUS/BEXUS YGTs Adam Lambert (2010), Paul Stevens (2011), Alex Kinnaird (2012) and Nora Newie (2013).

All these experiments would have not been possible without the outstanding support of Jim Dorothy of the Mechanical workshop and Thomas Canny from the Department of Physics workshop. Thank you for your patients of letting us borrow the necessary tools and use the testing facilities.

A big thank you to all of my colleagues at the University of Strathclyde for their continuous support and help: Andreas Borggräfe, Fabrizio Pescetelli, Willem van der Weg, Daniel Garcia Yarnoz, Juan Manuel Romero Martin, Marcel Düring, Alison Gibbings, Simone Alicino, Luca Masi, Massimo Veterisano, Manpreet Puri, Romain Wuilbercq, Charlotte Lücking, Russell Bewick, Jeannette Heilgers, Joan Pau Sanchez Cuartielles, Craig McLean, Daniele Pagnozzi, Nicolas Thiry, Chiara Tardiolo, Juan Romero Martin, Alessandro Mogavero and Steven Owens.

Last but not least I would like to thank my family for their continuous support and their patience over the three and something year that I spent on exploring the depths of the deployable space structures field.

Glasgow, August 2016

Thomas Sinn

**“Instead of thinking
outside the box,
get rid of the box”**

Deepam Chopra
(Physician, Writer)

Abstract

Nowadays, space structures are often designed to serve only a single objective during their mission life, examples range from solar sail for propulsion over shields for protection to antennas and reflectors for communication and observation. By enabling a structure to deploy and change its shape to adapt to different mission stages, the flexibility of the spacecraft can be greatly increased while significantly decreasing the mass and the volume of the system. Inspiration was taken from nature. Various plants have the ability to follow the sun with their flowers or leaves during the course of a day via a mechanism known as heliotropism. This mechanism is characterized by the introduction of pressure gradients between neighboring motor cells in the plant's stem, enabling the stem to bend. By adapting this bio-inspired mechanism to mechanical systems, a new class of smart deployable structures can be created. The shape change of the full structure can be significant by adding up these local changes induced by the reoccurring cell elements. The structure developed as part of this thesis consists of an array of interconnected cells which are each able to alter their volume due to internal pressure change. By coordinated cell actuation in a specific pattern, the global structure can be deformed to obtain a desired shape. A multibody code was developed which constantly solves the equation of motion with inputs from internal actuation and external perturbation forces. During the inflation and actuation of the structure, the entities of the mass matrix and the stiffness matrix are changed due to changing properties of the cells within the array based on their state and displacement. This thesis will also give an overview of the system architecture for different missions and shows the feasibility and shape changing capabilities of the proposed design with multibody dynamic simulations. Furthermore, technology demonstrator experiments on stratospheric balloons and sounding rockets have been carried out to show the applicability and functionality of the developed concepts.

Contents

Preface	iii
Abstract	vi
List of Figures	ix
List of Symbols and Abbreviations	xiv
1 Introduction.....	1
1.1 Motivation	1
1.2 State of the Art	2
1.3 Proposed Approach	3
1.4 Expected Results.....	4
1.5 Structure of the Thesis	5
1.6 Publications & Presentations.....	6
2 Deployable & Smart Structures.....	7
2.1 Deployable Structures	7
2.1.1 Applications	8
2.1.2 Technologies.....	13
2.2 Shape Changing Structures.....	25
2.2.1 Adaptive Materials.....	25
2.2.2 Smart Structural Concepts	28
2.3 Synopsis	32
3 Bio-inspired Smart Structures	34
3.1 Inspired by Nature	34
3.1.1 Nature's Deployables.....	34
3.1.2 Nature's Shapeshifters	36
3.2 Mechanical Analogue	38

3.2.1	Deployable Cells	39
3.2.2	Shape Changing Structure.....	39
3.2.3	Organism architecture inspired structures.....	40
3.2.4	Self-folding Origami Structure	41
3.3	Discretization and Modelling	45
3.3.1	Property Matrices.....	51
3.3.2	Adaptive Global Matrices	60
3.3.3	Forces.....	69
3.4	Control	79
4	Simulations and Experiments.....	85
4.1	Large Smart Structure Assembly in Space	85
4.2	Application I: Reflector & Concentrator	92
4.2.1	Concept and System Design.....	92
4.2.2	Simulation	96
4.2.3	Experiment: StrathSat-R	112
4.3	Application II: Smart Beam Elements in Space.....	128
4.3.1	Concept and System Design.....	128
4.3.2	Simulation	128
4.3.3	Experiment: iSEDE.....	138
5	Conclusions and Future Work	150
5.1	Discussion	150
5.2	Conclusions.....	150
5.3	Future Work	151
	Appendix A - Silicon Rubber Benchtest	153
	Bibliography	155

List of Figures

Figure 1-1: Artist impression of asteroid deflection using surface sublimation.....	1
Figure 2-1: ISS photographed from departing space shuttle	8
Figure 2-2: Deployed Harris rigid rib antenna	9
Figure 2-3: Deployed JWST heat shield in August 2014	11
Figure 2-4: NASA JPL's sunflower shaped star shade	11
Figure 2-5: Pressurized volume per astronaut over mission duration	12
Figure 2-6: Deployed decelerator test specimen of NASA's LDSD project.....	13
Figure 2-7: Deployed AstroMesh reflector	14
Figure 2-8: Deployed Harris TerreStar reflector.....	14
Figure 2-9: Drawing of two cells inflated by electrostatic forces	18
Figure 2-10: Inflatable Antenna Experiment (IAE)	19
Figure 2-11: Deployment test of inflatable airbags of Mars Pathfinder.....	20
Figure 2-12: Inflation of Bigelow BEAM module attached to ISS.....	21
Figure 2-13: Cell Residual Air Inflation in Vacuum Chamber	22
Figure 2-14: Four legged soft robot.....	29
Figure 2-15: RC controlled smart airship.....	30
Figure 2-16: Harvard and MIT's self-folding sheet	30
Figure 2-17: MIT's Robot pebbles creating programmable matter.....	31
Figure 2-18: Harvard's 4D printed orchid actuated in water.....	31
Figure 2-19: SRI International/DARPA specific energy chart	32
Figure 3-1: Deploying leaves of a legume plant.....	35
Figure 3-2: Eclosion process of a dragonfly	35
Figure 3-3: Arctic poppies moving their head towards the sun.....	37
Figure 3-4: Functionality of motor cells.....	38
Figure 3-5: a) Pre-deformed membrane b) Shape change of flat membrane	40
Figure 3-6: Schematic of cellular principle	41
Figure 3-7: Crease pattern and corresponding sculpture.....	42

Figure 3-8: Static 2D plot of actuated cell array forming a 180 degree fold.....	43
Figure 3-9: Height of 180 degree folds.....	44
Figure 3-10: LS-DYNA simulation parameters	47
Figure 3-11: Inflation of single cell (LS-DYNA™ simulation).....	47
Figure 3-12: Schematic of discretisation of cells.....	49
Figure 3-13: Modelling of cells:	50
Figure 3-14: Degrees of Freedom of a beam in local coordinates.....	52
Figure 3-15: Cell Coordinate System and Orientation.....	55
Figure 3-16: Numbering of cells and nodes	56
Figure 3-17: Rotation Axes and Angles	57
Figure 3-18: Schematic of cell inflation.....	60
Figure 3-19: Length of beam depending on gas mass inflow	62
Figure 3-20: Moment of inertia: cross section geometric drawing.....	63
Figure 3-21: Moment of Inertia in x and y	65
Figure 3-22: Modulus of elasticity and shear modulus	66
Figure 3-23: Single inflated cell	66
Figure 3-24: Radius of cell over gas mass inflow	67
Figure 3-25: First cell eigenfrequency over gas mass inflow.....	68
Figure 3-26: Force model of one cell.....	70
Figure 3-27: Inflated 11x11x2 cell array.....	72
Figure 3-28: Displacement of x and y and z-position	72
Figure 3-29: Top central 9x9 array of deploying structure	74
Figure 3-30: Displacement plot of actuated structure.....	75
Figure 3-31: Thermal force distribution in model.....	76
Figure 3-32: External force application areas at specific instance.....	79
Figure 3-33: Schematic of spherical concentrator.....	80
Figure 3-34: z-position error for each of the 81 cells at start.....	81
Figure 3-35: Development of error over 100 control loops	82
Figure 3-36: z-Position error for each of the 81 cells.....	82

Figure 3-37: Actuation of cells for at the end of control cycle	83
Figure 3-38: Position of all cell normals at the focal point ($r_{focal}=5m$)	83
Figure 4-1: Schematic of deployment option 1 with the release of colonies.....	86
Figure 4-2: Schematic of deployment option 2 with the release of colonies.....	87
Figure 4-3: 3D realization of one cell connected to pressure source.....	88
Figure 4-4: Single path vs. tree path vs. full path.....	89
Figure 4-5: Required gas units and valves for each path design.....	90
Figure 4-6: Artist Impression of SPS-ALPHA	94
Figure 4-7: Schematic of functionality of space solar power space segment	94
Figure 4-8: Schematic of rigid solar array / power transmission system	95
Figure 4-9: a) Inflated 10x10x2 cell array.....	98
Figure 4-10: Central layer wireframe plot	99
Figure 4-11: Displacement of nodes during inflation in all directions	100
Figure 4-12: Actuation of cells.....	101
Figure 4-13: Shape change of array	101
Figure 4-14: Focal area of array.....	101
Figure 4-15: Path of rays in parabolic concentrator.....	102
Figure 4-16: z-position error of 81 cells before shape control.....	103
Figure 4-17: Development of error over 100 control loops ($F/D = 0.66$)	104
Figure 4-18: z-position error of 81 cells after shape control.....	105
Figure 4-19: Actuation of cells for at the end of control cycle	105
Figure 4-20: Position of all cell normals at the focal point	106
Figure 4-21: Sketch with external forces of satellite passing asteroid.....	107
Figure 4-22: Satellite flying into the shadow of the asteroid.....	108
Figure 4-23: Mean position of the spacecraft over time.....	109
Figure 4-24: Mean velocity of the spacecraft over time	109
Figure 4-25: Position of spacecraft nodes (S/C CS).....	110
Figure 4-26: Rel. position change at entering shadow (S/C CS).....	111
Figure 4-27: Rel. position change at leaving shadow (S/C CS).....	111

Figure 4-28: Cut-through schematic of StrathSat-R deployable SAM	113
Figure 4-29: Actuator placement of Self-inflating Adaptive Membrane.....	114
Figure 4-30: Prototype of 5x2cell inflatable smart structure	115
Figure 4-31: 3D printed mould (top) used to cast 4x2x1 cell structures (bottom).....	117
Figure 4-32: Two fully inflated hyperelastic cells	118
Figure 4-33: Inflated 4x2x1 cell array.....	119
Figure 4-34: Inflatable cellular structures	120
Figure 4-35: Miura-ori folding pattern on flat sheet of paper	121
Figure 4-36: a) Schematic of star folding pattern and b) Benchtest structure.....	121
Figure 4-37: Schematic of flower folding pattern	122
Figure 4-38: Deployment of inflating membrane (blue) out from flat case.....	123
Figure 4-39: Radius of structure during inflation process from flat initial state	124
Figure 4-40: Deployment of inflating membrane.....	124
Figure 4-41: Radius of structure during packaging and inflation process.....	125
Figure 4-42: StrathSat-R's ejected cube satellite	126
Figure 4-43: PICARD's inflated conical helix antenna.....	127
Figure 4-44: Position over velocity for orbiting structure	129
Figure 4-45: Polar plot of orbiting element structure	129
Figure 4-46: Relation between reference coordinate system.....	130
Figure 4-47: a) Beam element.....	131
Figure 4-48: Difference to perfect LEO orbit for x-beam. (S/C CS).....	132
Figure 4-49: Displacement of nodes x-beam. (S/C CS).....	132
Figure 4-50: Difference to perfect LEO orbit for y-beam. (S/C CS)	133
Figure 4-51: Displacement of nodes y-beam. (S/C CS).....	133
Figure 4-52: Difference to perfect LEO orbit for z-beam. (S/C CS).....	134
Figure 4-53: Displacement of nodes z-beam. (S/C CS)	134
Figure 4-54: Polar plot of relative displacement in meters (x-axis beam)	136
Figure 4-55: Polar plot of relative displacement in meters (y-axis beam)	136
Figure 4-56: Polar plot of relative displacement in meters (z-axis beam).....	137

Figure 4-57: iSEDE experiment in BEXUS gondola.....	139
Figure 4-58: Inflating iSEDE Mylar/Kapton cell in vacuum chamber.....	140
Figure 4-59: Principle functionality of a soft robotic actuator	141
Figure 4-60: Deformation of actuated soft robotic actuator	142
Figure 4-61: Displacement graph of actuated soft robotic actuator	142
Figure 4-62: Actuation of satellites (soft robotic actuator = yellow lines).....	143
Figure 4-63: Actuator element	144
Figure 4-64: Full iSEDE experiment.....	145
Figure 4-65: Top cell of satellite with pump/pressure sensor unit	146
Figure 4-66: Fully deployed 1x2x10 array (iSEDE with symmetry)	147
Figure 4-67: Vertical displacement of iSEDE softrobotic actuator	148

List of Symbols and Abbreviations

Roman Symbols

A	Area (Beam Element)
A_{cell}	Area (Cell)
A_D	Drag Area
C_D	Drag Coefficient
C_{TE}	Coefficient of Thermal Expansion
D	Damping Matrix
d_{MB}	Inflated Diameter (Mylar Balloon)
E	Modulus of Elasticity (Beam Element)
E_{mat}	Modulus of Elasticity (Hyperelastic Material)
e	Error (PID)
f	Focal Point
F_{act}	Actuation Force
$F_{atmdrag}$	Force caused by Atmospheric Drag
F_{cell}	Force in each Cell
$F_{centrifugal}$	Centrifugal Force
$F_{diffgravity}$	Force caused by Differential Gravity
F_{global}	Global Force Distribution
F_{ext}	External Force
F_{int}	Internal Force
F_{inf}	Inflation Force

F_{node}	Nodal Force
G	Shear Modulus (Beam Element)
G_{mat}	Shear Modulus (Hyperelastic Material)
G_C	Gravity Constant
I	Moment of Inertia (Beam Element)
I_{cell}	Cell Moment of Inertia
i	Index (coordinate (x, y or z) or running number (1,2,3,...))
J	Torsion Moment of Area (Beam Element)
\mathbf{K}	Stiffness Matrix
\mathbf{K}_{cube}	Stiffness Matrix of one cubic element assembled of 8 beams
K_d	Derivative Gain (PID controller)
K_i	Integral Gain (PID controller)
K_p	Proportional Gain (PID controller)
\mathbf{K}_{rot}	Rotated Stiffness Matrix
L	Length (Beam Element)
\mathbf{M}	Mass Matrix
\mathbf{M}_{beam}	Mass (Beam Element Matrix)
m_{beam}	Mass (Beam Element Scalar)
m_{body}	Mass of Attracting Body
m_{cell}	Cell Mass
$m_{cellstruct}$	Structural Cell Mass
m_{gas}	Mass of (Inflation) Gas
m_{node}	Mass of Node

n_{cell}	Number of Cells
p_{cell}	Cell Pressure
$\ddot{\mathbf{q}}$	Acceleration
$\dot{\mathbf{q}}$	Velocity
\mathbf{q}	Position / Rotation
\mathbf{Q}	Rotation Matrix
R	Boltzmann Constant
r_{beam}	Beam Radius
r_{cell}	Cell Radius
r_{cello}	Outer Cell Radius
r_{MB}	Uninflated Radius (Mylar Balloon)
$\mathbf{r}_{body-node}$	Distance of Node to Attracting Body
r_{sphere}	Radius to Focal Point of Sphere
T_{cell}	Cell Temperature
$t_{cellwall}$	Thickness of Cell Wall
t_{MB}	Inflated Thickness (Mylar Balloon)
t	Time
V_{cell}	Cell Volume
$V_{cellstruct}$	Structural Cell Volume (Cell Walls)
v	Velocity of Moving Structure
x	Coordinate x
y	Coordinate y
z	Coordinate z

Greek Symbols

α	Rotation Angle around x-Axis
β	Rotation Angle around y-Axis
γ	Rotation Angle around z-Axis
ε	Strain
ρ	Density
σ	Stress
τ	Time Interval (PID)

Abbreviations

AFC	Active fibre composites
BEAM	Bigelow Expandable Activity Module
BEXUS	Balloon Experiments for University Students
CIRA	COSPAR International Reference Atmosphere
COSPAR	Committee on Space Research
CCG	Cold Gas Generator
CFRP	Carbon Fibre Reinforces Plastics
CTM	Collapsible Tube Masts
CS	Coordinate System
D/F	Diameter to Focal Length Ratio
DARPA	Defence Advanced Research Projects Agency (US)
DLR	Deutsches Zentrum für Luft- und Raumfahrt

EAP	Electroactive Polymers
EMC	Electromagnetic Compatibility
ESA	European Space Agency
FEA	Finite Element Analysis
FEM	Finite Element Method
GEO	Geostationary Orbit
IAE	Inflatable Antenna Experiment (NASA)
ICM	Inflatable Capture Mechanism
IRVE	Inflatable Re-entry Vehicle Experiment
iSEDE	Inflatable Satellite Encompassing Disaggregated Electronics
ISS	International Space Station
JAXA	Japan Aerospace Exploration Agency
JPL	Jet Propulsion Laboratory (NASA)
JWST	James Webb Space Telescope
LEO	Low Earth Orbit
LDSD	Low-Density Supersonic Decelerator
MAIT	Manufacturing, Assembly, Integration and Testing
MEMS	Microelectromechanical Systems
NASA	National Aeronautics and Space Administration
NIAC	NASA's Innovative Advanced Concepts
PID	Proportional-Integral-Derivative (Controller)
RC	Radio Controlled
REXUS	Rocket Experiments for University Students

RTG	Radioisotope Thermoelectric Generator
SAM	Self-inflating Adaptive Membrane
SAR	Synthetic Aperture Radar
SBSP	Space Based Solar Power
S/C	Spacecraft
SMA	Shape Memory Alloys
SMC	Shape Memory Composites
SMP	Shape Memory Polymers
SNSB	Swedish National Space Board
SRP	Solar Radiation Pressure
SSC	Swedish Space Corporation
STEM	Storage Tubular Extension Member
TRL	Technology Readiness Level
UV	Ultra Violet
WISCER	Wideband Ionospheric Sounder CubeSat Experiment

Chapter I

Introduction

The introduction chapter begins with the presentation of the motivation of this work, the description on the origin of the idea and the need for smart deployable structures. The motivation section is followed by a description on the state of the art giving a short overview on the already existing technologies and systems. The required work and the description of the different chapters are outlined within the structure of the thesis section. The expected results have a dedicated section within this introduction chapter preparing the reader for the goals of this research work. The chapter concludes with a summary on the published work related to the research undertaken in this thesis.

1.1 Motivation

The initial goal of this investigation was to find a solution of deploying very large concentrators in space capable of focusing the sun's energy. The need of these extra-large concentrators was revealed during Strathclyde's ongoing work on asteroid deflection which requires large amounts of energy over a long period of time.

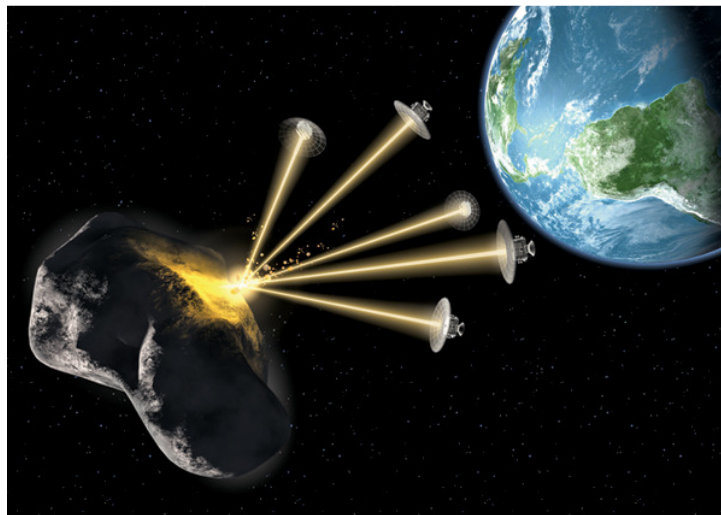


Figure 1-1: Artist impression of asteroid deflection using surface sublimation via lasers from spacecraft formation called Laser Bees [1]

Figure 1-1 shows an artist impression of the asteroid deflection satellites Laser Bees [1]. The sun's energy is focused to power a laser that is sublimating the surface of the asteroid and thereby changing the trajectory of it [2]. For this application there is an urgent need to provide very large deployable concentrators capable of altering their shape to adjust their focal point depending on the position of the sun and the asteroid to ensure that always the maximum of the sun's energy is collected to power the sublimating laser [3],[4].

By assessing also other possible applications, the following requirements were formulated that should be fulfilled by the developed structure:

- The structure shall be both deployable as well as smart. The developed design should be scalable and applicable to a large variety of applications ranging from large deformable space structures down to medical devices like blood vessel opening stents.
- The structure should be stored at a fraction of its final configuration volume and therefore has to be very lightweight. The used deployment concept should be reliable, simple and have a failsafe methodology meaning that a failure of a few components will not lead to a total failure of the entire structure.
- The smart aspect of the structure shall give the deployed structure the capability to change its shape once deployed and thereby forming a versatile smart structure. Another requirement that the developed structure had to fulfil is that the smart structure should only consume energy during shape alteration and not during maintaining the deformed shape.

1.2 State of the Art

The literature review showed that there is currently no structure or system that fulfils all the requirements. Some of the stated requirements are fulfilled by a number of the existing concepts that then are inevitably failing the other requirements.

In space technology, there is an ever increasing need for deployable structures; the most popular deployable methods for antennas or concentrators are deployment via complicated mechanisms or the release of stored energy. These structures already have a good area to mass ratio today but are often custom designed for one application. They are usually form a stiff structure once deployed with virtually no scope for shape adaption.

The requirement of the shape changing structure might be fulfilled by adaptive materials and smart structures. The existing concepts for very large smart structures are usually limited either due to their small actuation length like piezoelectric, their high mass like magnetostrictors or their temperature dependency like SMAs (Shape Memory Alloys).

All the current technologies lack the combination of a system that is capable of large expansion and can therefore be stored in a small stowage volume while being able to change their shape once expanded.

1.3 Proposed Approach

As outlined in the summary of the state of the art, a new technology needs to be developed that is able to fulfil the given objectives the smart controllable space structure.

Thinking outside the box was required and therefore inspiration was taken from nature with its millions of year of development experience. The original work of the thesis starts with the creation of a mechanical analogue that is mimicking the shape changing behaviour of plants that follow the sun during the pass of a day. The developed mechanical structure consists of hundred of cells and is deployed using inflation (due to its advantage of small storage volume). The structure is capable of shape alteration using pressure variations between the cells. This pressure change is facilitated through a pressure sources, MEMS (Microelectomechanical System) pumps and valves between the cells.

Initially, a commercial FEA (Finite Element Analysis) software package was used to simulate the deployment but the developed concept was very computationally expensive already for small numbers of cells. In order to make the simulation of the actuation as well as the influence of perturbing factors possible, an own standing code needed to be developed. This code has as its centre piece the equation of motion that is continuously solved to obtain the positions and velocities. The mass, stiffness and damping matrix are obtained by using beam elements that are assembled in cubes arranged like biological cells. The properties of these beam elements vary depending on the current inflation status of the cells. The inflation, actuation as well as the external forces enabling the structure to deform. A PID controller is used to optimize the shape of the structure.

The concept and simulation code was then applied to a number of significant cases like an orbiting large smart beam element and a shape adjusting concentrator for the asteroid deflection mission outlined in the motivation as well as a SBSP (Space Based Solar Power) satellite.

Experiments were carried out to validate the concept as well as the simulations. The sounding rocket experiment StrathSat-R proved that the deployment in space using trapped air worked of a free flying shape changing structure worked. Furthermore, during the experiment's MAIT (Manufacturing, Assembly, Integration & Test) important design lessons and mechanical properties were obtained. The second experiment iSEDE was launched on a stratospheric balloon and proved that the concept of the disaggregated electronic and communication over the surface of an all inflatable shape changing satellite worked.

1.4 Expected Results

The expected result of this work is the development of a structure that fulfils all the requirements stated in the motivation section. The structure shall be reliably deployed and its shape shall be changed to adapt to the environment without the continuous need for energy to hold its shape. The performance of the structure shall be demonstrated

with the developed code simulating different space applications with all contributing factors. Benchtest experiments including stratospheric balloon and rocket experiments shall show the capability of the developed systems and collect important lessons learned to mature the design of the smart deployable structure.

Another expected outcome of this work that is less space oriented than the original source of the motivation is the development of a kind of programmable matter. The tools and simulations shall be scalable to achieve the possibility to reduce the size of the elements to microscopic levels which has currently only limitation in regards to fabrication. If then hundreds or thousands of these smart elements are grouped and joined together, a programmable sheet that can self fold itself can be achieved. This programmable matter has its applications in almost every field ranging from medical applications like stents or medication deliverable devices over construction like adjusting covers redirecting the sunlight to art with the possibility to create active sculptures.

1.5 Structure of the Thesis

The scope of this thesis as well as the origin of the idea behind the developed concepts is outlined in **Chapter I**.

Chapter II provides a literature review on existing technologies and materials to build deployable and/or shape changing structures for space as well as terrestrial applications.

Chapter III presents the biological concept of shape changing plants and the developed structure mimicking this concept. A multibody code was developed that enables the deployment and actuation simulation of large shape changing space structures.

Chapter IV displays the most interesting applications of the smart deployable structures concept, the system design, the simulation with the developed code as well as

the experimental campaign (including sounding rocket and stratospheric balloon experiments) is described.

Chapter V shows the conclusions of the thesis and gives recommendations for future work.

1.6 Publications & Presentations

The following subchapters will give a summary on the work that was published during and with the work that has been done during this PhD. The subsection is divided into journal publication (2 in total), conference papers (22 in total), official reports (5 in total) and presentations either poster or oral without a paper (24 in total).

The two journal papers published as part of the research outlined in this thesis are currently (August 2016):

T. Sinn, D. Hilbich, M. Vasile ‘Inflatable shape changing colonies assembling versatile smart space structures’, *Acta Astronautica*, volume 104, pp. 45-60, doi:10.1016/j.actaastro.2014.07.015, 2014.

H. Mao, G. Tibert, **T. Sinn**, M. Vasile ‘Post-Launch Analysis of the Deployment Dynamics of a Space Web Sounding Rocket Experiment’, *Acta Astronautica*, volume 127, pp 345–358, doi:10.1016/j.actaastro.2016.06.009, 2016.

Chapter II

Deployable & Smart Structures

There are mainly two factors which drive the costs of space craft nowadays. The first one is the launch costs which are depend highly of the size and the mass of the object being launched into space [5]. The second factor is the complexity of the spacecraft and the amount of systems are needed to fulfil the given mission tasks. This chapter has the purpose to give a state of the art overview and is therefore separated in deployables which are a mean to overcome the launcher payload restrictions and into smart structures which can decrease the complexity of a system or enable more versatile spacecrafts. The chapter shows the technologies and materials available today to built large space structures and smart structures. At the end of the chapter, a synopsis is presented showing that none of the existing technologies completely fulfils the goal of obtaining a deployable smart space structure.

2.1 Deployable Structures

The size of spacecrafts nowadays is mainly governed by launch vehicle payload dimensions. The use of deployable structures became necessary due to their low stowage and high in-orbit volume. The principle of a deployable is that they can be stored in a volume a fraction of their full size but once they arrive at their final destination they will be expanded to larger dimensions. Another option to create large structures in space would be in orbit assembly like the International Space Station (ISS). This method requires a substantial amount of subsequent rocket launches and will therefore not be discussed further.

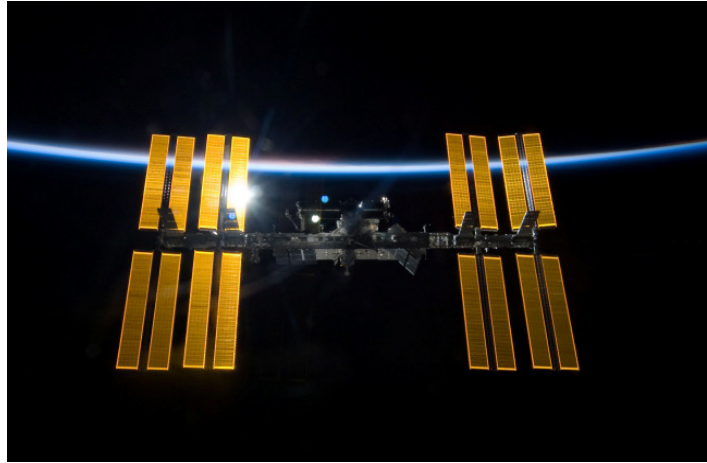


Figure 2-1: ISS photographed from departing space shuttle (source NASA)

Figure 2-1 shows the ISS with its separately launched modules assembled in orbit and deployable structures like the solar arrays.

2.1.1 Applications

Almost all of today's spacecrafts and satellites are using some sort of deployable structures, from the ISS' solar panels down to simple dipole antennas for cube satellites. Deployable structures are needed for applications such as reflectors, antennas, concentrators, solar panels, truss structures, solar and de-orbit sails, sun shields, decelerators and space stations. The following subchapters will give an overview on the need of deployable structures followed by an overview on existing technologies making these deployable structures possible.

Reflectors, Antennas and Concentrators

The most prominent applications for deployable structures are reflectors of telecommunication satellites with a usage of more than 80% today [6]. Other applications lie within power generation where the sun's energy needs to be concentrated on a solar panel to provide power to the spacecraft. Space Based Solar Power geostationary platforms [7] also require that the sunlight will be redirected and focused on an array of solar cells before the energy can be beamed down to Earth via

laser or microwaves. One application that was already mentioned in the motivation of this thesis was the use as solar concentrators for asteroid deflection missions like the Laser Bees project [1].

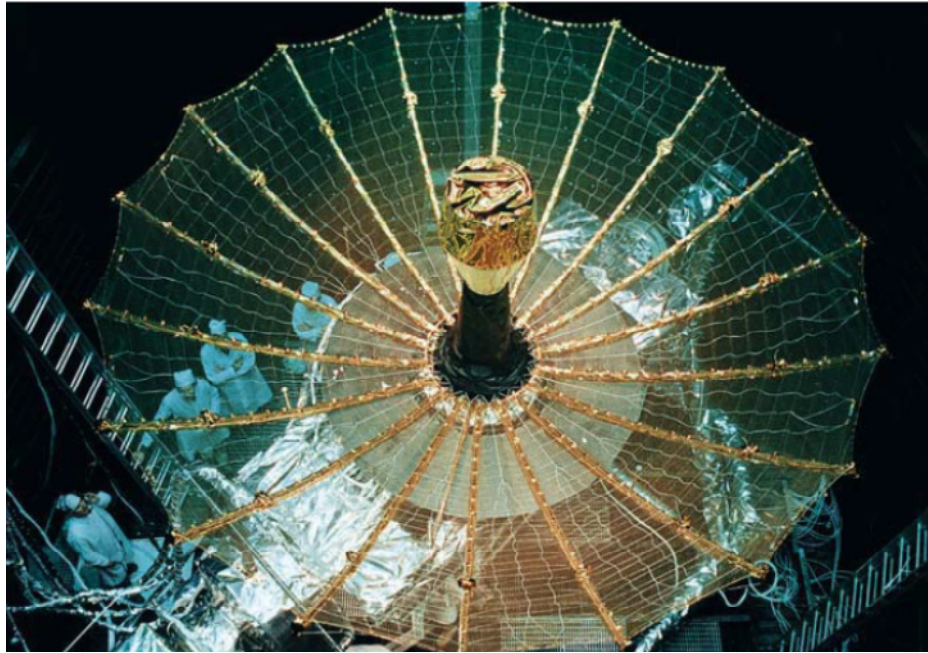


Figure 2-2: Deployed Harris rigid rib antenna for the Galileo and TDRS missions [6]

Solar Panels, Truss Structures and Appendices

Also solar arrays are often large expandable structures to ensure the required power production for the space craft, a great example is the foldable solar array of the ISS with an expanded length of 73 meters [8]. Solar panels for small to medium size applications are usually segmented and can be folded a few times to fit around the spacecraft. Bigger, thin film solar panels like the main panels of the ISS are deployed from storage canisters with the help of elongating mast or booms. These mast and booms are also used for spacecraft systems that need to be placed at a certain distance of the spacecraft to minimise disturbances on spacecraft instruments, e.g. a Radioisotope Thermoelectric Generator (RTG) that could disturb sensitive instruments on the spacecraft. A well-known example would be the magnetometers of the deep space probe Voyager 1 and 2 that left our solar system in 2013 with the achieved RTG separation to magnetometer

distance of 13m [9]. Applications like SAR or X-ray Earth imaging missions require a separation distance of a few tenths of meters between two transceivers to enable 3D imaging within the desired accuracy. Other applications that require these appendices include the deployment of instruments like magnetometers or gamma ray spectrometers, deployment booms for ion thrusters or heat rejection systems, deployment systems for dipole antennas or reflectors for mobile broadcasting [10].

Solar and De-orbit Sails

Increasing interest is given to very large lightweight structures which are increasing the area of the spacecraft for either propulsion or increasing the atmospheric drag to de-orbit faster. These spacecraft structures can be used as solar sails like the successfully flown JAXA's IKAROS solar sail with a dimension of 20m x 20m using the solar wind as a means of propulsion [11]. Other applications, especially for cube satellite applications are drag sails which are deployed after end of life of cube satellites to increase their atmospheric drag for faster de-orbiting [12]. This is an important aspect considering the increasing threat through space debris. The deployment technologies used for sail deployment are currently through booms or spinning deployment.

Sun and Star shields

Especially for missions to the inner solar system or sun observation missions' sun shields become important additional structures. Also telescopes like the James Webb Space Telescope (JWST) require very large deployable shields to decrease temperature and stray light effect on the sensitive optic. The temperature difference between the star facing hot side and cold science instrument side are 318 degrees (85°C hot side, -233°C cold side). The five layer sun shield of JWST has the dimensions of 21.197 m x 14.162 m [13] and is therefore much bigger than the available payload fairing volume available on launchers today.



Figure 2-3: Deployed JWST heat shield in August 2014 (Copyright NASA/Chris Gunn)

In 2014, NASA and JPL presented a novel design for a star shade to assist future telescopes to hunt for exoplanets orbiting around distance stars [14]. A star shade that in a deployed form has the shape of a sunflower will be positioned between the space-based telescope and the star to block its bright light. The starshade would make starlight suppression possible which makes the light coming or blocked by the exoplanet better to detect. The proposed deployment technique is a two-step system where in a first step the outside pedals that are wrapped around the central section are being released. In the next step the circular inner section gets expanded.

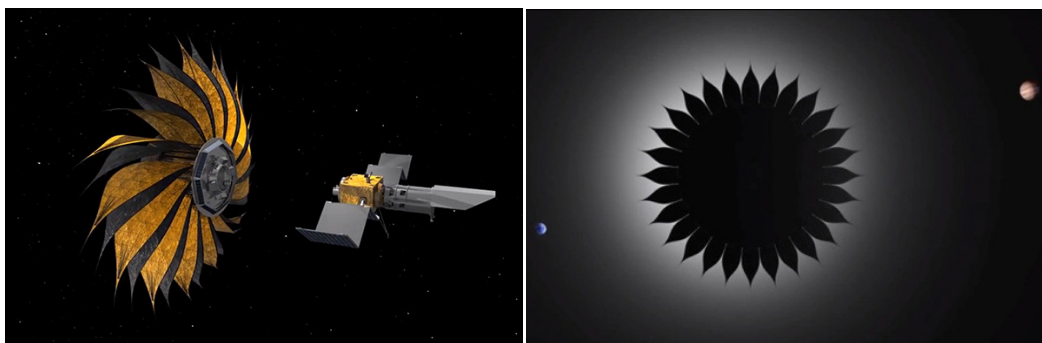


Figure 2-4: NASA JPL's sunflower shaped star shade: Artist impression of deployment (left) and placement to block starlight (right) [14].

Habitats and Space Stations

To enable a human presence in space astronauts need to be protected against the harsh space environment by providing a pressurized volume to live in and perform all mission tasks. The NASA document NASA-STD-3001 (superseding NASA-STD-3000) [15] gives guidelines on the required habitational volume depending on the mission duration. Especially longer missions require larger volumes per crewmember due to the higher importance of privacy counteracting confinement, isolation and stress that comes with long space missions [16]. Figure 2-5 shows the pressurized volume per crew member over the duration of the mission with the guidelines overlaid by data from actual space missions [17].

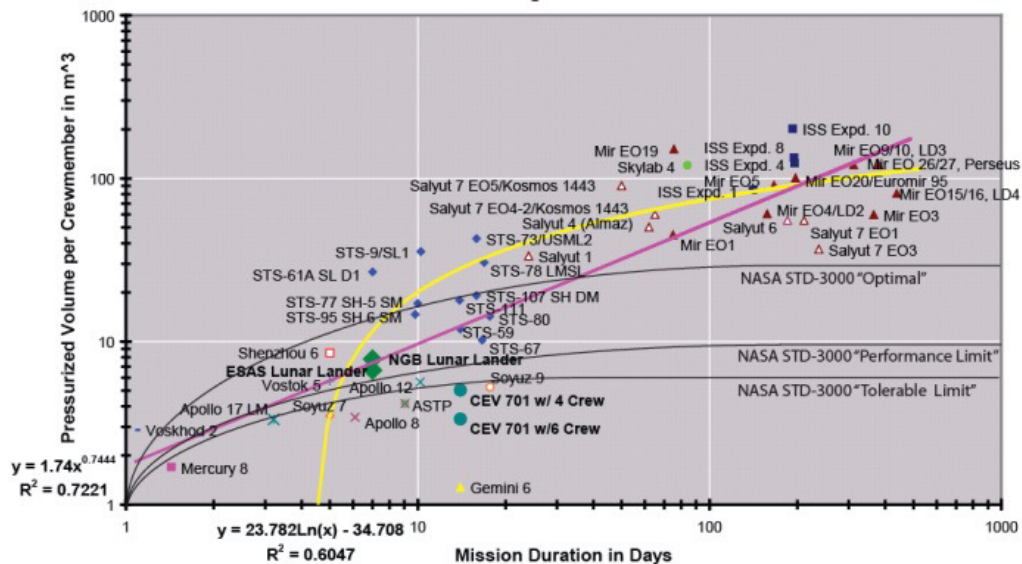


Figure 2-5: Pressurized volume per astronaut over mission duration (source [17]).

Decelerators and Balluts

Another application area that deployable structures are increasing their TRL is within the field of terrestrial and planetary decelerator systems. To land a spacecraft returning from Earth orbit or from interplanetary travel, the velocity of the spacecraft must be greatly reduced [18]. A common method to do this is the use of Earth's or the planet's atmosphere to reduce the speed by using the atmospheric drag. A large heat

resistive / ablative surface is necessary to facilitate the drag breaking. In 2014, NASA's Low-Density Supersonic Decelerator (LDSD) project performed rocket powered re-entry tests of an inflatable decelerator over Hawaii with velocities up to Mach 4. The system (2014 test specimen in Figure 2-6) is designed to land bigger and heavier payloads on Mars paving the way for future manned missions to the red planet.

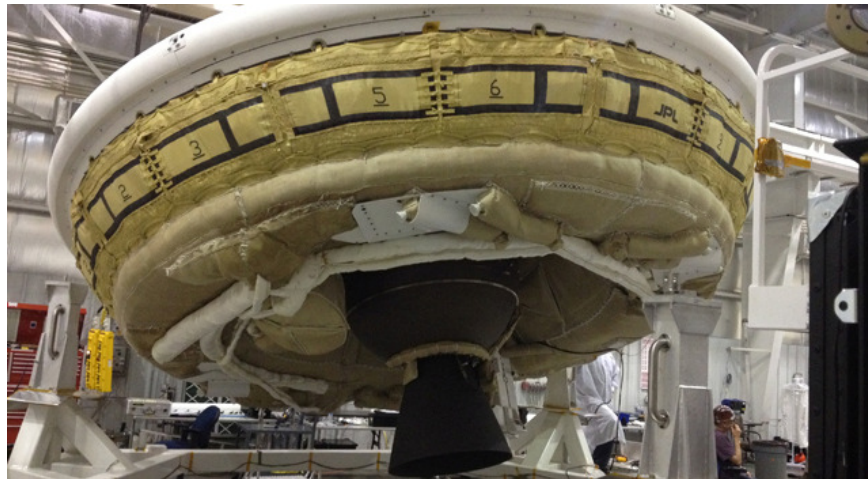


Figure 2-6: Deployed decelerator test specimen of NASA's LDSD project (source NASA/JPL-Caltech)

2.1.2 Technologies

The following chapter summarized the available technologies to deploy the space structures described in the previous chapter. The main technologies consist of umbrella deployment, expandable booms and masts, foldable shells, spinning deployable structures, tethers, electrostatic deployment as well as deployment via inflation.

Umbrella Deployment

A common deployment technology, especially for reflectors and concentrators is the umbrella deployment. The deployable structure usually consists of a rib or rod truss structure with multiple joints and hinges. During deployment the unfolding truss structure tensions the flexible surface membrane mesh depending on its application. An

example of this technology would be the AstroMesh reflector from Astro Aerospace/Northrop Grumman which is based on a tension truss concept with the deploying truss structure on its circumference [19].



Figure 2-7: Deployed AstroMesh reflector (source Northrop Grumman)

A good example for the umbrella deployment is also the Hinged-Rib Antenna from Harris Corporation (USA). In their design, the ribs are hinged along their length producing a small packaging volume.

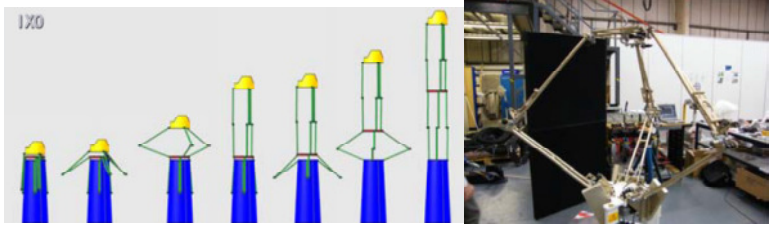
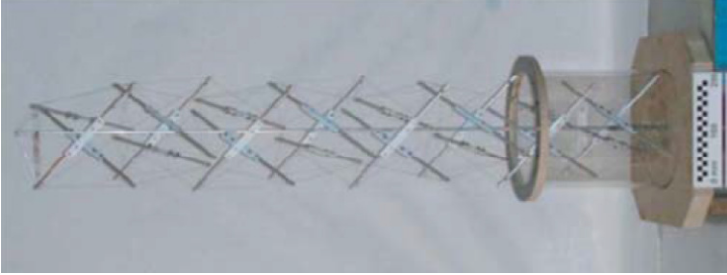
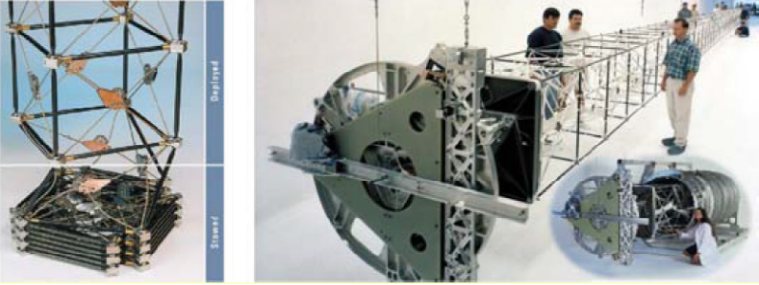


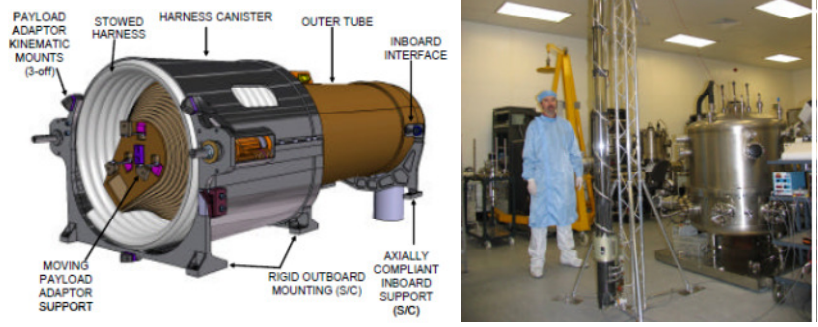
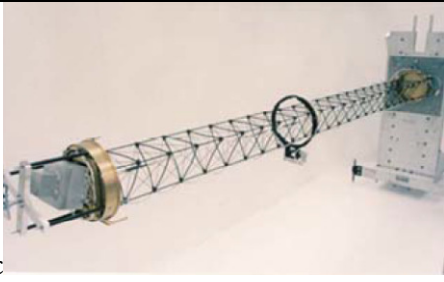
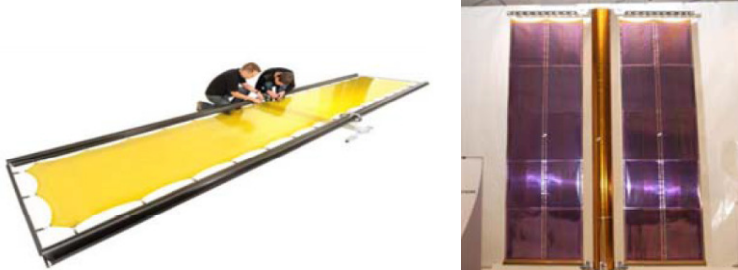

Figure 2-8: Deployed Harris TerreStar reflector (source Harris Corporation)

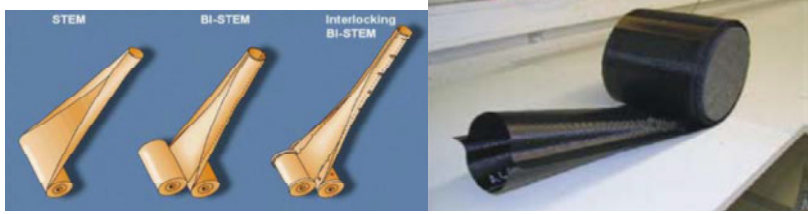
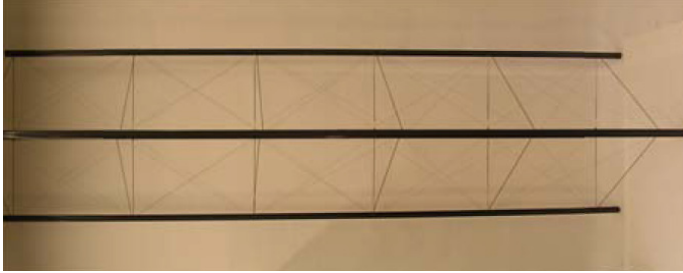
Booms and Masts

Booms and masts are deployable structure where by definition the cross section is by far smaller than the deployed length. Masts are main structural members and therefore having a higher stiffness than booms. In general booms are associated with hollow cylindrical or circular sections beams while masts are large deployable structures usually assembled in the truss type modular with multiple hinges [10]. Existing technologies for booms and masts are hinged articulated rigid booms, truss structures, telescopic booms, inflatable structures, CFRP (Carbon Fibre Reinforced Plastic) / SMC (Shape Memory Composite) booms, STEM & Bi-STEM (Storage Tubular Extension Member), CTM (Collapsible Tube Masts), Coilable Booms and Tape Springs [20].

Table 1: Various boom and mast types with examples (table source [20])

Articulated Boom	 <p>ESA – European Concept</p>
Truss Structures	 <p>Tensegrity Mast (Royal Institute of Technology, Stockholm)</p>  <p>ADAM's Mast (ATK)</p>

<p>Telescopic Boom</p>	 <p>SULA Boom (SSTL)</p>
<p>Coilable Boom</p>	 <p>(ATK)</p>
<p>Tape Spring</p>	 <p>Left: Antenna (ESA/DLR), Right: Solar Panel (Airbus)</p>
<p>Shape Memory Composites</p>	 <p>Left Solar Sail (ATK), Right: Solar Sail (DLR)</p>

STEM / CTM	 <p data-bbox="580 389 1406 427">Left: STEM & bi-STEM (NASA) and Right: CTM Boom (DLR)</p>
Deployable Tape Truss	 <p data-bbox="580 745 1366 842">Deployable Carbon Tape Truss for Gossamer Space Structures (DLR). Five bay truss prototype in deployed state.</p>

Foldable Shells

Foldable shells can be divided into two parts, the solid surface and the largely deformable shells [6]. Foldable solid surface shells are split into multiple pieces joined by hinges in order to be foldable. These solid surface reflectors are very modular and have a high surface accuracy. Largely deformable shells on the other hand are very flexible and can be folded directly. During folding the structure needs to be constrained because it will spring back in its original shape. Typically these largely deformable shells are made of a CFRP membrane. Sometimes these flexible shell membranes require additional back support structures.

Spinning Assemblies and Tethers

Spinning and Tether deployment are used for structures without any bending stiffness like cable or thin membrane structures. Spinning assemblies make use of the centrifugal forces acting on corner masses of a net or a membrane to deploy and stabilise the structure. Example for this methods are the Japanese solar sail IKAROS deploying a

solar sail via spinning introduced by thrusters on the central section and Strathclyde's experiment SUAINEADH, deploying a 2m x 2m web with spinning introduced by a reaction wheel [21][22][23] [24][25]. A detailed description including experiment design, launch campaign summary and result evaluation of the Suaineadh experiment can be found [26].

Tethers on the other hand are kilometre long cables with masses on each end. Tethers can be used for orbit alteration and power generation [27]. The deployment method of Tethers includes spinning deployment via centrifugal forces, propelled separation or via initial acceleration and dissipation.

Electrostatic Deployment

The means of electrostatic deployment is a more exotic method with currently the lowest TRL. Electrostatic deployment makes use of opposing forces acting on thin walled metallic structures which are electrostatically charged. The thin flexible structure is electrically charged developing a repelling force on opposing surfaces also known as the Coulomb force.

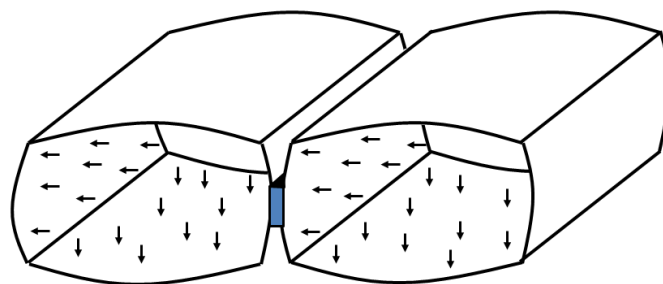


Figure 2-9: Drawing of two cells inflated by electrostatic forces

Individual charged cells made out of thin aluminium foil could be used to deploy such a structure. Two of such cells can be seen in Figure 2-9; each cell initially has a rectangular outline but becomes curved when the field is applied. Each of the cells has only four sidewalls that are all charged with the same field resulting in a force from the inside towards the outside. If no field is applied the cells collapse, this is caused either by their own weight if gravity is present.

Extensive research of this technology has been carried out by the University of Colorado (Boulder, CO, USA) [28]. The technology has potential but high electric fields of the order of a few thousand volts are required, and the EMC (Electromagnetic Compatibility) problems that these high fields might cause on the satellite subsystems needs further consideration.

Inflatable Structures

One of the most promising fields in deployable structures is the field of inflatable structures. Reasons for the use of inflatable structures range from their low cost over exceptional packaging efficiency, deployment reliability and low stowage volume to low weight. Over the last few decades, inflatable structures became an emerging field to overcome launch vehicle payload size restrictions [29]. Research in inflatable structures can be dated back to the 1950s. The first major developments during this time showing the potential of these novel structural concepts were the Goodyear antennas in the early 1960s and the Echo Balloon series from the late 1950s to the early 1960s. The Contraves antennas/sunshades and the L'Garde, Inc., inflatable decoys followed in the 1970s and mid-1980s [30]. The biggest achievement up to date is the Inflatable Antenna Experiment (IAE) of L'Garde which was launched from a Space Shuttle in May 1996 [31].

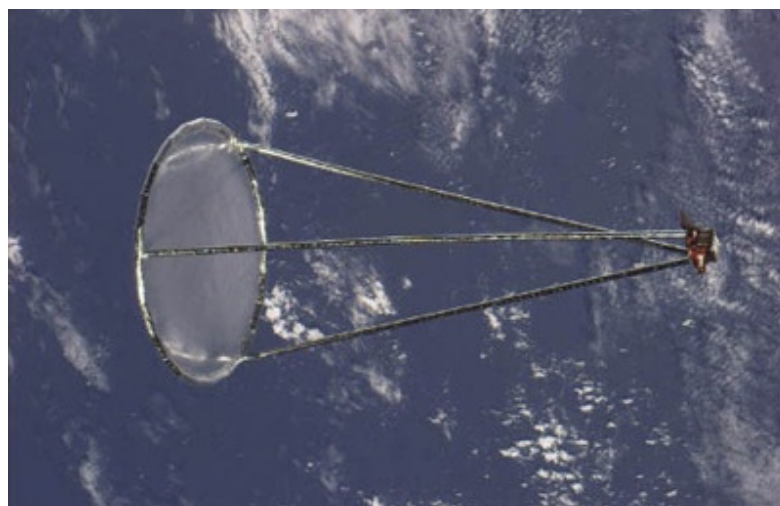


Figure 2-10: Inflatable Antenna Experiment (IAE) deployed in 1996 (source NASA)

Research has been undertaken in various institutions all over the world in the field of inflatable structures [32],[33][34]; new membrane materials have been discovered that can withstand the space environment, advanced simulation tools were developed that capture the highly non-linear behaviour of the inflation process and rigidization techniques have been investigated making the structure non-reliant on the inflation gas after deployment [35],[36],[37].The industry is focusing on a variety of applications of inflatable structures to enable future space flight at present. After 1996, inflatables were mainly used as protection devices for planetary rovers. The inflatable balloons were used to soften the landings of the Mars rovers Pathfinder in 1996 and Spirit and Opportunity in 2003.



Figure 2-11: Deployment test of inflatable airbags of Mars Pathfinder mission in 1996 (source NASA)

Various companies are working on the use of inflatable antennas, reflectors, booms and solar arrays as satellite components. Other research is carried out in inflatable boom experiments like the CFRP Booms from the German Aerospace Center (DLR) [38]. Also NASA is working on a couple of inflation based structures which led to a successful test of the Inflatable Re-entry Vehicle Experiment (IRVE-3) in July 2012 and the above mentioned Low-Density Supersonic Decelerator (LDSD) project with its inflatable prototype test of speeds up to Mach 4 in July 2014. The most ambitious plan comes from Bigelow Aerospace which has the target of building a Commercial Space Station

consisting of inflatable modules. In January 2013, Bigelow Aerospace was contracted by NASA to build an inflatable module called BEAM (Figure 2-12) to be tested on the International Space Station. The BEAM module was launched with the SpaceX Dragon capsule in March 2016 and was successfully inflated during the second try on the 28th of May 2016 [39].

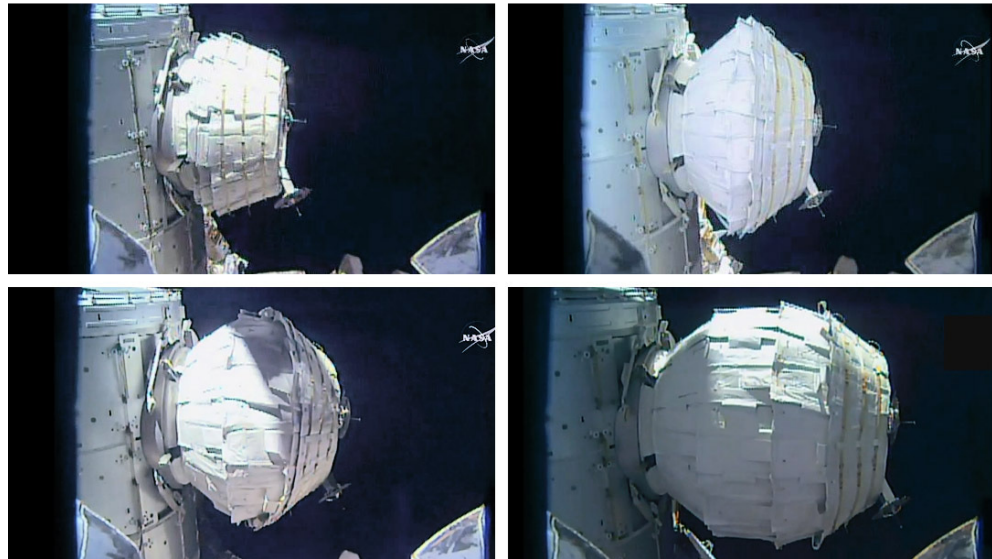


Figure 2-12: Inflation of Bigelow BEAM module attached to ISS (source NASA)

Other applications include the use of inflatables as capture and docking mechanism like the Inflatable Capture Mechanism (ICM) developed by TAS-I (Italy), Aerosekur (Italy) and SMA Research (Italy) for the Mars Sample Return reference mission in 2009 [10]. The use of inflatable tubes as part to deploy tensegrity reflectors has been also considered at the beginning of this research work on smart deployable structures [40].

An important aspect in the development of inflatable structures is the method of inflation, the three technologies that are most promising and considered further in this work are pressure vessel inflation, cold gas generator (CGG) inflation and residual air inflation.

The first option of triggering the inflation could be the use of a central pressure source. This could be either a pressurised vessel or a cold gas generator that creates a volume of gas once triggered. Nitrogen is the most commonly used gas in CGGs. The pressure source can be built as a rigid element with the capability to take very high

internal pressures. The other inflatable cells can be wrapped around the rigid part to keep the storage volume small. The big advantage of this system is the reliable control and the high TRL (Test Readiness Level) of the available systems, the disadvantage would be its size and possible restrictions due to its added risk of explosion of pressurized compartments for secondary payload launches.

Trapped or residual air is the air that is left inside the structure at manufacturing on ground at sea level conditions. As soon as the structure is subjected to vacuum space conditions the structure will inflate itself creating a very low internal pressure. This pressure can be on the order of 10-200Pa, depending of the enclosed air mass [41]. Strathclyde's experiment StrathSat-R [42], which is presented in Chapter 4.2.3, had the purpose to validate the possibility of deploying structures in space using residual air inflation [43]. Figure 2-13 shows the residual air inflation of a cell made out of two thin sheets of Mylar welded together on their circumference. It can be clearly seen that the trapped air inside the cell is enough to inflate the cell at vacuum conditions (Figure 2-13 right).

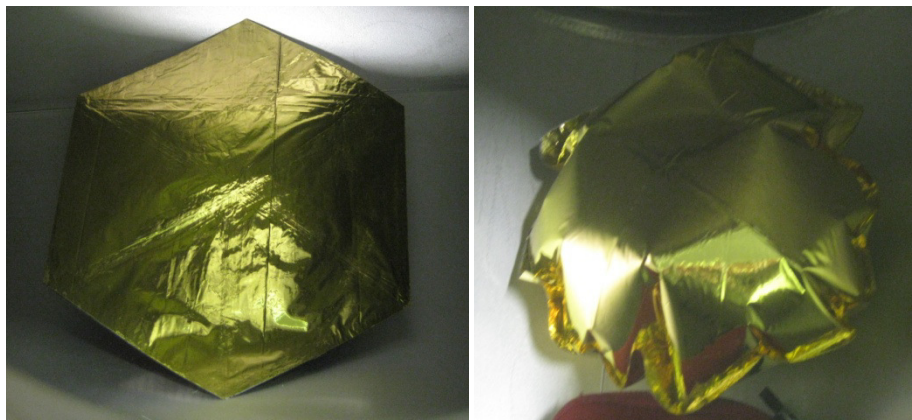


**Figure 2-13: Cell Residual Air Inflation in Vacuum Chamber
left: at ambient pressure, right: vacuum pressure**

There is also the option to seal the inflatable structure at a higher environmental pressure which would result in a higher pressure in a vacuum environment. One of the difficulties in this system lies within the manufacturing of the structure as well as air containment of trapped air mass inside the structure.

In order to make an inflatable structure rigid and resistant to micrometeoroid and space-debris impacts [44]; the structure needs to be rigidized from the flexible inflated state to a stiff rigid state. The rigidization also serves the purpose of obtaining a structure that is independent on the inflation gas after inflation. The rigidization technologies range from thermally cured thermosets to expandable aluminium film composites. The following overview should give a short summary on available rigidization techniques today, it is not meant to be a detailed scientific explanation of each of the available technologies. For more detailed explanation on the technologies please refer to the references.

One option is the use of thermally cured thermoset composites that consist of a fibrous substructure impregnated with a thermoset polymer resin. By introducing heat by for example solar illumination or resistive heating, the resin will cure and rigidize the structure [45].

The glass transition temperature rigidization is working in the way that the stored structure will be heated by the surrounding electronics and therefore stays flexible. As soon as the structure gets subjected to the cold space environment the structure becomes rigid [46]. The composites are also known as second order transition change or SMP composites [45].

Another option is the use of composites that cure in ultra violet (UV) light. The inflated structure is impregnated with a resin that will cure at certain wavelengths. The two ways of rigidizing the structure are either through the UV energy of the sun or the energy transmitted by UV lights embedded in the structure [38], [47][47].

The use of plasticizer or solvent boil-off is another possibility to rigidize inflatable structures. The principle behind this technique is that a softening component in the resin evaporates once subjected to the space environment and thereby rigidizes the composite [45].

Foam rigidization fills the cavities of the inflating structure with structural foam that reinforces the structure once deployed.

The oldest technology is the aluminium and film laminate rigidization technology which was used in NASA's ECHO II program in the 1950s. The laminates used for this approach consist of thin laminates made from ductile aluminium and polymeric film. The principle behind this technique is to stretch the aluminium beyond the aluminium's hardening stress. After stretching, the pressure is released and the aluminium is in a compressive stage while the polymer is still in its elastic range, the result is a rigid structure.

Despite all the advances in the field of rigidization technologies, no in space rigidization on any inflatable structure has been performed up to this date. One of the biggest problems with the rigidization is that in a real life application the rigidization will most likely be uneven which creates distortions in the shape of the reflector that are almost impossible to predict or simulate.

2.2 Shape Changing Structures

Various space structures are serving just one specific purpose in space systems nowadays. By developing a structure that can adapt itself to various mission stages, the flexibility of the entire mission can be enhanced. With applying shape changing structures, the spacecraft can easily adjust itself to the space environment and expensive on-ground simulation to verify the accuracy of the structure when subjected to the harsh space environment will become no longer necessary. Such a smart structural system is commonly a sum of various different systems including sensors, controllers and actuators. In the following, the most common adaptive materials are outlined which can be used in conjunction with a controller to form a morphing structure.

2.2.1 Adaptive Materials

Adaptive materials are a specific field of materials that are capable of changing their properties as a responds to an external stimuli. These external stimuli can be an applied temperature change, an electric field alteration or by change of light. The number of adaptive materials is as vast as their application areas; the list in Table 2 gives an overview over the most common adaptive materials.

Table 2: List of Adaptive Materials

Material Name	Stimuli	Change
Chromogenic Systems	Electric Field/ Thermal	Optical Properties
Dielectric Elastomers	Electric Field	Volume
Ferrofluid	Magnetic Field	Appearance
Halochromatic Materials	Acidity	Colour
Magnetic Shape Memory Alloys	Magnetic Field	Displacement
Magnetocaloric Materials	Magnetic Field	Temperature
Magnetostrictive Materials	Magnetic Field	Displacement
Photomechanical Materials	Light	Deformation
PH-sensitive Polymers	PH-change	Volume
Piezoelectric Materials	Electric Field / Stress	Length / Electric Field
Shape Memory Alloys (SMA)	Temperature / Stress	Deformation
Shape Memory Polymers (SMP)	Temperature / Stress	Deformation

Thermoelectric Materials	Temperature	Voltage
Temperature Responsive Polymers	Temperature	Deformation

The most interesting adaptive materials for the application in a shape changing smart structure are the materials which are capable of alternating their shape by a given external stimuli. These materials are temperature responsive polymers, dielectric elastomers, shape memory alloys and polymers, as well as magnetostrictive, photomechanical and piezoelectric materials which are described more in detail below.

Other adaptive materials include chromogenic systems that change their colour or cloudiness as a result of applied voltage, temperature or light. Examples for this material include liquid crystal displays or darkening sunglasses. Ferrofluids are a mixture of nanoscale ferromagnetic particles and a carrier fluid. The mixture can obtain different shapes depending on the applied magnetic field.

The adaptive materials of interest for this application are dielectric elastomers, shape memory alloys and polymers, as well as magnetostrictive, photomechanical and piezoelectric materials which will be outlined more in detail in the following.

Dielectric elastomers are actually a composite of multiple materials where a thin passive elastomer film is placed in between two compliant electrodes forming a capacitor [48]. When an electric field is applied on the electrodes, the Coulomb forces cause an electrostatic pressure and thereby compressing the elastomer film. This thinning of the elastomer makes it more compliant to tension letting the material respond with a change of length depending on the applied electric field. Dielectric Actuators have a high elastic energy density and are very lightweight. The field of dielectric elastomers promises a paradigm shift in smart material application due to its very large shape changing capabilities of up to 300% but their durability needs to be improved further [49].

Photomechanical materials alternate their shape when exposed to light; the material can be triggered, depending on the wavelength of the light [50]. These materials are

polymers with an azo compound that can physically and mechanically respond to light. Application of continuous wave light or irradiation with an interference pattern result in an expansion of the soft film [51].

Shape memory alloys are metallic alloys that can undergo martensitic transformations when subjected to applied thermo-mechanical loads [52]. The alloys are capable of recovering plastic strains when heated up above a certain temperature. SMAs can also be heated using resistive heating through an applied electric field increasing the application areas of the material. In a similar fashion, shape memory polymers undergo a phase transformation depending on the applied temperature. Shape memory alloys and polymers are inherently capable of being trained to almost any shape with one way and two way memory effects [53]. The advantage of shape memory material is their wide countless possibilities of obtainable shape but their disadvantage is their hysteresis behavior as well as the required high temperatures for shape change which could cause problems in the very low temperature space environment.

Electrostrictors are ceramics that expand in the presence of an electric field by a coupling effect between the applied electric field and the electric dipole of the material. Magnetostrictors work in a similar manner as electrostrictors but they are actuated by a magnetic field instead. These materials and actuators require high electric and magnetic fields and are usually rather heavy.

The piezoelectric effect describes the displacement of monopoles in the piezoelectric material when applying an electric field [54]. This forced displacement of the monopoles causes an elongation of the material. Composites made out of piezoelectric material and varying applied fields enables the structure to deform also out of plane. Also the material can serve as a sensor or energy harvesting device due to its reversibility of the piezoelectric effect transforming displacement to electrical energy. Piezoelectric actuators are very precise and display as inherently low hysteresis but the applied fields are high in the order of a few kilovolts and corresponding strains of only fractions of percent.

2.2.2 Smart Structural Concepts

A common misconception is the existence of smart materials, there are only smart structures. A smart structure is a system that responds to a given stimulus with a desired response. To make the most use out of an adaptive material, it needs to be integrated in an optimized system which is capable of obtaining the desired property change. A smart system usually consists of an actuator, a sensor and a controller. The adaptive material can act as an actuator and as a sensor; an example of this would be piezoelectricity which can act both ways, as a displacement actuator with an applied electric field or as a position or acceleration sensor which gives a specific electric field back depending on the deformation. Unfortunately, most of the adaptive materials available today require a constantly applied actuation force to obtain the desired shape which results in high power consumption. Other devices are bi-stable, using a short actuation impulse to switch between two different stable states. It is especially important that a space structure can stay in the deformed shape without the necessity of constantly driven actuation due to on board power constraints. The following subchapter outlines some selected smart structures focusing on shape changing performance or technologies that could enable programmable matter.

Over the last half century, continuous research and development work has been undertaken in the field of pneumatic devices that mimic biological muscles for actuating mechanical systems, for example in high lift surfaces on planes [55]. Pneumatic muscles were created that shorten when inflated and thereby become capable of lifting substantial loads [56]. Especially interesting for the proposed application are the methods employed by R. Vos [57],[58] and his work on a morphing air foil that utilizes gas filled elastic pouches that vary their diameter depending on the pressure of the environment. Such an air foil is able to independently adapt its shape depending on the altitude without the need for further control.

The researchers of the Whiteside Research Group at Harvard University took the development of air actuated devices a step further by creating soft robotic actuators that enables structures to move in a coordinated fashion [59]. These soft robots are

manufactured from hyperelastic material that was cast in 3D printed molds inspired by star and jellyfish.



Figure 2-14: Four legged soft robot (source [60])

Figure 2-14 shows a four-legged platform that is able to move by in sequence inflating and deflating multiple cavities in its body. Thereby the robot becomes able to crawl and squeeze through spaces.

In active fibre composites some of the carbon or glass fibres in a normal composite are being replaced by adaptive material like for example shape memory polymers or similar. With controlled fibre and layer placement the composite can be deformed in a desired fashion through actuation. Another interesting approach is embedding these active fibres in an asymmetric composite, e.g. a $[0,90]$ layup forming a bi-stable structure where the adaptive fibres can be used to switch between the two stable states.

EMPA is the Swiss interdisciplinary research and services institution for material sciences and technology development. The Materials and Engineering laboratory, created in 2005, developed electrically activated elastic polymer films that expanding their surface when an electric field is applied. These electroactive polymers are also part of dielectric elastomers which are described in Chapter 2.2.1. Figure 2-15 shows these

very thin and light actuators attached on the skin of a light airship. Alternating actuation of the actuators mimics the locomotion of a fish and thereby propels the airship.

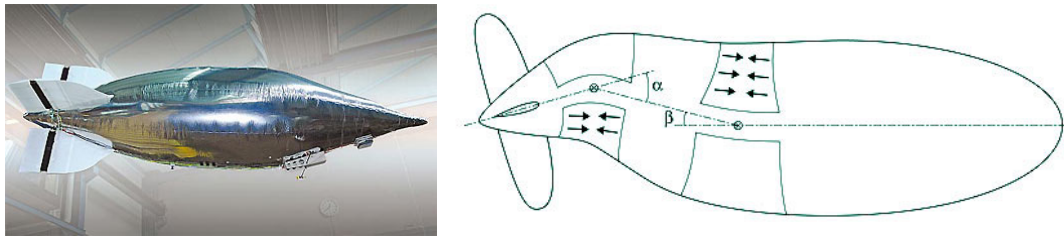


Figure 2-15: RC controlled smart airship with electrically activated polymer film actuators left and schematic of locomotion principle right (source EMPA)

The idea behind the self folding structure is the combination of rigid triangular fibre glass panels which are connected to each other with shape memory alloy hinges. By running electricity through the connecting hinges and thereby actuating one continuous line of these hinges, the structure gets folded along this line. Researchers at MIT and Harvard invented the self-folding sheet that can be seen in Figure 2-16 [61].

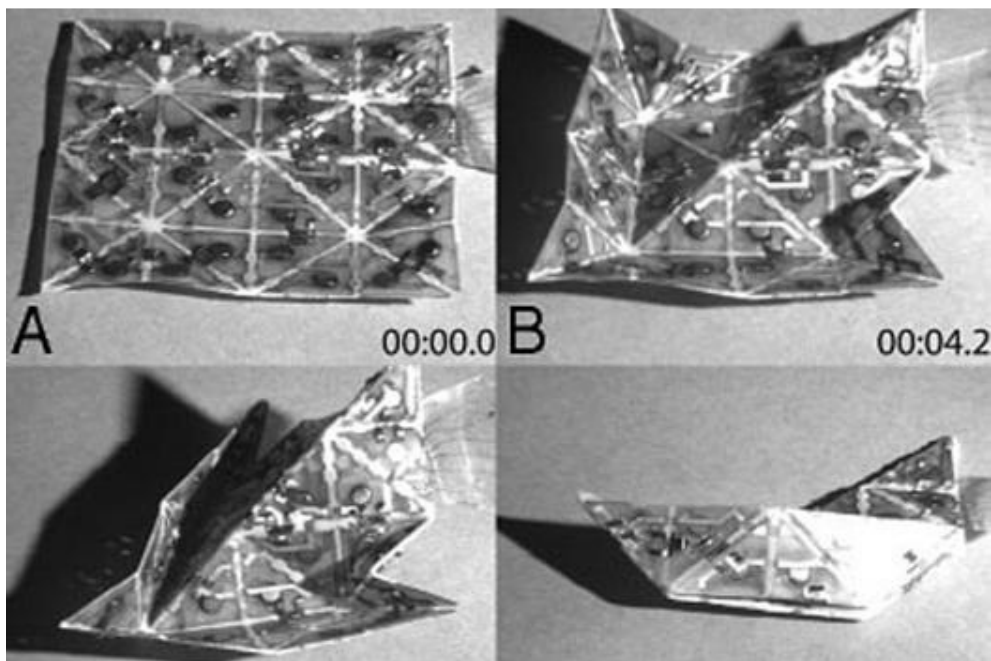


Figure 2-16: Harvard and MIT's self-folding sheet (source [61])

These self-assembling structure consist of many identical smart own standing systems that have interfaces on each side. These systems can assemble each other to a bigger shape by controlling the interfaces with for example magnetism. The big

disadvantage is the current size and weight of the systems and their rigid nature meaning that they cannot deploy to a bigger volume in space. In 2010 work undertaken at MIT was able to create cubes that that were able to disassemble themselves in a kind of smart matter using custom-designed electro permanent magnets to attach the cubes to each other, communicate with each other and exchange power [62].

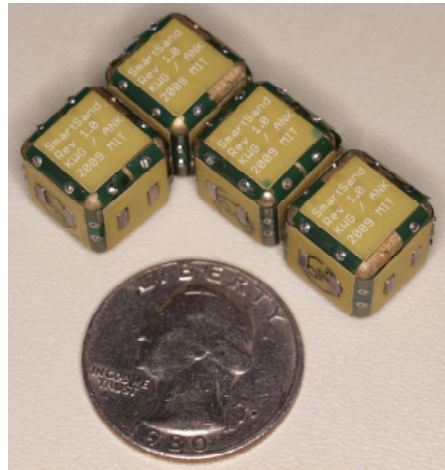


Figure 2-17: MIT's Robot pebbles creating programmable matter [62].

In 2014, researchers at the University of Harvard developed a new system that involved a swarm of thousands of simple robots that were able to assemble themselves in various different shapes [63].

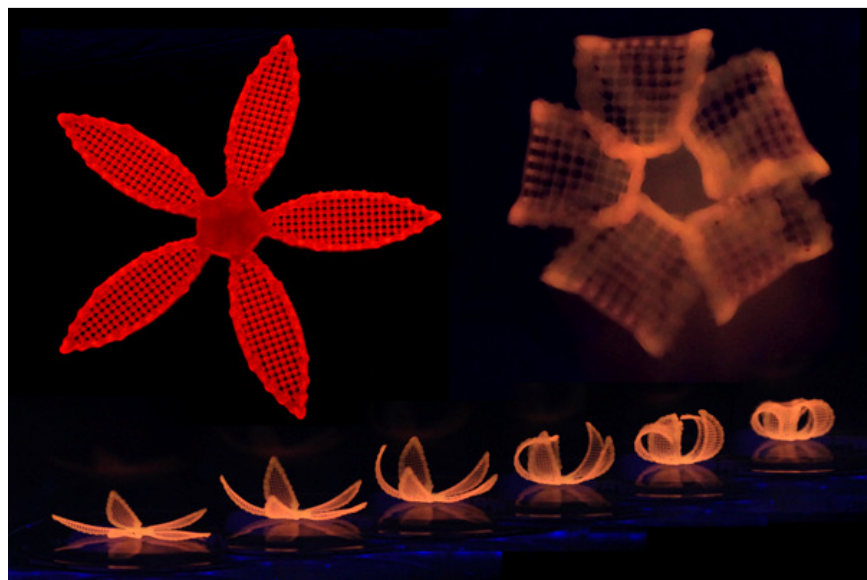


Figure 2-18: Harvard's 4D printed orchid actuated in water (source Wyss Institute at Harvard University).

Also at the University of Harvard, in 2016 researchers were able to create a 4D printed structure which are designed to change their shape after they have been 3D printed [64]. The structure is printed using two different materials, one which is stiff and the other one that is water absorbent. Once the structure is immersed in water, the shape of the structure can be changed as the water absorbing material is doubling its size. By properly designing the structure and with the use of 3D printing enabling the fabrication of complex structures, shape shifting structures can be created. Figure 2-18 shows such a 4D printed structure actuated in water.

2.3 Synopsis

In order to create the smart deployable structure and to fulfil the requirements of low storage volume, deployment reliability, shape changing capability and shape holding without power consumption, the best combination of deployable technology and adaptive material needs to be chosen. For the deployment method, inflation is the most promising due to its simplicity, reliability and very low storage volume. Regarding the adaptive material and the smart structure, none of the existing concepts poses a viable solution for very large smart structures either due to their small actuation length (piezoelectric), high mass (magnetostrictors) or their temperature dependency (SMAs). A new concept needed to be developed combining the smart and the deployable structure to a harmonised system.

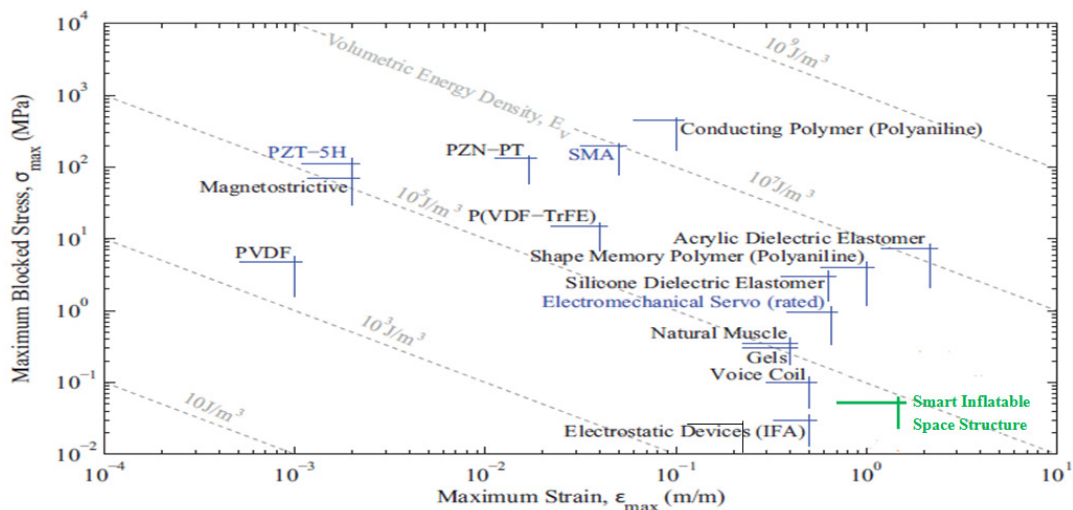


Figure 2-19: SRI International/DARPA specific energy chart of existing actuators and the developed smart inflatable space structure (original from Ref.[57]).

Figure 2-19 shows the DARPA/SRI International energy chart of exciting actuators with their maximum strain and blocked stress. The developed smart inflatable space structures design space is within the lower right part of the chart. Since these structures are designed to be used in space under the influence of only small gravitational forces, it is possible to design an extremely light, flexible structure with the capability of changing its shape and overcoming very low blocked forces. The displacement and the deformation capability on the other hand is very high reaching to 200% because they are being used in a micro gravity environment with only minor, slow perturbations.

Chapter III

Bio-inspired Smart Structures

In the previous chapter, the need for a completely new technology to enable deployable smart structures was outlined. In this chapter, inspiration is taken from nature with its plants capable of fast movement to create such a deployable smart structure. The original work starts with the development of a scalable mechanical analogue capable of deployment and shape change. The main idea behind the mechanical analogue is that the structure consists of colonies with hundred of hyperelastic inflatable cells which can vary their size by shifting fluid in between them. The main part of this chapter focuses on the description of a developed multibody code capable of simulating the deployment by inflation as well as actuation through fluid shifting cells and the influence of external forces. The multibody code outlined in this chapter is then used for example applications in the next chapter.

3.1 Inspired by Nature

Over millions of years nature has optimised its organisms to survive the harsh conditions on Earth. This evolution did not necessarily mean the survival of the strongest or biggest but more the survival of the best adapted. To take advantage of these million-year developments, more and more systems in our daily life are inspired by nature. A popular example is the lotus effect property in plant leaves which is used in current paints to repel dirt within the surfaces. In the following subchapters inspiration is taken by nature to build a deployable shape changing structure.

3.1.1 Nature's Deployables

Biology might be redefined as the natural history of deploying structures [65]. Interesting examples include deployable membranes link the wings of insects that can be

also folded like origami once expanded and the deployment of tree leaves or flower pedals. These leaves are deployed in a short timeframe and might be folded and stored again in a diurnal rhythm. An example for the leaf deployment can be seen in the figure below for the legume plant.

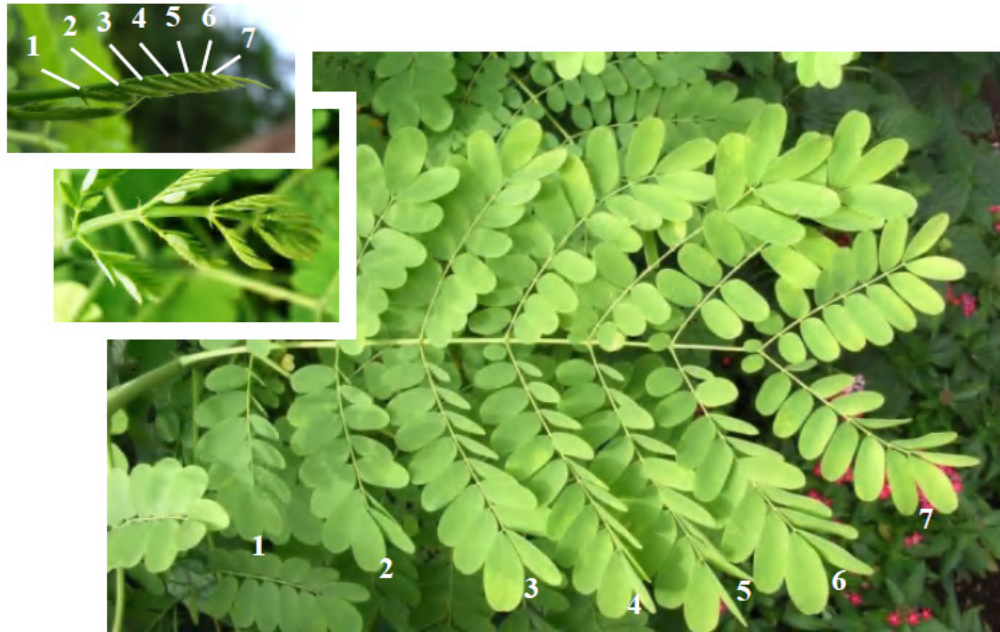


Figure 3-1: Deploying leaves of a legume plant [66]

A most interesting case with respect to high volume increase is deployment via inflation. A good example here is the deployment of dragonfly wings. The dragonfly deploys its wings in a short amount of time, increasing the wing area forty fold. The dragonfly wing consists of thin membranes connected by branching veins. By pumping air in the small channels, the dragonfly can unfold its wings during its metamorphosis from the larva state. After the deployment process, the dragonfly rigidizes its wings with the help of the sun eliminating the need for the cannels to stay inflated; the wings are now a stable and light structure.



Figure 3-2: Eclosion process of a dragonfly [66]

Many plants also have the possibility to alter their appearance to adapt to the ever changing environment. Such a plant-derived development is known as tropism and is explained further in the following chapter on nature's shapeshifters.

3.1.2 Nature's Shapeshifters

Tropism is the Greek word for "turning" and it describes the biological movement of a plant in reaction to an external stimulus e.g. a light in a specific wavelength [67]. According to its stimuli, tropism can be divided in different types. Existing tropism include Chemotropism which is the movement or growth in response to chemicals, Geotropism or Gravitropism as a responds to gravity, Hydrotropism to water, Sonotropism to sound, Thermotropism to temperature, Electropism to electric fields, Thigmotropism to touch or contact, Heliotropism to sunlight and Phototropism to lights or spectral colours of the light.

Certain flowers have the capability to follow the path of the sun over the sky during a day with their flower head or leaves. The phenomena was discovered and named Heliotropium by the Ancient Greeks. However according to Aristotle's logic of plants being passive and immobile organisms, it was assumed to be a passive effect [68]. Following growth experiments in the 19th century, the observation was made that some sort of growth processes in the plants stem were involved. Thus, the phenomena were named Heliotropism in 1832 for the first time just to be renamed to Phototropism in 1892. The reason for the name change from Heliotropism meaning turned by the sun to Phototropism meaning deformation caused by light influences was the result of lab experiments on algae that showed strong dependence on light brightness and direction, not purely on sun light.

The research undertaken here in this thesis was inspired by the movement of sunflower heads from East to West following the path of the sun during a day [69]. In nature Heliotropism and Phototropism can be used interchangeably because the sun is the only source of light. This principle can be also observed by plants growing in arctic

climates where the exploitation of heliotropism enables arctic poppies (Figure 3-3) to retain warmth within the plant [70].



Figure 3-3: Arctic poppies moving their head towards the sun [70]

The cells that give the plant the ability for fast movements are called motor cells and act like hinges or joints. The movements are driven by the shrinking and swelling of opposing cell regions of the pulvinus (motor organ) [71]. The pulvinus is a joint-like thickening at the base of a plant or leaf facilitating growth-independent movement. These motor cells are capable of adjusting their intermembrane potassium ions (K^+) to change their internal turgor pressure and thereby their shape. The accumulation of intermembrane potassium ions via channels in the plasma membrane enable the osmotic uptake of water into the cell, which lead to increasing cell volume and eventually the cell becomes turgid. On the other hand, the potassium channels can also release K^+ away from the cell membrane resulting in a water release and therefore a shrinkage of the cell [72]. The change in turgor pressure happens gradually and takes from a few minutes up to hours. Faster actuation example are carnivorous plants like the Venus' flytrap which can trigger the closing of its leaves to trap an insect in a fraction of a second. Once triggered, the motor cells in the joint line of the leaf halves becomes freely permeable to K^+ forcing the water out of the cells resulting in an immediate collapse of the cells. Therefore the leaves can close and the prey (e.g. insects) can be trapped.

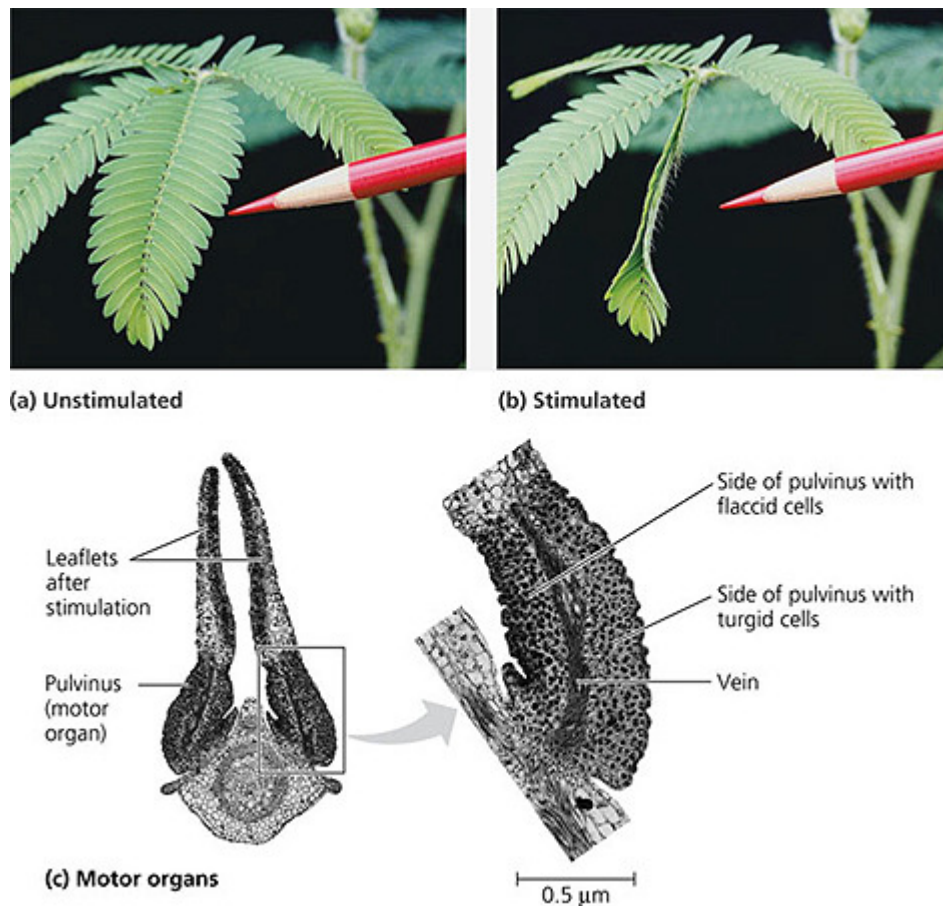


Figure 3-4: Functionality of motor cells (Photo: Copyright Pearson Education, Inc. (Benjamin Cummings), 2005.)

With this mechanism, the flower has the ability for comparably fast movement of its head without the need of growing additional cells. This simple pressure change principle seems perfect for the application on deployable space structures.

3.2 Mechanical Analogue

The original contribution of the thesis starts with the development of the mechanical analogue concept. The following subchapters follow the same outline as the inspiration from nature. First a mechanical analogue of the deploying structure will be presented followed by a description of how to enable shape change within this structure. The mechanical analogue subchapter finishes with an overview on further applications of larger arrays of these shape changing structures.

3.2.1 Deployable Cells

The inflatable wings of the dragonfly are used as an inspiration for developing a deployable structure. The dragonfly wings consist of channels that expand their volume by inflation forming a stable beam element. The mechanism is taken on by using cells which can expand with inflation and it can expand its volume to over 300-900% of its initial stored volume. A material class that offers such a high elastic range are hyperelastic materials like silicon rubbers. The cells can be inflated either by using trapped air which expands once the environmental pressure changes or by releasing stored gas like a cold gas generator. The gas can be then shifted between neighbouring cells until every cell is inflated.

3.2.2 Shape Changing Structure

The motor cells of plants on the other hand can be taken as blueprints to develop a shape changing mechanical structure. For the mechanical analogue, a structure can be created consisting of hundreds to thousands of cells. The smallest reoccurring element in this design is the single mechanical cell which is capable of changing its volume. The shape of the overall structure can be altered by coordinated volume changes of single mechanical cells which are incorporated in a cell array of multiple hundreds or thousands of these cells. This volume change can be seen in Figure 3-5 and it is undertaken by a differential pressure increase due to air molecule increase. Two methods of this pressure increase have been evaluated. One option would be the use of micro pumps in-between two cells that could transfer air molecules between them. This will allow one cell to always be inflated while other deflated. Another option is the use of valves between all the cells with a central pressure source. The system of valves would transfer the air mass to the cell which needed to be actuated. Each method has its pros and cons and the use of one over the other needs to be evaluated for every future proposed application or mission separately.

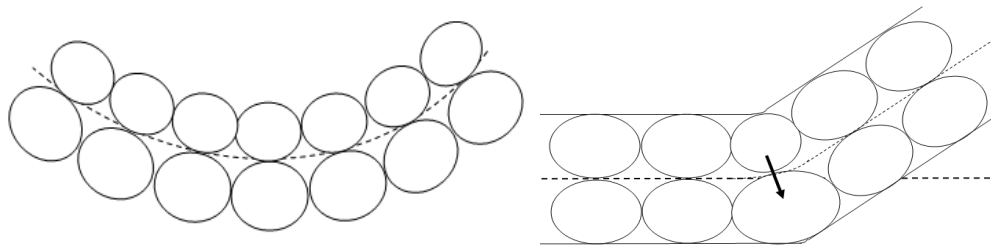


Figure 3-5: a) Pre-deformed membrane b) Shape change of flat membrane introduced by volume change of neighbouring cells

The following subchapters should give a first idea how far this design can be taken using biological inspired structures consisting of unit cells that all act in a specific way to create a global structure with example rigid skeleton cells as well as flexible movable muscle cells. As a follow up, a concept is elaborated using origami math and a flat smart sheet to form any shape imaginable.

3.2.3 Organism architecture inspired structures

The above mentioned design can be even taken a step further into the bio inspired structure by creating a system consisting of cells that have different properties creating as an analogue to a living organism. Each cell can be optimized for one specific application decreasing the overall mass of the system. Also a combination of highly specialized cells and common flexible cells is possible; the best approach depends highly on the actual application of the system.

The possibility of rigid elements in the system gives the structure a predefined shape to overcome gravity or other perturbations. The rigid elements can form a skeleton that can act as a backbone or supporting structure. The options of the deployment of these elements are either to already launch them in their rigid configuration or to inflate the cells in space and then rigidized them once deployed with one of the rigidization techniques described in Chapter 2.1.2. The selection of the appropriate rigidization technique is highly dependent on the chosen application; the first question that needs to be answered is if the rigidization has to be just once or that it should be reversible. For

the irreversible method either the UV curing composite or the strain hardening is suggested. Both systems are light, reliable and can be stored in a much smaller space. For the reversible application the thermally cured resin rigidization is suggested due to its temperature sensitivity. The process of rigidization can be reversed by increasing or decreasing the temperature of the cell material making it softer and therefore deformable or hard and thereby rigid.

The shape changing cells can be treated as an analogue to muscle cells in an organism. By adding arrays of these flexible or active cells in-between the interlinks of the substructure between the skeleton cells the structure becomes more stable and the actuation can be better controlled due to the higher overall stiffness. An example can be seen in Figure 3-6 of an active joint with three types of cells, the rigid skeleton cells in red, the passive flexible cells in white and the shape changing cells in green.

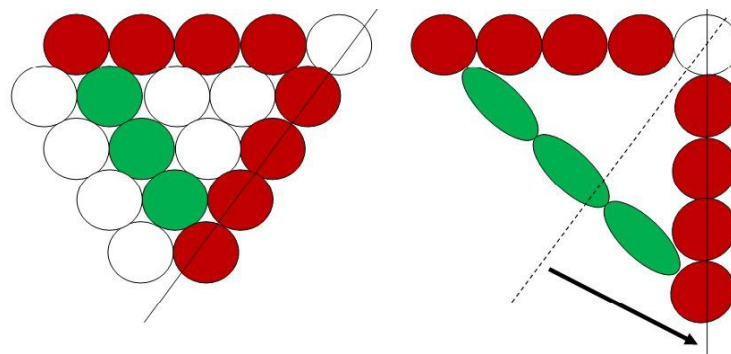


Figure 3-6: Schematic of cellular principle: Red cells are rigid, green are actuator cells and white are flexible cells (cells are hidden in right image for better visualisation)

3.2.4 Self-folding Origami Structure

By adding thousands of these smart deformable cells together to a large array, a smart sheet can be created. This smart sheet can create crease patterns and fold line by itself just by actuating neighbouring cells. By combining the capability of the developed system with the art of origami, almost any shape regardless of its complexity can be created from a simple smart sheet.

Origami is a traditional Japanese art of paper folding originating in the 17th century AD. Origami is the art to create more or less complex sculptures or shapes via folding from one single sheet of paper without the use of adhesive or irreversible cutting. Especially this aspect makes it very interesting for using within the smart structure approach undertaken here. The free flying smart sheet of paper would have the capability to transform itself into any desired shape.

There are only four main laws behind origami math which were outlined by Robert Lang [73]:

- Areas joined by a fold line can be colour coded in two colours and fields with the same colour will never be adjacent.
- At any interior vertex, the number of mountain to valley folds must always differ by two.
- Alternate angles around a vertex sum up to a straight line.
- However sheets are stacked during folding, a sheet can never penetrate a fold.

With these simple rules, Lang developed a mathematical code which is capable of creating folding pattern for any complex shape. The left side of Figure 3-7 shows the crease lines created to fold the beetle sculpture in Figure 3-7 right side.

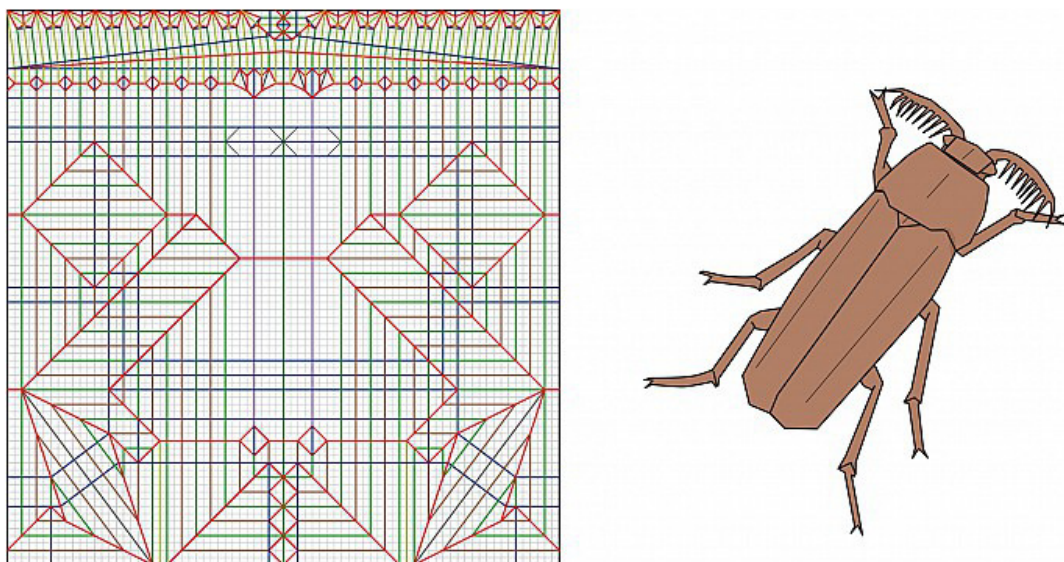


Figure 3-7: Crease pattern and corresponding sculpture (left and right, source: R. Lang [74])

This can be used to create crease patterns which can act as the blueprint to instruct the developed adaptive sheet to deform its flat shape into more complex application dependent shapes.

The shifting of molecules within the structure described in Chapter 3.2 leads to a volume decrease of the bottom cell and a volume increase of the top cell resulting in a buckling of the sheet. Coordinated actuation can be used to control this curvature to form the desired deformation or fold line.

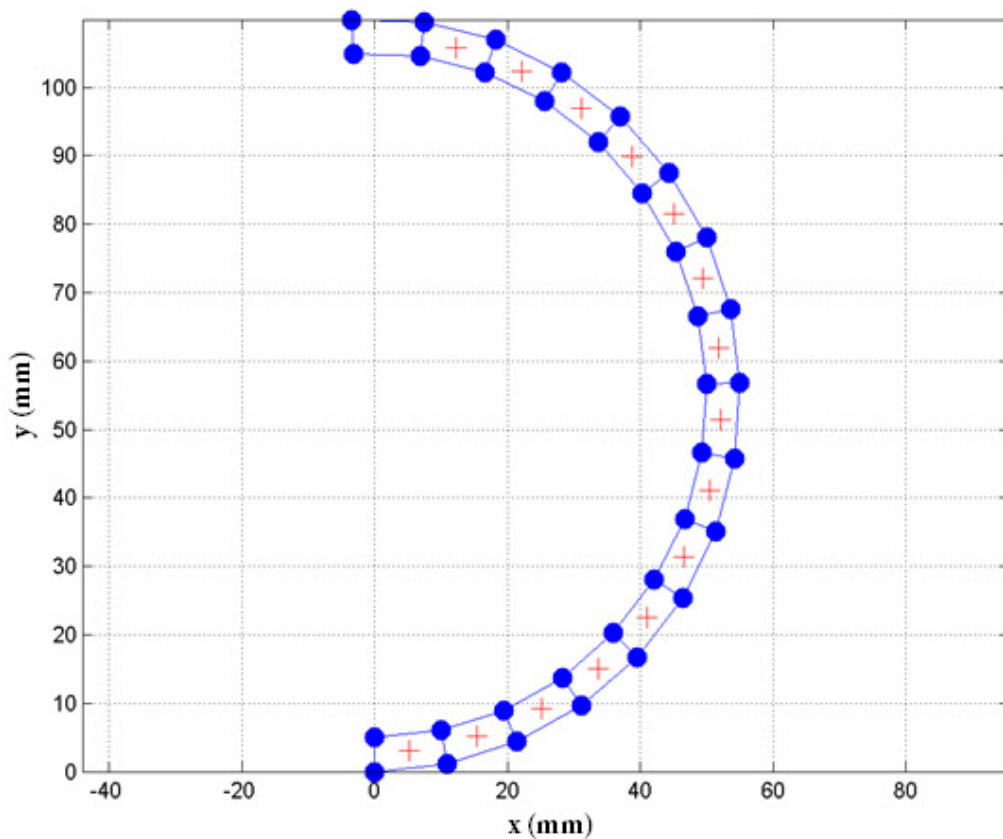


Figure 3-8: Static 2D plot of actuated cell array forming a 180 degree fold

To achieve a simple 180 degrees folding line over the entire sheet, cells in parallel lines need to be actuated. Figure 3-8 shows the 2D static plot of the deformed two cell thick array creating a 180 degree fold. Each cell is represented by a blue dot in Figure 3-8. It can be seen that the actuation occurs from the inside line to the outside line of

cells with increase of volume of the outer cells. With a given actuation capability of 20% of its original length, a full 180 degree fold will require 16 cells.

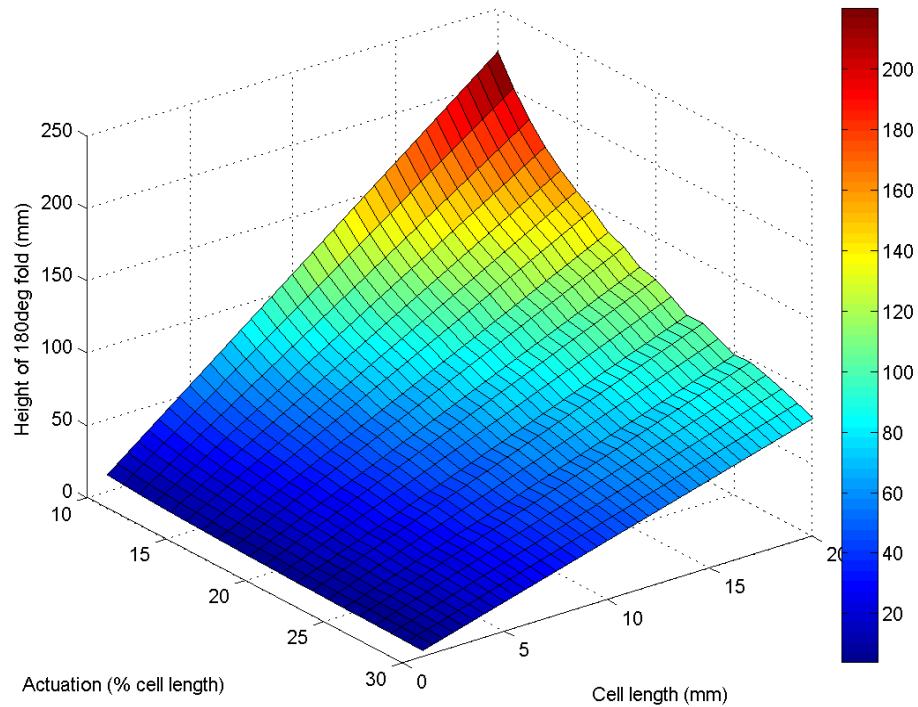


Figure 3-9: Height of 180 degree folds depending on actuation and initial cell length

Figure 3-9 shows the relation of achievable fold thickness of a 180 degree fold in relation to the initial cell diameter and the actuation capability of the used cell. This graph highly depends on the used material and size of the system. The colour code in the figure is the height of the achievable 180 degree fold where black is close to 0 mm and red is 200mm folding height. The scalable nature of the developed structure enables the creation of a system that is applicable from the nano scale up to large space structures. The limiting factor today is only the fabrication technology for miniaturised systems.

The following chapter will present tools to simulate the deployment and shape change of these kinds of structures,

3.3 Discretization and Modelling

Simulations are very important to predict the behaviour of these initial very flexible structures in the appropriate environment. Especially the simulation of a gravity free environment is of great importance for the Gossamer like developed concept with its application in a space environment.

To validate the functionality of the developed concepts with its multiple hundred of inflatable cells forming a rigid or semi-rigid structure in space, commercial FEM programs were consulted first to obtain a better idea on the behaviour of the deploying structure. Simulations of the deployment of the membrane were performed in LS-DYNA™. The initial shape was modelled in the LS-DYNA™ pre-processor LS-PrePost™. LS-DYNA™ is a well-known software used in the industry for nonlinear dynamic simulations. Its development for airbag deployment simulations is especially interesting for this application. The control volume method was used to simulate the inflation of the cells. For the control method approach a mass flow rate into the enclosed structure needs to be defined. By using the control volume method and applying it to the entire structure, a proper inflation characteristic can be achieved due to the fact that the entire volume will expand without starting at one specific initial point. The mass flow required for the control volume method was calculated by employing simple ellipsoid geometrics and thermodynamic equations assuming ideal gas relationships.

For the simulation the use of cells with an initial diameter of 14.5 cm were chosen. 14.5 cm is the diagonal of a 10x10cm² box (cube satellite size). This dimension originates from the sounding rocket experiment StrathSat-R which is described in more detail within Chapter 4.2.3.

Simulations showed that by inflating a single cell from the initial flat shape with 14.5cm diameter, an ellipsoid with a volume of roughly 500cm³ will form after full inflation. Taking $V_{cell} = 500\text{cm}^3$ as the desired fully inflated volume in space and by assuming a pressure difference between the inner structure and vacuum environment of $p_{cell} = 100\text{Pa}$ (0.001bar), the trapped gas mass is in the order of $m_{gas} = 595 \times 10^{-9}\text{kg}$ at

room temperature ($T_{cell} = 293K$) by using the simple thermodynamic equation in Equation 3-1.

$$m_{Gas} = \frac{p_{cell} \cdot V_{cell}}{R \cdot T_{cell}} \quad \text{Eq. 3-1}$$

A triangle shaped mass flow characteristic (as can be seen in Figure 3-10a) was selected over the rectangular progression because of the nature of the residual air inflation method which starts slowly then leading to a maximum at the highest depressurization gradient and slowing down afterwards. By using the equations 3-2 and 3-3 that were derived by Mladenov [75] for the shape change of a Mylar balloon like structure during inflation, the diameter of the inflated cell d_{MB} and its thickness t_{MB} can be derived from the uninflated radius r_{MB} . f_1 and f_2 are factors necessary to develop the equation from reference [75].

$$d_{MB} = \frac{r_{MB}}{2} f_1 = 1.3110 r_{MB} \quad \text{Eq. 3-2}$$

$$t_{MB} = 2\sqrt{2} \left[f_2 \left(\frac{1}{\sqrt{2}} \right) - \frac{1}{2} f_1 \left(\frac{1}{\sqrt{2}} \right) \right] r_{MB} = 1.1981 r_{MB} \quad \text{Eq. 3-3}$$

Using the Mladenov's theorem on a circular specimen with a diameter of $r_{MB} = 7.25\text{cm}$ ($14.5\text{cm}/2$) leads to an inflated diameter of $d_{MB} = 10.78\text{cm}$. With this calculation it can also be said that the thickness of the inflated ellipsoid will be in the order of $t_{MB} = 6.46\text{cm}$.

The triangular mass inflow can be seen in Figure 3-10a. By looking at the inflation time plots in Figure 3-10b. Figure 3-10c and Figure 3-10d, it is obvious that the full inflated volume is achieved after a fraction of the inflation time, while the pressure build up requires the length of the entire inflation process. The pressure increase is due to the defined triangular mass inflow, it needs to be verified if the actual pressure behaves the same way during the bench test.

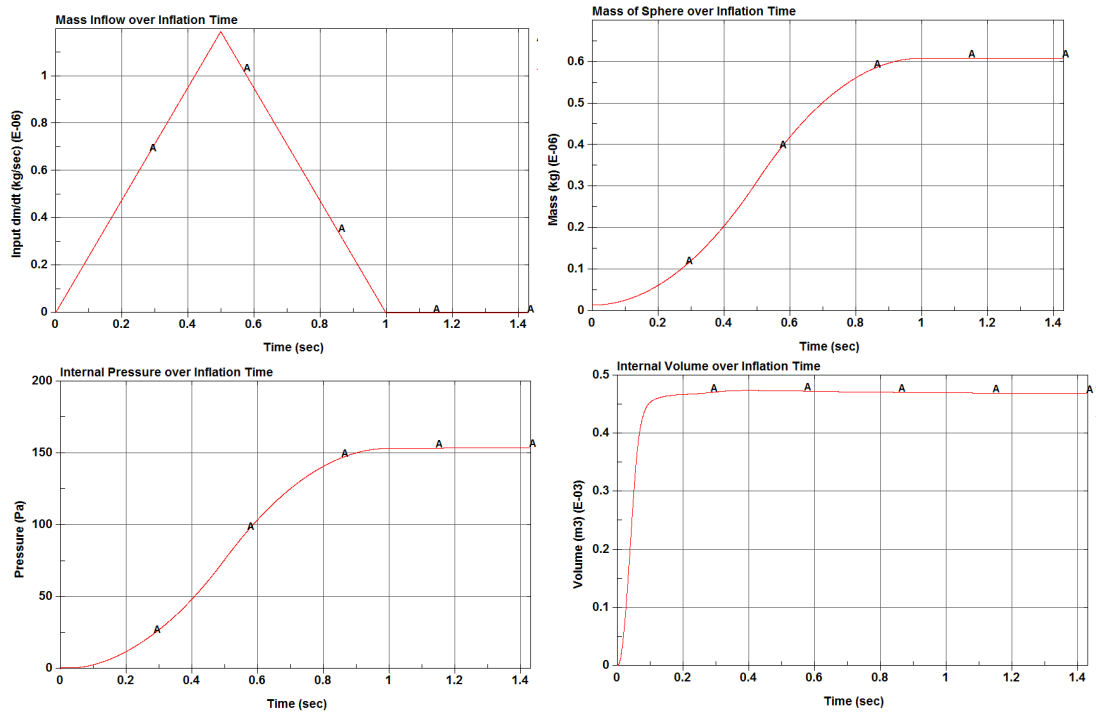


Figure 3-10: LS-DYNA simulation parameters: mass inflow, mass of sphere, internal pressure and internal volume of one single sphere during inflation

Two flat circular sheets with a diameter of 14.5 cm were placed over each other with a 0.1mm gap. The elements on the circumference were then joint to provide the enclosed volume required for the control volume method in LS-DYNA™.

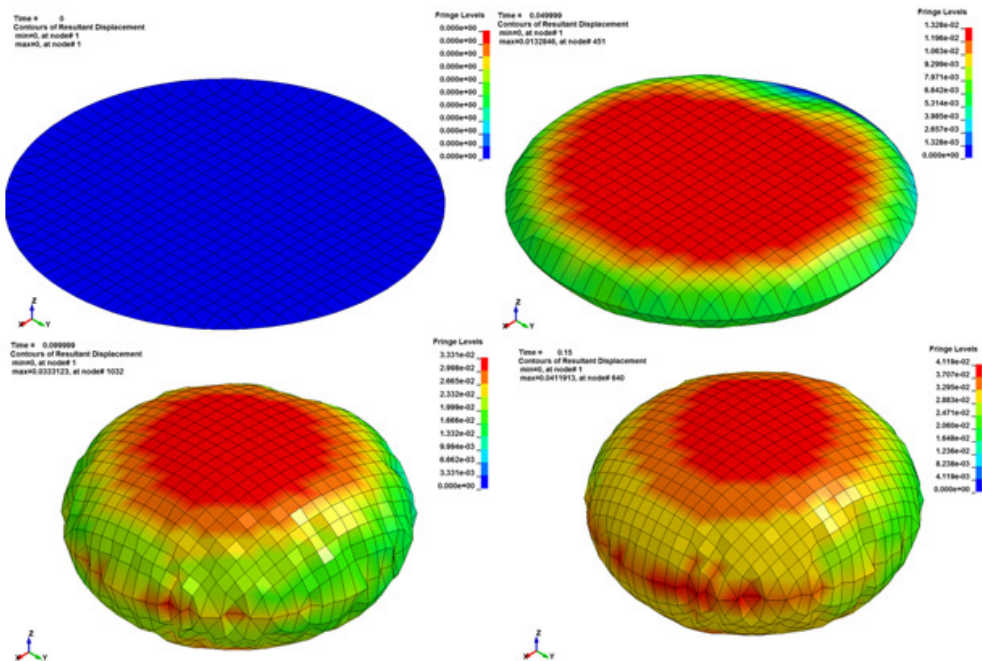


Figure 3-11: Inflation of single cell (LS-DYNA™ simulation)

The single cell inflation was used to verify the design and the concept of inflation in the simulation and vacuum tests carried out at the University of Strathclyde. Due to the fact that the available vacuum chamber would only fit a few cells, simulations had to be run for multiple cells. Another issue for the vacuum chamber experiments or the ground test in general is that the structure is subjected to 1 g gravity. Especially for a low pressure, low stiffness structure, the influence of gravity can be major and can falsify the results of shape adaption experiments. For this reason a sounding rocket experiment outlined in Chapter 4.2.3 was proposed.

The inflation simulation of a 5x5x2 cell array of 50 cells with a simulation time of 10 seconds took at least a full day to run. But to simulate the developed structure in the appropriate environment and in orbital timescales of hours or days, a new much simpler code had to be developed. The developed code had to treat every cell as a simplified cube without the need to know the exact deformation of each and every facet of the cell and therefore reducing the necessary calculations to make it run able on a common desktop computer. Furthermore, the modelling of hyperelastic material in LS-DYNA made it difficult to create a parameterized simulation tool that can easily be adjusted to the dedicated application. Another reason for the development of an own standing code was first the required license and the limitation on how many cores the simulation can be run as well as the modification ability in regards to the applied external disturbances. The previous LS-DYNA simulation can be seen as a verification tool to prove that the structure assembled by multiple flexible inflatable cells form a stable substructure in space. The developed code had the purpose to take the LS-DYNA simulation one step further and also model the actuation and external forces realistically.

Due to the multitude of potential applications and cell geometries, it was necessary to create a parameterized simulation code which can be scaled to the appropriate application dimension. Figure 3-12 shows the basic principle in 2D by using point masses and springs to discretize the complex cells and model the deformation due to

air mass change between the bottom and top cells. This simplified 2D model also shows the expected deformation behaviour of the cells when fluid from the bottom cells is pumped to the top cells resulting in the bottom springs to compress and the top springs to expand.

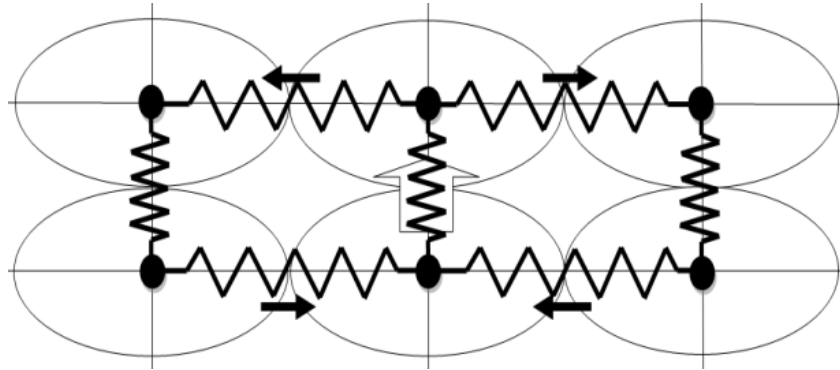


Figure 3-12: Schematic of discretisation of cells

The spring elements in the 2D model need to transmit translational as well as rotational deformations in order to create a structure that is capable of out of plane deformations. For the 3D case, every cell in the simulation is modelled as a cube surrounded by beam elements. These 3D beam elements are basically spring elements similar to the ones that can be seen in Figure 3-12 but with the requirement of having the displacements of the various degrees of freedom coupled. Different modelling approaches for the cells have been undertaken [76]. The use of spherical, elliptical and cube cells were considered. In conclusion, the cube cells were the best analogue for the bio-inspired structure due to the fact that the cells in the discussed plants are cubic. Furthermore, during inflation the hyperelastic spherical cells form cube like structures because the walls of adjacent cells were constrained and were forming cubic enclosures even though the original non inflated cell was spherical. A mass point is located at each corner of the cube. Each beam element is able to transfer tension/compression, bending, and torsional loads between the six degrees of freedom (DOF) nodes. Figure 3-13 shows two inflated spherical elements (red) surrounded by two discretisation cubes. Every cell is modelled with 12 beam elements (blue) and 8 nodes (black) on their corners. By assembling a structure consisting of two cells, the beam elements and node elements in

the centre are joined resulting in a total of 12 nodes and 20 beam elements for the structure as shown in Figure 3-13.

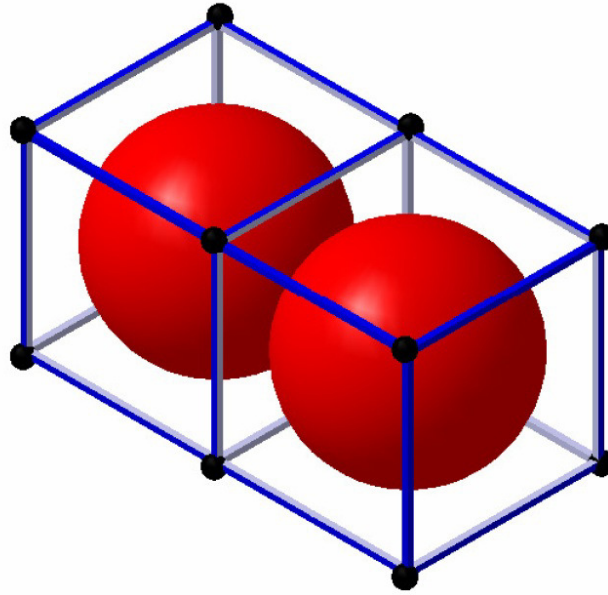


Figure 3-13: Modelling of cells: two inflatable cells (red) inside discretisation cubes made out of beam elements (blue) in-between nodes (black)

Every array has $(n_{cell,x}+1) \cdot (n_{cell,y}+1) \cdot (n_{cell,z}+1)$ nodes (where $n_{cell,i}$ is the number of cells in the i-direction) resulting in a total of 108 nodes for a 5x5x5 cell array for example. The equation of motion is written with mass matrix \mathbf{M} , damping matrix \mathbf{D} and stiffness matrix \mathbf{K} . Entries in all three matrices are dynamically modified based on the inflation and deformation that each cell experiences during the simulation cycle. An example of this change would be the added mass and stiffness while inflating a cell. The coupling terms in the stiffness matrix are especially important for the out of plane deformation of the entire structure.

$$\mathbf{M} \ddot{\mathbf{q}} + \mathbf{D} \dot{\mathbf{q}} + \mathbf{K}\mathbf{q} = \mathbf{F}_{int} + \mathbf{F}_{ext} \quad \text{Eq.3-4}$$

The equation of motion in Equation 3-4 is continuously solved in the time domain to obtain the displacement \mathbf{q} and the velocity $\dot{\mathbf{q}}$. The input variable is the changing force within the cells and the external forces perturbing the structure. The internal force \mathbf{F}_{int} includes the inflation force, the actuation force as well as all the internal contributors.

The external force like the gravity or solar radiation pressure for example is summarized in the external force term \mathbf{F}_{ext} . In the developed model, all the forces are applied to the nodes of the cubes and algorithms have been created to distribute the forces according to their application. A more detailed description on the internal and external forces can be found in Chapter 3.3.3.

First, the assembly of the property matrices \mathbf{K} , \mathbf{D} and \mathbf{M} are described including their change during the inflation of the cells. Secondly, the forces are described in more detail.

3.3.1 Property Matrices

The property matrices in the equation of motion provide the simulation code with the properties of the smart structure. Furthermore, the initial shape and linkage between the cells is defined in these matrices consisting of stiffness matrix \mathbf{K} , damping matrix \mathbf{D} and mass matrix \mathbf{M} . Each of the matrices has six DOFs per node which for example results in 48×48 matrix for a cell with eight nodes. The assembly of each one of the three matrices will be outlined in the following subsections. The effect of the inflation on the beam properties and the effect on whole cells is detailed in Chapter 3.3.2.

Stiffness Matrix

The developed structure takes most of its shape changing potential from the coupling between in plane actuation and resulting out of plane deformation. The use of simple tension/compression springs in the stiffness matrix does not lead to the desired result necessary for the full three dimensional deformation of the structure. For this reason, discretisation methods commonly used for finite element modelling were used to construct a suitable stiffness matrix. The use of torsion-bending beams with their coupling terms gives the stiffness matrix and therefore the developed model the capability for out of plane deformations.

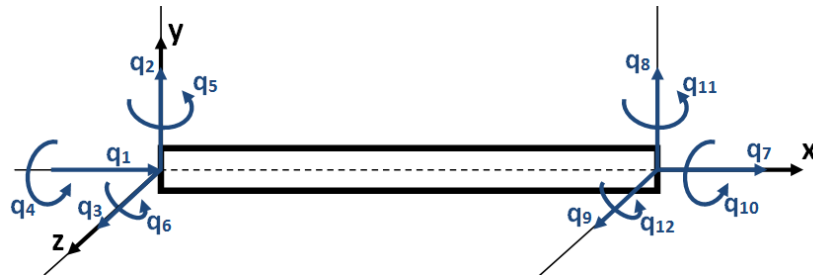


Figure 3-14: Degrees of Freedom of a beam in local coordinates

Figure 3-14 shows the displacement and degrees of freedom in local coordinates. The displacements q_1, q_2, q_3, q_7, q_8 and q_9 are the translations while $q_4, q_5, q_6, q_{10}, q_{11}$ and q_{12} are the rotational DOF. The assembly of the element stiffness matrix of a single beam element rotated into the x-axis, the y-axis and the z-axis can be seen in the Equation 3-5 and onward.

$$\mathbf{K}_x = \begin{bmatrix} \mathbf{K}_{x11} & \mathbf{K}_{x12} \\ \mathbf{K}_{x21} & \mathbf{K}_{x22} \end{bmatrix}, \mathbf{K}_y = \begin{bmatrix} \mathbf{K}_{y11} & \mathbf{K}_{y12} \\ \mathbf{K}_{y21} & \mathbf{K}_{y22} \end{bmatrix}, \mathbf{K}_z = \begin{bmatrix} \mathbf{K}_{z11} & \mathbf{K}_{z12} \\ \mathbf{K}_{z21} & \mathbf{K}_{z22} \end{bmatrix} \quad \text{Eq. 3-5}$$

The unrotated three dimensional beam stiffness equation [77] is split into the following three sub matrices. The unrotated beam stiffness matrix is oriented in the x-axis. The matrices below are rotated with the Equation 3-22 in the y and z direction. The entities of the matrices are described in detail in Chapter 3.3.2.

$$\mathbf{K}_{x11} = \begin{bmatrix} \frac{EA}{L} & 0 & 0 & 0 & 0 & 0 \\ 0 & \frac{12EI_z}{L^3} & 0 & 0 & 0 & \frac{6EI_z}{L^2} \\ 0 & 0 & \frac{12EI_y}{L^3} & 0 & -\frac{6EI_y}{L^2} & 0 \\ 0 & 0 & 0 & \frac{GJ}{L} & 0 & 0 \\ 0 & 0 & -\frac{6EI_y}{L^2} & 0 & \frac{4EI_y}{L} & 0 \\ 0 & \frac{6EI_z}{L^2} & 0 & 0 & 0 & \frac{4EI_z}{L} \end{bmatrix} \quad \text{Eq. 3-6}$$

$$\mathbf{K}_{x12} = \begin{bmatrix} -\frac{EA}{L} & 0 & 0 & 0 & 0 & 0 \\ 0 & -\frac{12EI_z}{L^3} & 0 & 0 & 0 & \frac{6EI_z}{L^2} \\ 0 & 0 & -\frac{12EI_y}{L^3} & 0 & -\frac{6EI_y}{L^2} & 0 \\ 0 & 0 & 0 & -\frac{GJ}{L} & 0 & 0 \\ 0 & 0 & \frac{6EI_y}{L^2} & 0 & \frac{2EI_y}{L} & 0 \\ 0 & -\frac{6EI_z}{L^2} & 0 & 0 & 0 & \frac{2EI_z}{L} \end{bmatrix} = \mathbf{K}'_{x21} \quad \text{Eq. 3-7}$$

$$\mathbf{K}_{x22} = \begin{bmatrix} \frac{EA}{L} & 0 & 0 & 0 & 0 & 0 \\ 0 & \frac{12EI_z}{L^3} & 0 & 0 & 0 & -\frac{6EI_z}{L^2} \\ 0 & 0 & \frac{12EI_y}{L^3} & 0 & \frac{6EI_y}{L^2} & 0 \\ 0 & 0 & 0 & \frac{GJ}{L} & 0 & 0 \\ 0 & 0 & \frac{6EI_y}{L^2} & 0 & \frac{4EI_y}{L} & 0 \\ 0 & -\frac{6EI_z}{L^2} & 0 & 0 & 0 & \frac{4EI_z}{L} \end{bmatrix} \quad \text{Eq. 3-8}$$

The following three equations give the building blocks for the beam element rotated in the y-axis.

$$\mathbf{K}_{y11} = \begin{bmatrix} \frac{12EI_z}{L^3} & 0 & 0 & 0 & 0 & -\frac{6EI_z}{L^2} \\ 0 & \frac{EA}{L} & 0 & 0 & 0 & 0 \\ 0 & 0 & \frac{12EI_y}{L^3} & \frac{6EI_y}{L^2} & 0 & 0 \\ 0 & 0 & \frac{6EI_y}{L^2} & \frac{4EI_y}{L} & 0 & 0 \\ 0 & 0 & 0 & 0 & \frac{GJ}{L} & 0 \\ -\frac{6EI_z}{L^2} & 0 & 0 & 0 & 0 & \frac{4EI_z}{L} \end{bmatrix} \quad \text{Eq. 3-9}$$

$$\mathbf{K}_{y12} = \begin{bmatrix} -\frac{12EI_z}{L^3} & 0 & 0 & 0 & 0 & -\frac{6EI_z}{L^2} \\ 0 & -\frac{EA}{L} & 0 & 0 & 0 & 0 \\ 0 & 0 & -\frac{12EI_y}{L^3} & \frac{6EI_y}{L^2} & 0 & 0 \\ 0 & 0 & -\frac{6EI_y}{L^2} & \frac{2EI_y}{L} & 0 & 0 \\ 0 & 0 & 0 & 0 & -\frac{GJ}{L} & 0 \\ \frac{6EI_z}{L^2} & 0 & 0 & 0 & 0 & \frac{2EI_z}{L} \end{bmatrix} = \mathbf{K}'_{y21} \quad \text{Eq. 3-10}$$

$$\mathbf{K}_{y22} = \begin{bmatrix} \frac{12EI_z}{L^3} & 0 & 0 & 0 & 0 & \frac{6EI_z}{L^2} \\ 0 & \frac{EA}{L} & 0 & 0 & 0 & 0 \\ 0 & 0 & \frac{12EI_y}{L^3} & -\frac{6EI_y}{L^2} & 0 & 0 \\ 0 & 0 & -\frac{6EI_y}{L^2} & \frac{4EI_y}{L} & 0 & 0 \\ 0 & 0 & 0 & 0 & \frac{GJ}{L} & 0 \\ \frac{6EI_z}{L^2} & 0 & 0 & 0 & 0 & \frac{4EI_z}{L} \end{bmatrix} \quad \text{Eq. 3-11}$$

The submatrices of the z-axis rotated beam element are described in the following.

$$\mathbf{K}_{z11} = \begin{bmatrix} \frac{12EI_y}{L^3} & 0 & 0 & 0 & \frac{6EI_y}{L^2} & 0 \\ 0 & \frac{12EI_z}{L^3} & 0 & -\frac{6EI_z}{L^2} & 0 & 0 \\ 0 & 0 & \frac{EA}{L} & 0 & 0 & 0 \\ 0 & -\frac{6EI_z}{L^2} & 0 & \frac{4EI_z}{L} & 0 & 0 \\ \frac{6EI_y}{L^2} & 0 & 0 & 0 & \frac{4EI_y}{L} & 0 \\ 0 & 0 & 0 & 0 & 0 & \frac{GJ}{L} \end{bmatrix} \quad \text{Eq. 3-12}$$

$$\mathbf{K}_{z12} = \begin{bmatrix} -\frac{12EI_y}{L^3} & 0 & 0 & 0 & \frac{6EI_y}{L^2} & 0 \\ 0 & -\frac{12EI_z}{L^3} & 0 & -\frac{6EI_z}{L^2} & 0 & 0 \\ 0 & 0 & -\frac{EA}{L} & 0 & 0 & 0 \\ 0 & \frac{6EI_z}{L^2} & 0 & \frac{2EI_z}{L} & 0 & 0 \\ -\frac{6EI_y}{L^2} & 0 & 0 & 0 & \frac{2EI_y}{L} & 0 \\ 0 & 0 & 0 & 0 & 0 & -\frac{GJ}{L} \end{bmatrix} = \mathbf{K}'_{z21} \quad \text{Eq. 3-13}$$

$$\mathbf{K}_{z22} = \begin{bmatrix} \frac{12EI_y}{L^3} & 0 & 0 & 0 & -\frac{6EI_y}{L^2} & 0 \\ 0 & \frac{12EI_z}{L^3} & 0 & \frac{6EI_z}{L^2} & 0 & 0 \\ 0 & 0 & \frac{EA}{L} & 0 & 0 & 0 \\ 0 & \frac{6EI_z}{L^2} & 0 & \frac{4EI_z}{L} & 0 & 0 \\ -\frac{6EI_y}{L^2} & 0 & 0 & 0 & \frac{4EI_y}{L} & 0 \\ 0 & 0 & 0 & 0 & 0 & \frac{GJ}{L} \end{bmatrix} \quad \text{Eq. 3-14}$$

A code was created that is using these beam building blocks to assemble the global stiffness matrix that is described in the following.

Global Stiffness Matrix Assembly

A mathematical model for the cells can be created consisting of four x-rotated, y-rotated and z-rotated beam elements. To assemble the global stiffness matrix the orientation and the numbering of the cells and nodes needs to be defined.

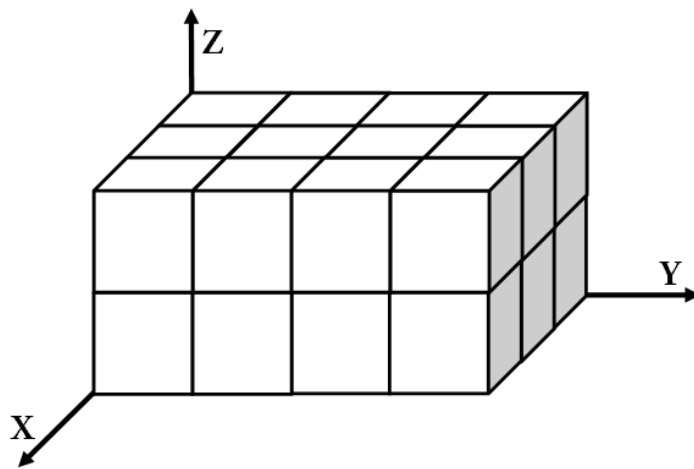


Figure 3-15: Cell Coordinate System and Orientation

Figure 3-15 gives the orientation of the deploying cubes in a local coordinate system. This convention is important to number the nodes and cells appropriately to support the creation of any size of smart structure instantly.

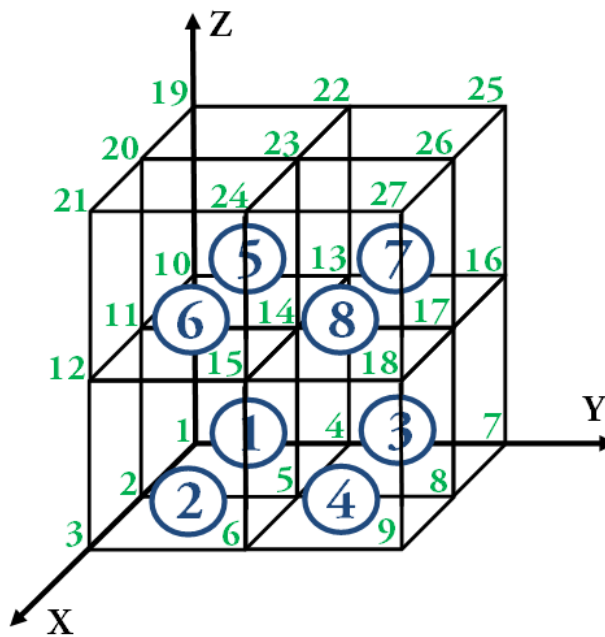


Figure 3-16: Numbering of cells and nodes

The numbering of cells and nodes can be seen in Figure 3-16 for a 2x2x2 box with 8 cells and 27 nodes. The used algorithm associates every cell with the correct nodes and the appropriate beam distribution. This assigns for example the 4th cell in the 2x2x2 array from the nodes 5, 6, 8, 9, 14, 15, 17 and 18. First it is important to determine which beams are connected to which nodes to assemble the global stiffness matrix. From Figure 3-16 it can be seen that the numbering of the nodes in the x-direction continues until the end of the structure is reached while the numbering in y has always a step of the number of nodes in x ($n_{cell,x}+1$). The numbering in the z direction on the other hand shows a gap in the nodal product of nodes in x and y ($(n_{cell,x}+1) \cdot (n_{cell,y}+1)$).

Equation 3-17 for example shows the global stiffness matrix assembly for a three dimensional cube with eight nodes and twelve beam element with four in the x-axis orientation, four in the y-axis and four in the z-axis orientations. Each of the sub matrices in the equations 3.16, 3.17 and 3.18 is a 6x6 matrix calculated with the equations described further on the following pages.

$$\mathbf{K}_{\text{cube}} = \begin{bmatrix} \mathbf{K}_{11} & \mathbf{K}_{12} \\ \mathbf{K}_{21} & \mathbf{K}_{22} \end{bmatrix} \quad \text{Eq. 3-15}$$

$$\mathbf{K}_{11} = \begin{bmatrix} \mathbf{K}_{X11} + \mathbf{K}_{Y11} + \mathbf{K}_{Z11} & \mathbf{K}_{X12} & \mathbf{K}_{Y12} & 0 \\ \mathbf{K}_{X21} & \mathbf{K}_{X22} + \mathbf{K}_{Y11} + \mathbf{K}_{Z11} & 0 & \mathbf{K}_{Y12} \\ \mathbf{K}_{Y21} & 0 & \mathbf{K}_{X11} + \mathbf{K}_{Y22} + \mathbf{K}_{Z11} & \mathbf{K}_{X12} \\ 0 & \mathbf{K}_{Y21} & 0 & \mathbf{K}_{X22} + \mathbf{K}_{Y22} + \mathbf{K}_{Z11} \end{bmatrix} \quad \text{Eq. 3-16}$$

$$\mathbf{K}_{22} = \begin{bmatrix} \mathbf{K}_{X11} + \mathbf{K}_{Y11} + \mathbf{K}_{Z22} & \mathbf{K}_{X12} & \mathbf{K}_{Y12} & 0 \\ \mathbf{K}_{X21} & \mathbf{K}_{X22} + \mathbf{K}_{Y11} + \mathbf{K}_{Z22} & 0 & \mathbf{K}_{Y12} \\ \mathbf{K}_{Y21} & 0 & \mathbf{K}_{X11} + \mathbf{K}_{Y22} + \mathbf{K}_{Z22} & \mathbf{K}_{X12} \\ 0 & \mathbf{K}_{Y21} & 0 & \mathbf{K}_{X22} + \mathbf{K}_{Y22} + \mathbf{K}_{Z22} \end{bmatrix} \quad \text{Eq. 3-17}$$

$$\mathbf{K}_{12} = \begin{bmatrix} \mathbf{K}_{Z12} & 0 & 0 & 0 \\ 0 & \mathbf{K}_{Z12} & 0 & 0 \\ 0 & 0 & \mathbf{K}_{Z12} & 0 \\ 0 & 0 & 0 & \mathbf{K}_{Z12} \end{bmatrix} = \mathbf{K}'_{21} \quad \text{Eq. 3-18}$$

Distortion of the Model

During the simulation, the nodes will move in the global as well as in the local coordinate frame which necessarily means that also the beam elements connected with the nodes needs to be transformed. This transformation is facilitated by using Equation 3-18 on the full global stiffness matrix for each node with the node rotations q_4 , q_5 and q_6 that are rotated with the rotation angles α , β and γ . Figure 3-17 shows the relation between the angles and their rotation axis.

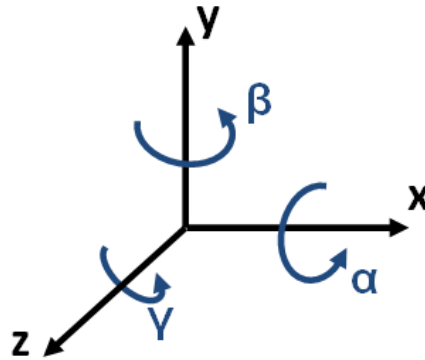


Figure 3-17: Rotation Axes and Angles

The rotation angles come directly from the previous time step of the simulation and are applied first around the z-axis, then y-axis and then a rotation around the x-axis (the beam main axis). The rotation equations can be found in the following.

$$\mathbf{Q} = \begin{bmatrix} \mathbf{Q}_{3 \times 3} & \mathbf{0} \\ \mathbf{0} & \mathbf{Q}_{3 \times 3} \end{bmatrix} \quad \text{Eq. 3-19}$$

$$\mathbf{Q}_{3 \times 3} = \mathbf{Q}_z(\gamma) \cdot \mathbf{Q}_y(\beta) \cdot \mathbf{Q}_x(\alpha) \quad \text{Eq. 3-20}$$

$$\mathbf{Q}_x(\alpha) = \begin{bmatrix} 1 & 0 & 0 \\ 0 & \cos \alpha & -\sin \alpha \\ 0 & \sin \alpha & \cos \alpha \end{bmatrix}$$

$$\mathbf{Q}_y(\beta) = \begin{bmatrix} \cos \beta & 0 & \sin \beta \\ 0 & 1 & 0 \\ -\sin \beta & 0 & \cos \beta \end{bmatrix} \quad \text{Eq. 3-21}$$

$$\mathbf{Q}_z(\gamma) = \begin{bmatrix} \cos \gamma & -\sin \gamma & 0 \\ \sin \gamma & \cos \gamma & 0 \\ 0 & 0 & 1 \end{bmatrix}$$

$$\mathbf{K}_{rot} = \mathbf{Q}^T \cdot \mathbf{K} \cdot \mathbf{Q} \quad \text{Eq. 3-22}$$

This transformation is constantly performed for each beam element and for each simulation time step in the equation of motion using the ode45 solver in Matlab.

Damping Matrix

The damping matrix \mathbf{D} in the equation of motion has the main purpose of making the structure controllable by damping the vibrations within the structure creating an equilibrium condition. In an actual assembled structure multiple factors like interconnects, opening and closing of micro cracks and friction between the structure are contributors to the energy dissipation. It is almost impossible to describe mathematically each of these energy-dissipating term in an actual structure [78]. For this reason, the damping is usually modelled in a highly idealized manner. Therefore for this code, the damping matrix was assumed as directly proportional to the stiffness matrix. Simulations with a fraction of 1/10 to 1/100 between stiffness matrix and damping matrix values obtained good results and controllability. This simplification was used with the justification that the to be simulated structure needs to be treated as a free flying object with only energy dissipation through structural damping. For a more

precise damping behaviour for a specific real application, extensive testing and experimentation is needed.

Mass matrix

The global mass matrix \mathbf{M} is assembled of the mass matrices of all the beam elements in the structure. Assembling the global mass matrix is carried out in a similar fashion as the global stiffness matrix assembly described above. The mass matrix of each beam element [77] distributes the mass over the two nodes and their six degrees of freedom. Each beam element has the same initial properties as can be seen in Equation 3-5.

$$\mathbf{M}_{\text{beam},i} = \rho AL \begin{bmatrix} \frac{1}{3} & 0 & 0 & 0 & 0 & 0 & \frac{1}{6} & 0 & 0 & 0 & 0 & 0 \\ 0 & \frac{13}{35} & 0 & 0 & 0 & \frac{11L}{210} & 0 & \frac{9}{70} & 0 & 0 & 0 & -\frac{13L}{420} \\ 0 & 0 & \frac{13}{35} & 0 & -\frac{11L}{210} & 0 & 0 & 0 & \frac{9}{70} & 0 & \frac{13L}{420} & 0 \\ 0 & 0 & 0 & \frac{I_y + I_z}{3A} & 0 & 0 & 0 & 0 & 0 & \frac{I_y + I_z}{6A} & 0 & 0 \\ 0 & 0 & -\frac{11L}{210} & 0 & \frac{L^2}{105} & 0 & 0 & 0 & -\frac{13L}{420} & 0 & -\frac{L^2}{140} & 0 \\ 0 & \frac{11}{210} & 0 & 0 & 0 & \frac{L^2}{105} & 0 & \frac{13L}{420} & 0 & 0 & 0 & -\frac{L^2}{140} \\ \frac{1}{6} & 0 & 0 & 0 & 0 & 0 & \frac{1}{3} & 0 & 0 & 0 & 0 & 0 \\ 0 & \frac{9}{70} & 0 & 0 & 0 & \frac{13L}{420} & 0 & \frac{13}{35} & 0 & 0 & 0 & -\frac{11L}{210} \\ 0 & 0 & \frac{9}{70} & 0 & -\frac{13L}{420} & 0 & 0 & 0 & \frac{13}{35} & 0 & \frac{11L}{210} & 0 \\ 0 & 0 & 0 & \frac{I_y + I_z}{6A} & 0 & 0 & 0 & 0 & 0 & \frac{I_y + I_z}{3A} & 0 & 0 \\ 0 & 0 & \frac{13L}{420} & 0 & -\frac{L^2}{140} & 0 & 0 & 0 & \frac{11L}{210} & 0 & \frac{L^2}{105} & 0 \\ 0 & -\frac{13L}{420} & 0 & 0 & 0 & -\frac{L^2}{140} & 0 & -\frac{11L}{210} & 0 & 0 & 0 & \frac{L^2}{105} \end{bmatrix} \quad \text{Eq.3-23}$$

In Equation 3.23, $\mathbf{M}_{\text{beam},i}$ is the beam element mass matrix. The matrix gives the mass distribution over the DOF of the nodes creating an inertia for all movements associated with this node. The mass of the beam originates from the scalar term ρAL in front of the matrix, this term will be called $m_{\text{beam},i}$ in the following calculations, $m_{\text{beam},i}$ is a scalar.

$$m_{\text{beam},i} = \rho AL = \frac{1}{12} m_{\text{cell},i} = \frac{1}{12} (m_{\text{cellstruct},i} + m_{\text{gas},i}) \quad \text{Eq. 3-24}$$

For a 3D structure assembled of twelve beam elements, the mass of a single beam element is therefore a twelfth of the mass of the cell $m_{cell,i}$. The mass of each cell itself is made up of the structural mass $m_{cellstruct,i}$ and the inflation gas mass $m_{gas,i}$. The structural mass of each single cell in the structure stays the same but the gas mass changes $m_{gas,i}$ depending on the cells current inflation status therefore the only variable for the mass matrix $\mathbf{M}_{beam..}$.

3.3.2 Adaptive Global Matrices

During the inflation and actuation process, the entities of the mass, stiffness and damping matrix change due to a volume change of its cells. The volume change is undertaken by adding or removing air or fluid. Figure 3-18 shows the principle of the cell expansion by adding gas or fluid mass inside the cells. The figure also shows the initial spherical cell and the modelled cube with its beam elements.

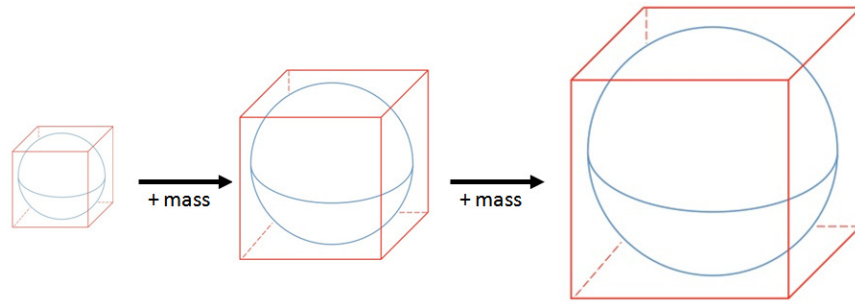


Figure 3-18: Schematic of cell inflation

The size of the cells increases by adding gas or fluid mass to them, the relationship V_{cell} in dependence on $m_{gas,i}$ can be formulated with the ideal gas equation with the Boltzmann constant R , the internal cell pressure p_{cell} and the average cell temperature T_{cell} :

$$V_{cell} = \frac{m_{gas,i}RT_{cell}}{p_{cell}} \quad \text{Eq.3-25}$$

As the cells are made from an ultrahigh elasticity silicon rubber that can expand over the manifold of its initial size, the pressure within the cell is assumed to be constant due to the added gas mass inside the cell counteracted by the increasing volume enabled by

the hyperelastic cell material. The temperature is assumed constant over the inflation and actuation process.

As the cell is inflating, also the material in the cell wall is thinning. The volume of the cell walls is the cell structural volume ($V_{cellstruct}$), similar to the mass of the walls which is also the structural mass of the cells. This can be calculated by using the equations of the surface area of the inflating sphere and the cell wall thickness $t_{cellwall}$. The cells can be treated as spheres with the radius r_{cell} .

$$V_{cellstruct} = t_{cellwall} 4\pi r_{cell}^2 = \text{const.} \quad \text{Eq.3-26}$$

Giving the following relationship between cell wall thickness and sphere radius between state 1 and state 2:

$$\frac{t_{cellwall,1}}{t_{cellwall,2}} = \left(\frac{r_{cell,2}}{r_{cell,1}} \right)^2 \quad \text{Eq.3-27}$$

The equations above give the geometrical basis for the property alteration assessment described in the following subchapters.

The property alteration is carried out for the mass matrix only with the mass changes due to the gas mass that is added or removed by the inflation process. The geometry changes are accounted for in the stiffness and damping matrix. As the developed code uses inflatable spherical cells that are modeled as cubes with beam elements on their edges, the moment of inertia needs to be reformulated to obtain a valid code. In this case, the single cell with its 12 beam elements is the smallest reoccurring element and is therefore used to obtain the properties for every single beam element within the cell. Each cell is modelled with 12 beam elements and every beam element has the same properties. These basic properties can be grouped into the following three categories: geometrical entities like the area of the beam A and the length of the beam L , the material properties like the modulus of elasticity of the material E and the shear modulus G and the inertia terms, like moment of inertia I and the torsional moment J . Their behaviour during the cell inflation is discussed in the next couple of pages.

Area A and Length L

The length L of each beam element changes during inflation of the cells depending on the mass inflow inside the spherical cells and can be calculated using the volume equation of the inflating sphere:

$$L = 2 \sqrt[3]{\frac{3 V_{cell}}{4 \pi}} \quad \text{Eq.3-28}$$

With the modeling approach using a sphere made out of hyperelastic material, the assumption was made that the area of the beam elements A in all three direction stays constant of the sphere. The change in geometry is already accounted for in the variation in the length L .

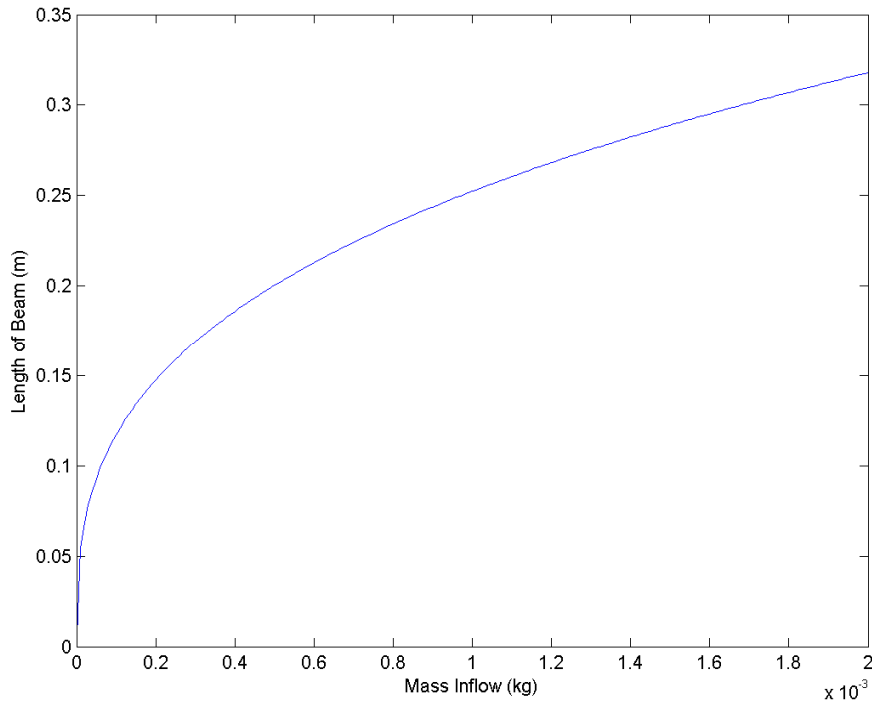


Figure 3-19: Length of beam depending on gas mass inflow

Second Moment of Inertia I_y , I_z and Torsion Moment of Area J

The moment of inertia of a cell with an outer radius r_{cello} , and an inner radius r_{cell} can be calculated with the following sphere equation [79].

$$I_{cell} = \begin{pmatrix} \frac{\pi}{4}(r_{cello}^4 - r_{cell}^4) & 0 & 0 \\ 0 & \frac{\pi}{4}(r_{cello}^4 - r_{cell}^4) & 0 \\ 0 & 0 & \frac{\pi}{4}(r_{cello}^4 - r_{cell}^4) \end{pmatrix} \quad \text{Eq.3-29}$$

with $r_{cello} = r_{cell} + t_{cell}$

To obtain the moment of inertia of the 12 beam elements in all three axes, the moment of inertia of the inflating sphere must be adapted. Figure 3-20 shows the cut through in the y-z plane of the discretized cube model. As the cells were modeled as spheres with identical properties in each direction, the dimensions and orientations will be the same in all planes.

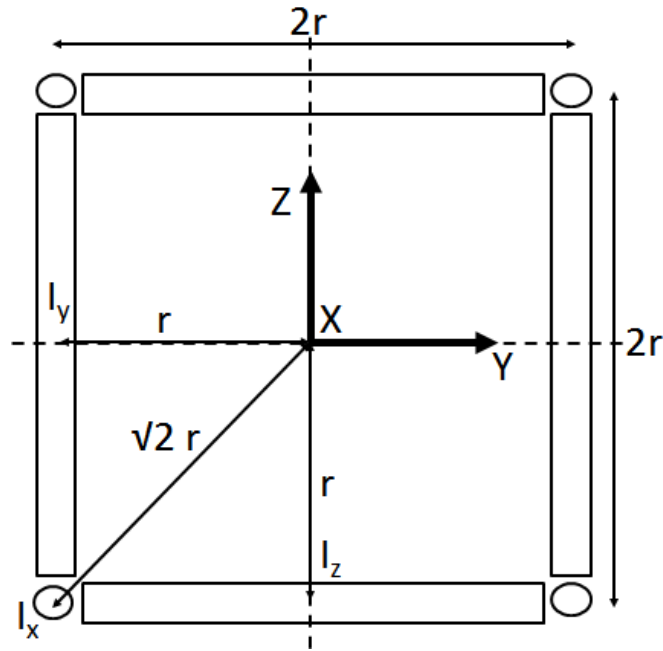


Figure 3-20: Moment of inertia: cross section geometric drawing

The figure shows that there are four beams oriented out of y-z plane in the corners which will contribute to the sphere moment of inertia in x with I_x (also known as polar moment of inertia J). Then there are two times four identical beam elements oriented in

the y and z axis contributing with I_y and I_z . It is to be noted here that all twelve beam elements will contribute.

By using the parallel axis theorem [80] to calculate the moment of inertia in the beam centre can be calculated with the following equation.

$$I = I_{cell} - A_{beam}r_{cell}^2 \quad \text{Eq.3-30}$$

Substituting the parallel axis theorem equation with the positions and distances of the twelve beam elements displayed in Figure 3-20 and setting it equal to the moment of inertia of one of the identical axis of the sphere a relationship to calculate the moment of inertia of the discretised beam elements can be created.

$$\begin{aligned} 4(I_x - 2A_{beam}r_{cell}^2) + 4(I_y - A_{beam}r_{cell}^2) + 4(I_z - A_{beam}r_{cell}^2) & \quad \text{Eq.3-31} \\ = \frac{\pi}{4}(r_{cello}^4 - r_{cell}^4) & \end{aligned}$$

To solve the equation above, the following two relationships need to be used

1. the Moment of Inertia is identical in y and z directions:

$$I_y = I_z \quad \text{Eq.3-32}$$

2. the relationship between the Moment of Inertia in x and z can be formulated as follows with the perpendicular axis theorem [81].

$$I_x = I_y + I_z \quad \text{Eq.3-33}$$

Substituting Equation 3-31 and 3-32 into Equation 3-33, the moment of inertia of each beam element can be calculated depending on the inflation of the cell:

$$I_y = I_z = \frac{\pi}{64}(r_{cello}^4 - r_{cell}^4) + A_{beam}r_{cell}^2 \quad \text{Eq.3-34}$$

$$I_x = J = I_y + I_z = \frac{\pi}{32}(r_{cello}^4 - r_{cell}^4) + 2A_{beam}r_{cell}^2 \quad \text{Eq.3-35}$$

The plot of the moment inertia depending on the volume change due to the gas mass inflow is plotted in the Figure 3-21.

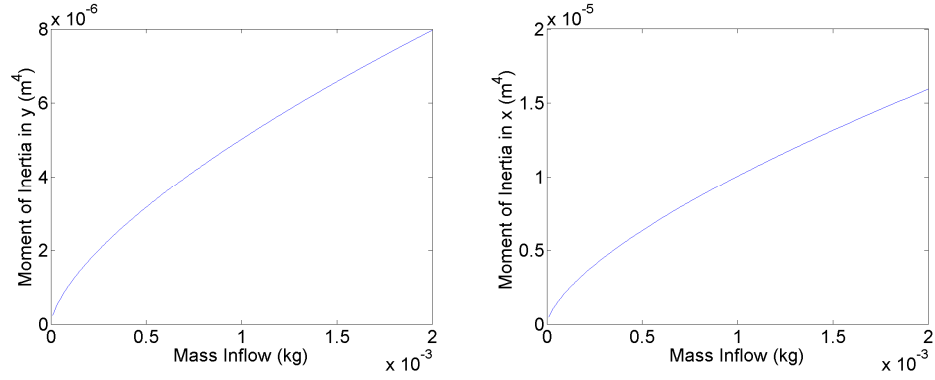


Figure 3-21: Moment of Inertia in x and y depending on the volume increase due to gas mass inflow

Modulus of Elasticity E and Shear Modulus G

The Modulus of Elasticity E and the Shear Modulus G for the hyperelastic material are constant if only the material is considered. Due to the fact that during inflation and actuation, the cell becomes a composite material consisting of the hyperelastic cell wall and the inflated cell core, both properties will become lower as the cell is inflating. This is accounted for by obtaining a specific modulus for the inflating cell which is mathematically expressed via the following two equations.

$$E = \frac{V_{cellstruct}}{V_{cell} + V_{cellstruct}} E_{mat} \quad \text{Eq.3-36}$$

$$G = \frac{V_{cellstruct}}{V_{cell} + V_{cellstruct}} G_{mat} \quad \text{Eq.3-37}$$

In these equations $V_{cellstruct}$ is the volume of the uninflated cell that just consists of hyperelastic material while V_{cell} is the volume of the inflated cell enclosed by the hyperelastic shell. The initial values of modulus of the elasticity and shear modulus E_{mat} and G_{mat} were taken from the literature.

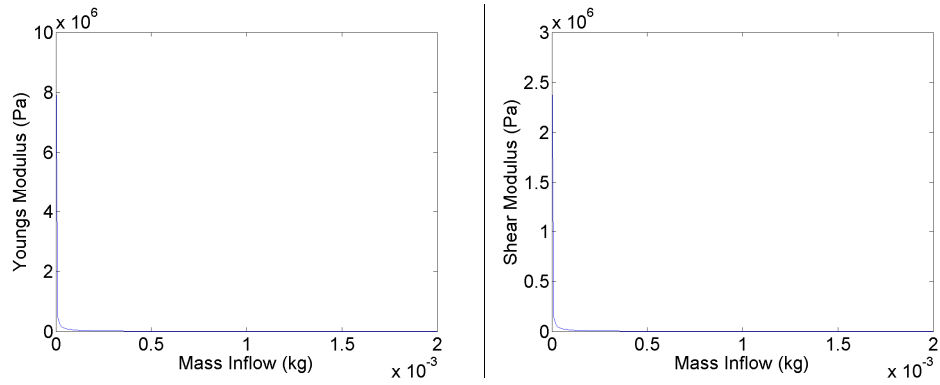


Figure 3-22: Modulus of elasticity and shear modulus depending on gas mass inflow

In the following the downstream effect of property alteration on the deploying structure will be outlined more in detail.

Property Alteration

To better plan for the mission application it is important to understand how a change of properties will affect the shape and the performance of the deployed structure. For this investigation a single cell was used consisting of twelve beam elements with their rotated properties. The cell is free flying in space with no external forces and no actuation forces. The only force acting on the structure is the inflation force which is modelled as a gas mass inflow into the cell.

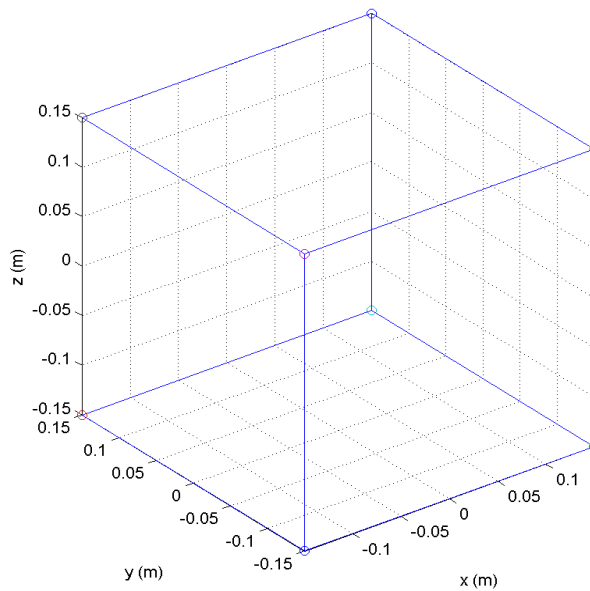


Figure 3-23: Single inflated cell

As mentioned above, each of the blue beam elements in Figure 3-23 are described by their properties E , A , L , I_x , I_y , G and J . It is important to know the impact of changing each of these properties in relation to the deployed structure. For this reason, the following assessment has been carried out to better understand the impact of the changing properties of the beam elements on the behaviour of the full cell (made out of 8 beam elements). The element properties above were obtained by using a static system. In this calculation the developed property equations are included in the dynamic system with the equation of motion in its core. The two main parameters of interest here are the cell dimensions to observe the deployment behaviour of the cells (Figure 3-24) and the frequency behaviour during the inflation (Figure 3-25) to allow drawing conclusions on the structural performance of the deployed structure.

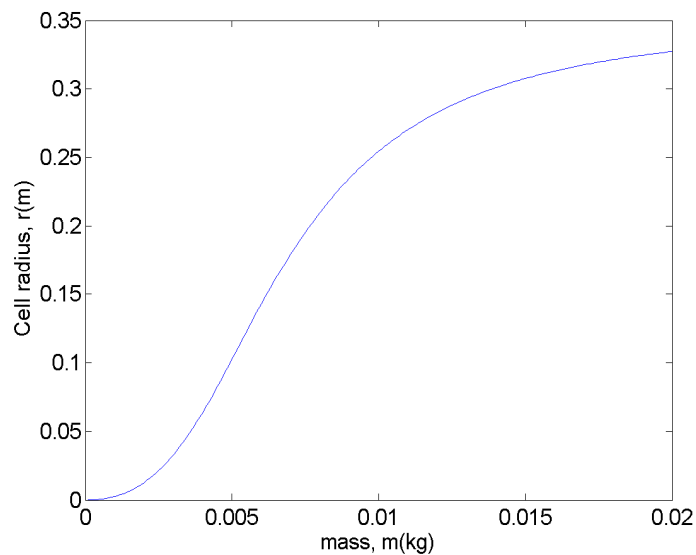


Figure 3-24: Radius of cell over gas mass inflow

The increasing cell size by adding gas mass into the cell displayed in Figure 3-24 models reality very well. In the beginning of the inflation, the walls of the cells are very thick and it takes a considerable amount of gas mass to initiate the deployment. Once this initial inflation period is overcome, the increase in size is almost linear until the cell has such a large volume that the further added mass has no impact on the size of the cell anymore. In reality, the cell will also rupture at some point due to the thinning of the cell walls during volume increase. For the simulations it is considered advantageous to

stay well below this rupture point, therefore the decision was made to stay below 0.25m cell radius to ensure reliability.

As another figure of merit, the eigenfrequency behaviour over the mass inflow is shown in Figure 3-25 for a single cell for the first eigenfrequency of the system. As expected, the frequency decreases with the size of the cells even though that mass is added into the system.

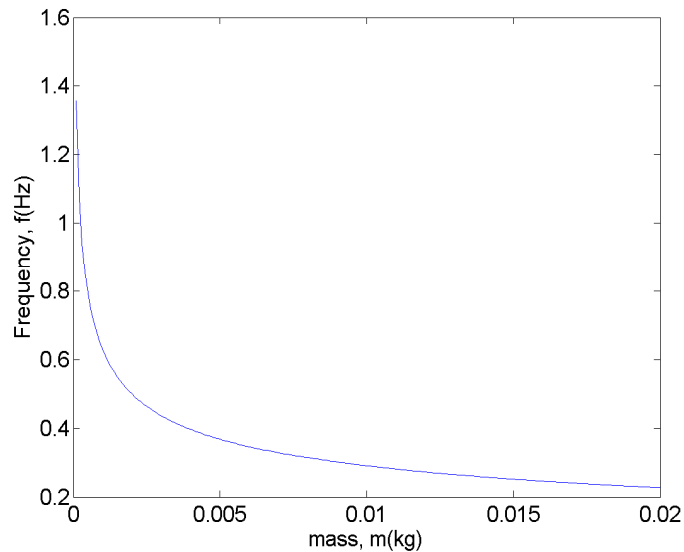


Figure 3-25: First cell eigenfrequency over gas mass inflow

By assessing Figure 3-24 with a maximum cell radius of 0.25 m and therefore a mass inflow of 0.01 kg, the first eigenfrequency range of a single cell can be determined to ~0.3/0.4 Hz in inflated state to ~1/2 Hz in the stored state. This assessment is just considering the cells alone without any attachment or satellite substructure. For the launch the cells will be tightly packed in a storage container significantly increasing the eigenfrequency of the assembly to ensure no interference with the satellite and the launcher.

3.3.3 Forces

The control and alteration of the cells are facilitated over the force entry in the equation of motion. The following subchapters are giving an overview of the used force model to simulate the desired behaviour in the appropriate environment.

$$\mathbf{F} = \mathbf{F}_{\text{int}} + \mathbf{F}_{\text{ext}} \quad \text{Eq. 3-38}$$

The total force can be separated in two forces, the internal forces \mathbf{F}_{int} like inflation and actuation and the external forces \mathbf{F}_{ext} like gravitational forces. The forces are a column vector with the same dimension as the property matrices. Similar to the stiffness matrix, the applied force also needs to be transformed in the appropriate node coordinate system using Equation 3-24 as soon as the structure is being transformed.

Internal Forces

The internal force \mathbf{F}_{int} that is made up of the inflation force deploying the structure and the actuation force changing the shape of the structure. Also the thermal force can be considered an internal force.

1. Inflation Force:

Before inflation, all nodes are located in a centre point (e.g. the pressure storage) with an infinitesimal spacing between them as an initial condition. During inflation the differential pressure inside the cells increases which results in an equally applied force on the walls of the cell. Similar to the internal differential pressure of a plant's cell acting on the walls to sustain the integrity of the cell, the inflation force is modelled as an outward force normal to the walls of the cell. The force acting on the wall surface is then split and distributed equally to the four nodes in the corners of the cell wall.

Figure 3-29 shows the force acting on the walls (blue arrows) and their equal distribution over the nodes (black arrows). The forces in the nodes are always in the

global coordinate system which requires a coordinate transformation of the pressure force in case the cells are deformed or distorted.

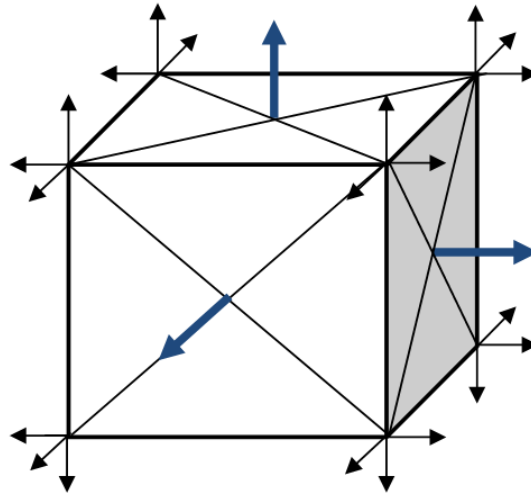


Figure 3-26: Force model of one cell

The code evaluates each nodal cell connection and sums up all the applied forces in a line of connected nodes and applies it to the nodes on the edges of inflating cells. It is also possible to simulate broken cells within the array to observe the deployment behaviour and the obtained shape. The forces acting on each of the nodes can be calculated by using the equation provided below. The equation was derived using the fact that the gas inside applies a pressure with a force against each wall. By substituting the pressure with the force per wall in the ideal gas equation presented in Equation 3-1 and the assumption that each wall has 4 nodes at its corners separated by the distance d , the following equation can be developed.

$$F_{node} = \frac{3}{8} m_{gas} \frac{RT_{cell}}{r_{cell}} \quad \text{Eq. 3-39}$$

The nodal force originates from the pressure that the fluid molecules apply on the inner surface of the cells. In the equation, m_{gas} is the mass of fluid within the cell and therefore the main parameter that is used for the inflation/actuation. R is the Boltzmann constant, T_{cell} is the temperature and r_{cell} is half the edge length of the cell between two nodes. During the inflation and actuation this distance also changes depending on the stiffness of the cell material. The force is calculated for each node in each of the three

directions creating a force vector with 24 values which is the number of nodes per cell (3D: 8 nodes/cell) times the translation degrees of freedom (3 DOF). The equation below shows the force vector for one three dimensional cell, the numbering and the direction convention can be found in Figure 3-15.

$$\mathbf{F}_{\text{cell}} = \begin{bmatrix} -F_{\text{node}} & -F_{\text{node}} & -F_{\text{node}} & F_{\text{node}} & -F_{\text{node}} & -F_{\text{node}} \dots \\ -F_{\text{node}} & F_{\text{node}} & -F_{\text{node}} & F_{\text{node}} & F_{\text{node}} & -F_{\text{node}} \dots \\ -F_{\text{node}} & -F_{\text{node}} & F_{\text{node}} & F_{\text{node}} & -F_{\text{node}} & F_{\text{node}} \dots \\ -F_{\text{node}} & F_{\text{node}} & F_{\text{node}} & F_{\text{node}} & F_{\text{node}} & F_{\text{node}} \end{bmatrix} \quad \text{Eq. 3-40}$$

To account for distorted cells, the cell force is then rotated in the correct orientation by using the rotation equation outlined in Equation 3-22 in Chapter 3.2.

To obtain a global force vector the sum of the forces at each node is established. The number of columns in the global force vector is the number of nodes in the structure times the dimensions. So if the three dimensional structure would have two cells with one shared cell wall, this would mean that the vector would have 36 columns.

$$\mathbf{F}_{\text{global},i} = \sum_{j=0}^3 \mathbf{F}_{\text{cell } i,j} \quad \text{Eq. 3-41}$$

In the equation i stands for the number of nodes while j stands for number of directions.

The inflation force has a linear slope for a constant time t . After inflation is complete, the differential pressure stays constant but it is also possible to apply a leakage to certain cells or the entire array of cells. In practice, this leakage could be caused by micrometeoroid impacts, fabrication errors, degradation of materials, or natural leakage of an inflatable in the space environment.

As described above, the structure deploys from a single point which corresponds to the stored configuration. The inflation time was taken as four seconds which only impacts the damping characteristics of the structure. For this deployment demonstration it is assumed that every cell is fully functional and that the inflation force is the same for all the cells.

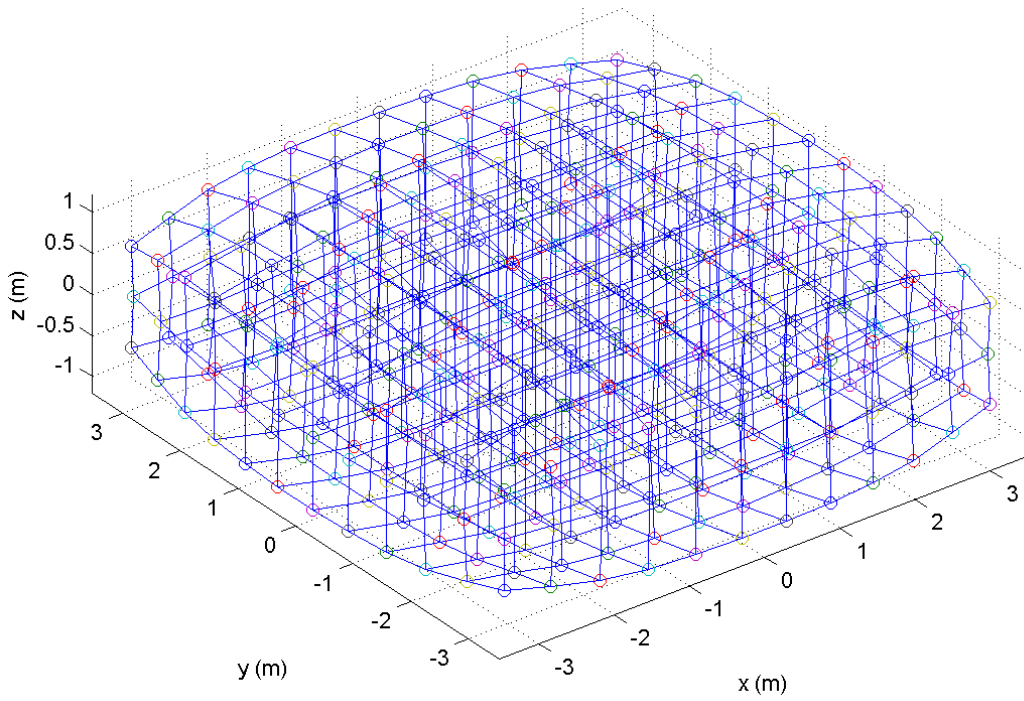


Figure 3-27: Inflated 11x11x2 cell array

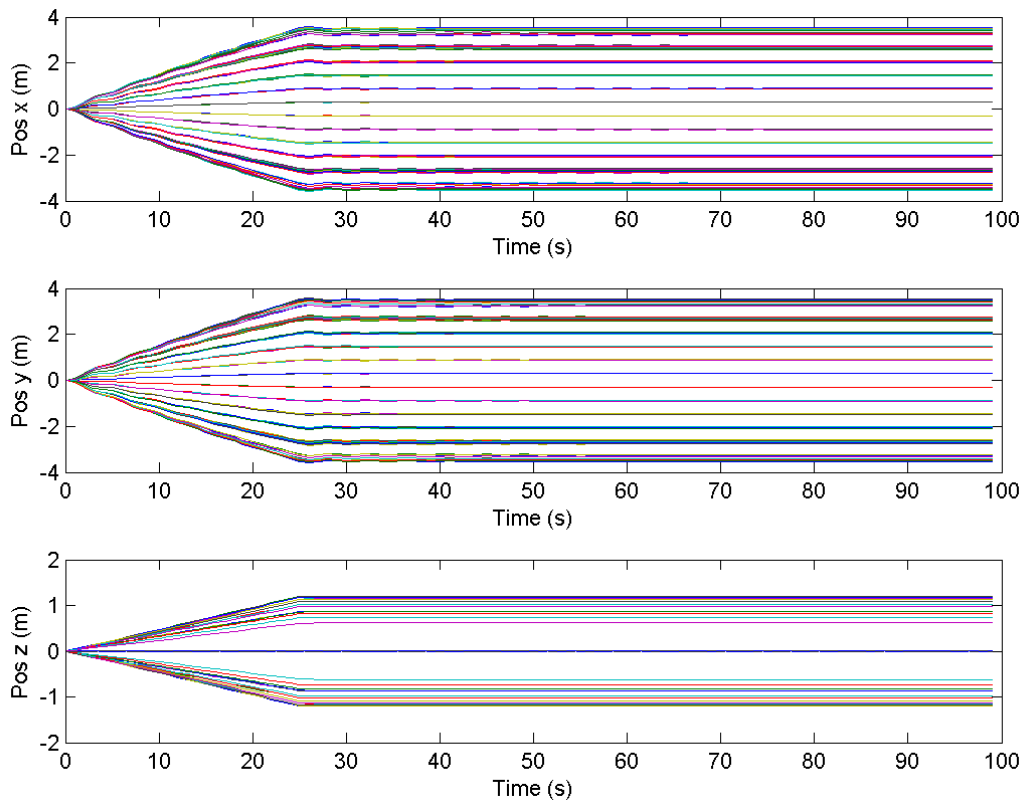


Figure 3-28: Displacement of x and y and z-position

Figure 3-27 shows the inflated array after the oscillation of the array due to inflation died down. It can be seen that a flat sheet is formed in the xy-plane after substituting the

boarder cells and the edge effects. The edge effect of the boarder cells inflated to a smaller volume than the centre cells comes from the modeling of the cells. The walls between the cells as well towards the edge have the same wall thickness. When inflated with the same pressure, the cells form a curved shape towards the edge. This can be seen in nature and the hyperelastic cell benchtest samples as well as in the simulation (e.g. in Figure 3-27). The displacement of the deploying structure separated in the three axes can be seen in Figure 3-28. Each line in the plot corresponds to one node of the 432 nodes in the model, due to the fact that perfect inflation was assumed, all the nodes in each direction are overlaying each other. Figure 3-28 shows that for the first seconds after the inflation, the structure is oscillating a bit but it's dying down due to damping.

2. Actuation Force:

The actuation of the structure is triggered by changing the pressure within the cells which causes a shape change of the cell membrane. The actuation force is applied in a similar manner to the inflation force. The actuation force is, depending on its application, added or subtracted from the inflation force. If only pumps between the cells are used, it is important that the fluid mass budget stays in equilibrium meaning that if one cell gets inflated another one needs to be deflated with the same amount of gas. This force can be applied in a specific pattern to trigger a particular response, for example if the membrane sheet should be folded along one line, this line of cells can be actuated. If micro pumps between the cells are used the air mass is getting transferred between neighbouring cells which makes one cell inflate and the other deflate. On the other hand if valves are used, the air mass is transferred only to the cells with a lower pressure until the system is in equilibrium.

After the deployment through inflation formed a flat sheet, the cells are being actuated to form the desired shape. For the actuation the top cells pump air molecules to the bottom cells to create a positive curved surface. To change the curvature of the dish, the structure was actuated twice with the second actuation cycle having twice the air

mass exchanged from the top to the bottom layer. The following simulation was carried out with a 11x11x2 cell array. The following figure shows the central 9x9 cells of the actuated structure without the border cells (without edge effects).

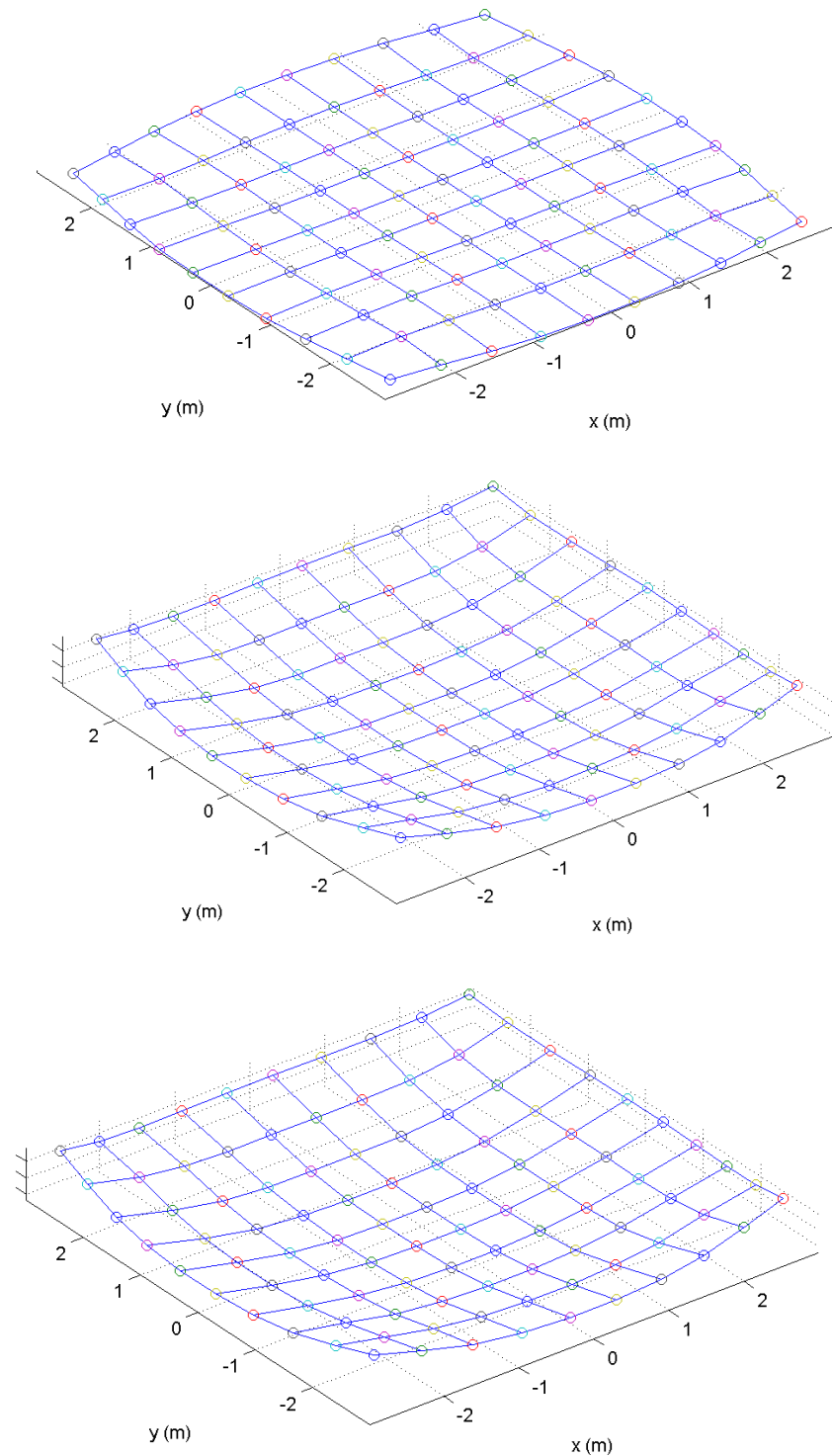


Figure 3-29: Top central 9x9 array of deploying structure: a) inflated structure, b) structure actuated once and c) structure actuated twice

Figure 3-29 shows the evolution of the deformation due to actuation. To increase the readability of the graphs, only the top layer of the full array without the border cells. The array in Figure 3-29a shows the inflated structure, Figure 3-29b is the array after being actuated once and Figure 3-29c shows the increased curvature of the structure after being actuated twice.

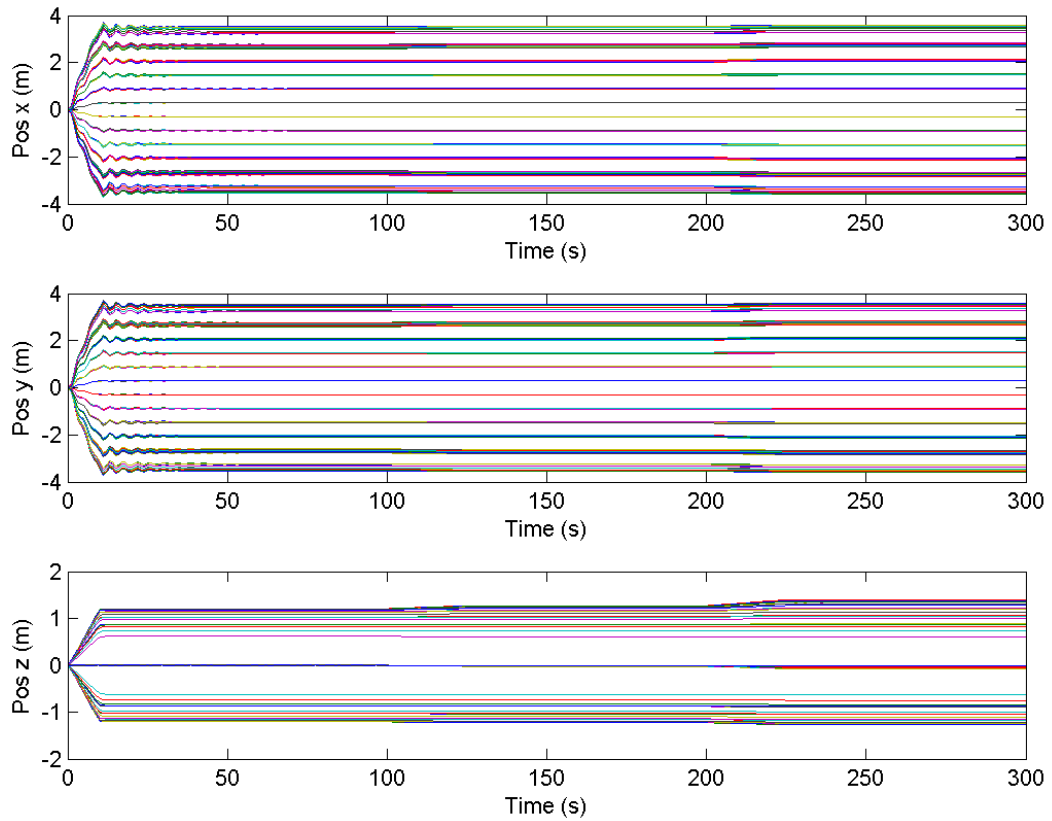


Figure 3-30: Displacement plot of actuated structure

The position over time of all the nodes can be seen in Figure 3-30. In the first ten seconds of the simulation the structure was inflated homogenously. After the oscillation has mostly settled down, the first actuation was started at 100 seconds with a linear increase for 25 seconds. The second actuation started at 200 seconds and also lasted again for 25 seconds with a linear increase.

3. Thermal Force:

The thermal force has an external source but acts as an internal force due to expansions and contractions that occur inside the structure. The thermal force is the force that is introduced in the structure due to thermal gradients. Figure 3-31 shows the temperature gradient principle of the modeled structure. In this example a increased temperature is applied to node 9 resulting in a temperature gradient between node 9 and 6, 6 to 3 and so on. From the heat source (e.g. heating up from the sunlight), a heat flux is calculated through the structure giving each beam element of the cells the according temperature difference and thereby different forces. These forces are applied directly on the beam elements in opposite directions on the nodes.

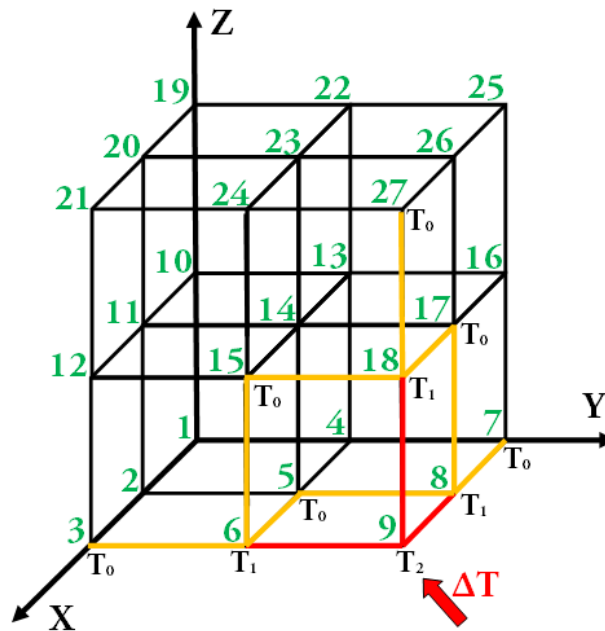


Figure 3-31: Thermal force distribution in model

The internal force caused by the thermal gradient can be calculated for each beam element with the following equation:

$$F_{thermal} = \sigma A_{beam} = E \varepsilon A_{beam} = E (C_{TE} \Delta T) A_{beam} \quad \text{Eq. 3-42}$$

Where σ is the stress due to temperature expansion E is the Youngs Modulus of the beam, ε the strain, C_{TE} the temperature expansion coefficient, A is the cross section area

of the beam and ΔT the temperature difference between two beam nodes (e.g. $\Delta T_{9,6} = T_2 - T_1$ between the node 9 and node 6 in Figure 3-31).

External Forces

Depending on the environment the structure is operated in, the external forces may vary. The main two environments described here are the space and terrestrial environments. Based on the nature of the application, some forces may only be applied to mass nodes, other forces may act on the inside walls, and others are just applied to one surface on the outside of the structure.

1. Gravitational Force and Centrifugal Force:

In space, the main external force applied to the structure is gravity, which may include a gravity gradient for very large structures. Even small gravity gradients can affect the structure due to its low differential pressure and lightweight nature. The gravitational force is applied to each node towards the center of gravity with a value changing depending on the distance between the cells. The gravitational force at each node changes at each time step due to the shifting mass during actuation; this is done through the adaptive mass matrix described earlier. Also due to the fact that each node has a different distance from the centre of mass, the differential gravity effect acts on the structure which is calculated for each node continuously with the following equation.

$$F_{diffgravity,node} = - \frac{G_C m_{body} m_{node}}{r_{body-node}^2} \quad \text{Eq. 3-43}$$

Where G_C is the gravity constant, m_{body} is the mass of the body that's being orbited, m_{node} is the current mass distributed to the node at this point in time and $r_{body-node}$ is the the three dimensional distance between the centre of mass of the body and the node which is taken from the previous time step of the simulation.

For objects that are orbiting a large mass body with a velocity v , the gravitational force is balanced by the centrifugal force (equation below) keeping the object in its circular trajectory.

$$F_{centrifugal} = \frac{m_{node} v}{r_{body-node}} \quad \text{Eq. 3-44}$$

In the code, the centrifugal force does not need to be modeled as it a result of the orbit simulation when the structure is placed at an distance $r_{body-node}$ with the velocity v perpendicular to the gravity force vector in the beginning of the simulation.

2. Atmospheric Drag and Solar Radiation Pressure:

Other perturbing forces are solar radiation pressure (SRP) and atmospheric drag which apply a force on the surface of the structure. In order to model these forces in the code, only the nodes on one surface experience the force.

$$F_{atmdrag} = \frac{1}{2} \rho v^2 C_D A_D \quad \text{Eq. 3-45}$$

Where ρ is the density of the air, v is the velocity of the space craft, A_D is the reference area and C_D is the dimensionless drag coefficient which is related to the object's geometry and surface friction. The air density is calculated using the COSPAR International Reference Atmosphere 2012 (CIRA-2012) Model [82] and its value highly depends on the solar activity. At high solar activity, the atmosphere expands and the space craft experiences a higher drag force. On the other hand at lower solar activity, the space craft experiences less drag force.

These forces depend on the orientation and the shape of the structure as well as the source of the external force. Figure 3-32 shows the force application points for the different external forces. In this example a three cell structure is moving from left to the right while getting propelled by solar radiation pressure, decelerated by atmospheric drag and pulled downwards by gravity. Due to the fact that the orientation of the structure changes in every instance, Figure 3-32 only gives the application forces for this specific

time instance where the solar radiation and drag are opposite each other and gravity perpendicular to both of them. It can be seen that even though the forces act on a surface or a mass, the forces in the model are distributed over the nodes of the different cells. These forces are depending on the orientation and the shape of the structure.

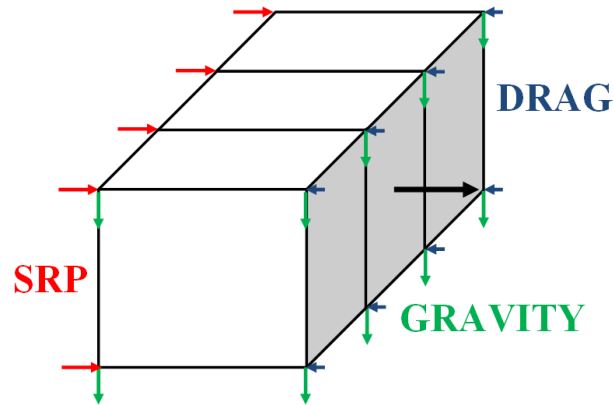


Figure 3-32: External force application areas at specific instance

Other forces that can be applied to the model are short term impact forces, for example meteoroids or space debris.

3.4 Control

The definition of a smart structure says that the structure should be able to respond to a given stimulus in a desired fashion. To realize this, the structure needs to consist of a sensor that measures the displacement, the structure that can alter its shape and a controller that accounts for environmental effect to ensure the final shape of the structure is as desired.

As a controller for the structure a simple PID controller was implemented that uses the control variable for actuation force F_i at the time step i , the actuation force for the next time step F_{i+1} can be calculated by using the discrete velocity algorithm PID controller Equation 3-46 (source [83]).

$$\mathbf{F}_{i+1} = \mathbf{F}_i + K_p \left(1 + \frac{\tau}{K_i} + \frac{K_d}{\tau} \right) \mathbf{e}_i - K_p \left(1 + 2\frac{K_d}{\tau} \right) \mathbf{e}_{i-1} + \frac{K_d}{\tau} \mathbf{e}_{i-2} \quad \text{Eq. 3-46}$$

The error \mathbf{e} in the PID controller equation is the difference between the desired position and the actual position at the certain time step and was used during every time step of the simulation to obtain the corrected force input for the next simulation step. To tune the controller the proportional, integer and differential terms are used where K_p is the proportional factor, K_d the differential factor, K_i is the integral factor and τ is the time interval between two control steps. With this set up it was possible to investigate if the actuation of the structure alone would be enough to overcome the influences of external perturbations on the global structure.

The error term \mathbf{e} is the distance between the actual z-position of the structure's surface and the surface of a sphere section that has the focal point in its centre. The control force \mathbf{F}_i is the actuation force of each of the cells. The equation of motion (Equation 3-4) is now continuously solved in a loop with the changing control force based on the error of the previous two control cycles until the error has reached the desired value.

As an example, to show the capability of the PID controller for use with this code, the shape adaption of an array of cells shall form a part of a sphere (Figure 3-33) with the radius r_{sphere} .

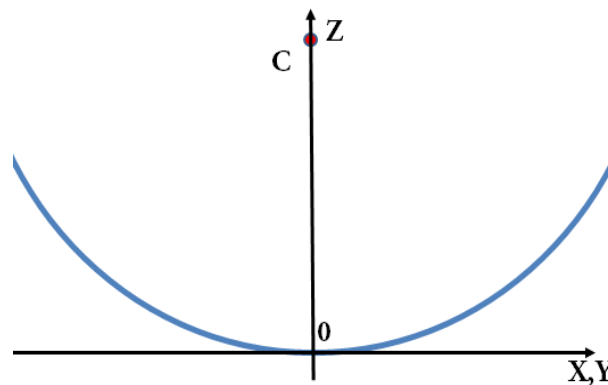


Figure 3-33: Schematic of spherical concentrator

The equation below was used to calculate the required z coordinate for each cell based on its x and y coordinates and as well as the radius of the sphere r_{focal} in which center the focal point lies.

$$z = \sqrt{r_{sphere}^2 - x^2 - y^2} \quad \text{Eq. 3-47}$$

For this simulation, a 9x9x2 cell array was used in order to reduce the computational time required to run each loop of the control cycle. A spherical radius of 5m was used in this example. Using Equation 3-47, the necessary z displacement of all cells can be calculated, compared to the existing displacement and an error term ϵ can be created. For the comparison between the simulation results and the shape of the sphere, the coordinate system is in the centre of the reflector. This origin is marked with a 0 in Figure 3-33, C stands for the centre of the sphere.

x/y	1	2	3	4	5	6	7	8	9
1	-60.6%	-47.7%	-36.2%	-22.5%	-15.2%	-18.9%	-31.1%	-44.0%	-53.9%
2	-47.7%	-30.6%	-18.2%	-4.2%	3.2%	-0.5%	-12.8%	-26.6%	-40.4%
3	-36.2%	-18.2%	-5.0%	9.4%	16.9%	13.2%	0.4%	-14.0%	-28.9%
4	-22.5%	-4.2%	9.4%	24.1%	31.7%	27.9%	14.9%	0.1%	-15.3%
5	-15.2%	3.2%	16.9%	31.7%	39.4%	35.6%	22.5%	7.4%	-8.0%
6	-18.9%	-0.4%	13.2%	27.9%	35.6%	31.7%	18.7%	3.7%	-11.6%
7	-31.1%	-12.8%	0.4%	14.9%	22.5%	18.7%	5.8%	-8.9%	-24.0%
8	-44.0%	-26.6%	-14.0%	0.0%	7.4%	3.7%	-8.9%	-23.1%	-37.5%
9	-53.9%	-40.5%	-28.9%	-15.3%	-8.0%	-11.7%	-24.0%	-37.5%	-50.7%

Figure 3-34: z-position error for each of the 81 cells at start of control cycle

Figure 3-34 shows the normalized difference in percentage of the existing to the desired z-position of all the 81 cells. 100% is the maximum (+40% at the 5x5 cell in the centre) minus the minimum error (-60% at the 1x1cell in the top left corner). In the code the x and y position of all the cells are continuously calculated and the difference between the existing position and the desired position is the error for the PID controller. The goal was to find an actuation pattern that would obtain this shape with the help of the controller. The PID controller was converged with the parameters set to $K_p = 0.5$ (proportional gain), $K_d = 0.1$ (derivative gain) and $K_i = 0.5$ (integral gain). Figure 4-16 shows the resulting z-position error in meters of the 81 cells after 100 control cycles. In

order to provide the error of the two previous time steps at the beginning of the simulation, the first three error values are identically and are obtained by calculating the positions of the single cells without any control applied to them.

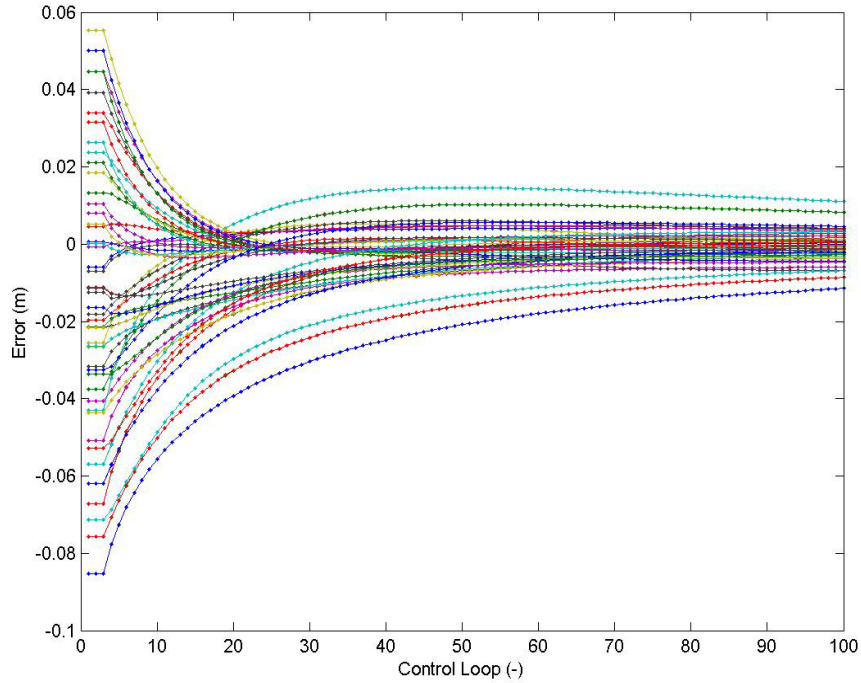


Figure 3-35: Development of error over 100 control loops

It can be seen in Figure 3-35 that most of the errors are approaching zero. Similarly to the error at the beginning of the simulation shown in Figure 3-34, the error at the end of the simulation can be seen in Figure 3-36 as a percentage of the total z-position error from the perfect sphere at the beginning of the simulation.

x/y	1	2	3	4	5	6	7	8	9
1	-8.2%	2.0%	-4.2%	-1.8%	-1.4%	-2.2%	-2.6%	-0.9%	-6.1%
2	2.0%	7.9%	0.4%	2.9%	2.9%	2.4%	2.7%	5.9%	2.2%
3	-4.2%	0.4%	-4.9%	-1.6%	-1.7%	-2.5%	-3.2%	-1.0%	-3.3%
4	-1.8%	2.9%	-1.6%	1.2%	0.8%	0.3%	-0.2%	1.5%	-1.2%
5	-1.4%	2.9%	-1.7%	0.8%	0.4%	0.0%	-0.2%	1.5%	-0.8%
6	-2.2%	2.4%	-2.5%	0.3%	0.0%	-0.5%	-0.8%	0.9%	-1.4%
7	-2.6%	2.7%	-3.2%	-0.2%	-0.2%	-0.8%	-1.2%	0.6%	-2.0%
8	-0.9%	5.9%	-1.0%	1.5%	1.5%	0.9%	0.6%	3.3%	0.5%
9	-6.1%	2.2%	-3.3%	-1.2%	-0.8%	-1.4%	-2.0%	0.5%	-4.9%

Figure 3-36: z-Position error for each of the 81 cells at the end of the control cycle

Through the PID controller it was possible to greatly decrease the error especially in the centre of the reflector. There is still an error of 6-7% in the corners but it is considered that these 4-6 cells are only a small percentage of the total of 81 cells.

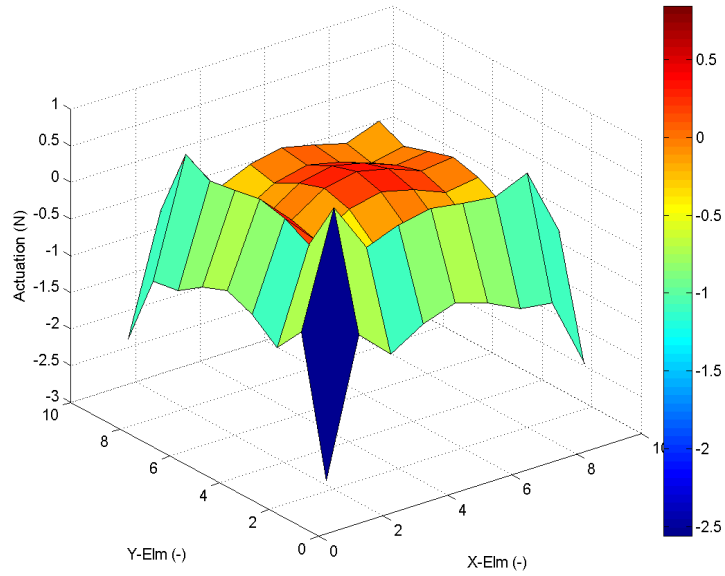


Figure 3-37: Actuation of cells for at the end of control cycle

The actuation of the top cell layer is shown in Figure 3-37. This actuation at the end of the inflation leads to a concentration of the cells normals at the focal point ($r_{focal} = 5\text{m}$) with a radius of just 0.2m. This concentration is displayed in Figure 3-38.

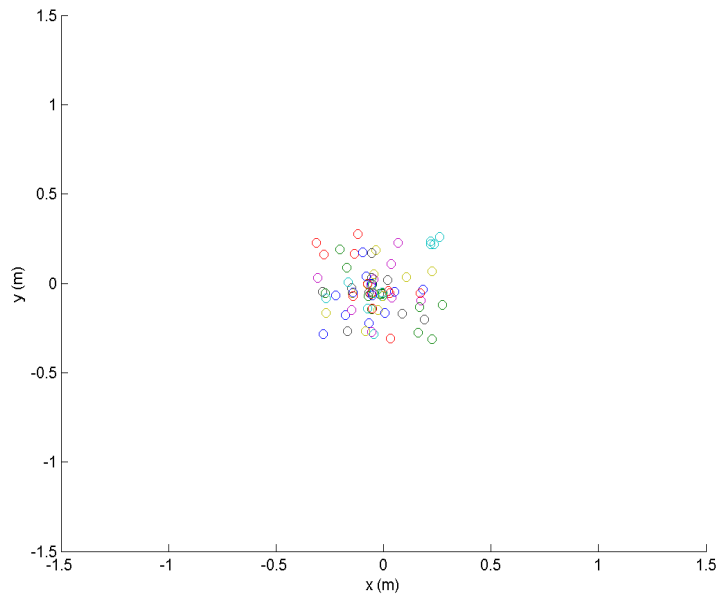


Figure 3-38: Position of all cell normals at the focal point ($r_{focal} = 5\text{m}$)

The shape changing structure together with the PID controller were able to alter the shape of the structure to maximise the focus of the concentrator and reduce the focal length from 30m to just five meters.

In Chapter 4.2.2, the applicability of this control algorithm to control the shape of a paraboloid reflector is presented as part of one of the applications of the developed structure

Chapter IV

Simulations and Experiments

The developed smart structure and simulation code has numerous applications due to the structure's scalability from atom size self-assembling and deforming nano machines up to cells in the range of several hundred meters to form very large space structures. These range from applications such as smart reflectors and concentrators that can change their focal point over shape shifting solar sails that adjust the area of the sail subjected to the solar wind to steer the spacecraft to large appendices like beam elements that have the capability to change their properties to immediately correct for perturbations.

This chapter is structured in a way that first the concept of assembling very large structures in space using self-contained colonies is outlined. To further increase the area to weight ratio of these colonies the use of disaggregated electronics on their surface enabling a satellite without any dead structural mass is envisioned.

The main two applications that are discussed in more detail in the following are shape changing reflectors and beam elements. The subchapters are structured that first the design and system concept is outlined and then a simulation to observe the capability of the structure in a space like environment is carried out. Furthermore, the experiments had the purpose to validate the developed concepts are presented as well. The first experiment is StrathSat-R focusing on the deployment of a concentrator investigating the residual air inflation and actuation. The second experiment iSEDE was inspired by a beam design as an all inflatable satellite investigating disaggregated electronics and hyperelastic actuator application.

4.1 Large Smart Structure Assembly in Space

The proposed design is a light weight flexible structure with low storage volume and high deployed volume which has the ability to change its global shape in space. The

global structure is made up of a number of similar self-controlling cellular colonies deployed from a payload fairing, with only a small fraction of the volume of the deployed structure [84]. There are various options to deploy and assemble these colonies to create the full structure in orbit. One option would be to stack rigid modular components in the launcher payload fairing to make use of the maximum available volume. These rigid or semi rigid components are then assembled in orbit; a well-known example of this in-orbit assembly is the International Space Station which required multiple launches during its construction. The option shown in Figure 4-1 is to deploy hundreds of cellular colonies in a single launch and then inflate them with the desired cellular configurations. A construction robot can then assemble the global structure from the free flying colonies. The advantage of this approach is that the assembly robot can inspect the structures before assembly and use only the colonies which are fully functional. The assembly robot can also be used to reconfigure the structure and exchange broken components.

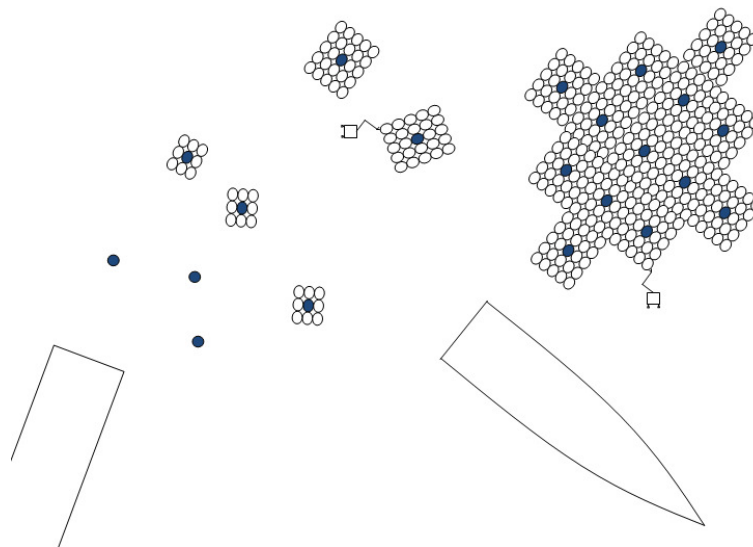


Figure 4-1: Schematic of deployment option 1 with the release of colonies from launcher and assembly via free-flying robot.

Another option (shown in Figure 4-2) would be to eject an assembly robot that has a storage unit filled with stored colonies. After the robot reaches the desired orbit, it will start releasing colonies one after another, letting them inflate and inspecting them for

possible damage. The robot can hold on to the assembled structure, inspect the newly deployed colony and add it to the assembled structure.

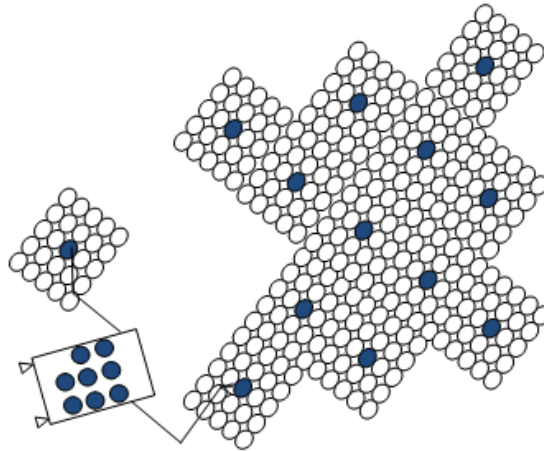


Figure 4-2: Schematic of deployment option 2 with the release of colonies from launcher and assembly via free-flying robot.

Deploying the structure already fully assembled would be also an option. This option would make an assembly robot unnecessary; however, the danger of permanent entanglement is substantial, especially when deploying very large structures. The final selection of the deployment concept is highly dependent on the selected application and needs to be further evaluated for each mission separately.

The main concept of the colony design is that a number of colonies, each composed of a number of individual cells, will be assembled together in space to form a global structure. Each colony is either a two dimensional plane or a three dimensional cube, made up for example of a 5×5 or a $5 \times 5 \times 5$ array (x,y,z) of inflatable cells respectively, surrounding a central pressure source. The modular colonies as well as the cells are scalable to be adapted to a desired application ranging from nano scale (within fabrication constraints) to macro scale. The high pressure source is filled at the beginning of the mission and uses the gas stored in the pressure tank to inflate individual cells and change the overall shape of the structure until the tank is empty. To deflate a cell, gas is released into space via exit valves. Each cell is connected via MEMS valves [85] either to neighbouring cells, to the central pressure source, or to the external

environment. The cells are therefore inflated and deflated by redirecting the gas from the central source through the colony or releasing it to the environment. Figure 4-3 shows one smart element in a 3D structure; the central cell (blue) is connected to the pressure source and is surrounded by hyper-elastic cells with six MEMS valves each. Neighbouring cells are fastened together with mechanical MEMS interconnects, allowing gas to flow through integrated micro valves. Electrical routing to a central controller and intercellular electrical interconnects are also present on each cell.

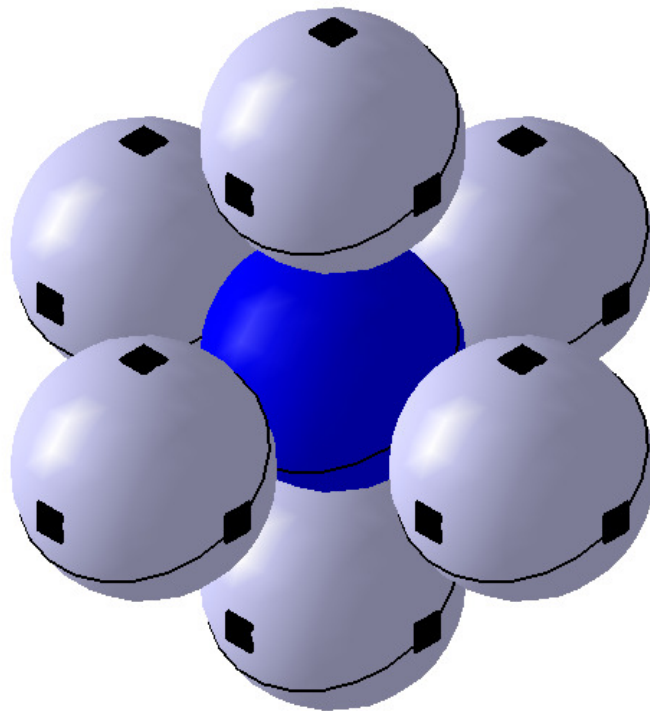


Figure 4-3: 3D realization of one cell connected to pressure source (centre) surrounded by inflatable cells connected via MEMS valves (remaining cells of 5x5x5 cube are hidden for better visualisation)

The complexity of the system, and to some extent the weight, is highly dependent on the number of valves in the system. The hard design requirements are that every cell is accessible by the central pressure source by some path through neighbouring cells, and that any configuration of cells being inflated or deflated is achievable. There is an inherent trade-off in the design process; the approach that uses the fewest number of valves, thus reducing the mass and the complexity of the structure, is also the approach

that uses the most gas since more complex valve operations are required, with more operations requiring that the gas be vented into the environment. On the other hand, the approach with a valve on each cell side, meaning each cell can exchange gas flow with all of its neighbours, makes the whole structure comparatively heavy and complex. Several basic connection valve architectures, shown in Figure 4-4, are discussed to demonstrate examples of these design considerations.

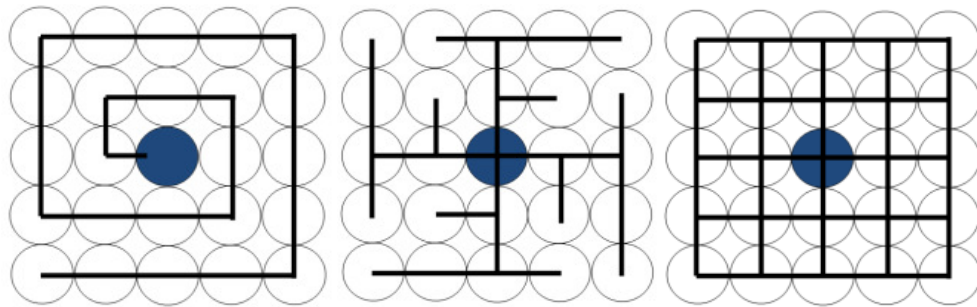


Figure 4-4: Single path vs. tree path vs. full path (blue cell in centre: pressure source)

The three path types considered are the single path with just two valves on each cell for 2D and 3D colonies, the full path with 4 valves in 2D (6 in 3D) and the tree solution in-between with three to four valves.

The amount of actuation and therefore the amount of used gas mass highly depends on the application and planned mission. For example if the mission is quite short, it may be better to use a design that requires fewer valves, since more of the gas would be expendable. On the other hand, a larger mission with many dynamic reconfigurations of the structure would require a large amount of gas; to minimize wasted gas in this case, it would be more feasible to increase the number of valves and complexity in the design. Essentially, each mission must minimize cost as a function of gas mass, valve mass, and complexity.

In order to compare the different architectures, a worst case scenario checkerboard pattern was selected as an actuation pattern. To achieve a checkerboard pattern, where each cell is in a state alternate to its nearest neighbours, then the number of operations and the path of the gas will be different in each architecture. Figure 4-5 shows the number of valves required in each architecture, as well as the number of gas units

required to achieve this pattern due to inflation and deflation operations. Note that in this analysis, it is assumed that the only outlet valve allowing the gas to escape to environment is at the central cell. To achieve the checkerboard pattern, for example in the single path approach, all the cells have to be inflated first until the air reaches the last cell. Following this the air from all the cells except of the last one will need to be released from the centre cell and is therefore lost. To inflate the third last cell in order to create the desired pattern all cells until the third last cell needs to be inflated again and so on. Depending on the cost function (as yet undetermined) which operates based on the cost of gas and the number valves, it can be seen that there will be a large difference between the Single and Full architectures for this application.

The amount of used gas can be further reduced by adding an outlet valve to each cell to release the gas into outer space. By adding these outlet valves, each cell can deflate by itself and is not required to deflate all the surrounding cells. The same analysis except with outlet valves at each cell of the checkerboard pattern can be also seen in Figure 4-5.

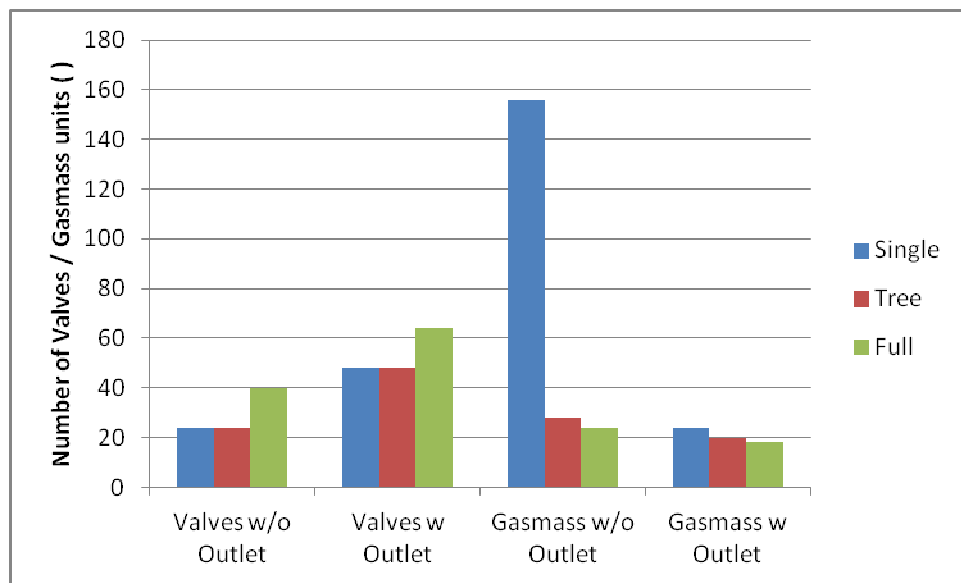


Figure 4-5: Required gas units and valves for each path design to achieve checkerboard pattern (with and without outlet valves at each cell)

As previously mentioned, the added mass and complexity of the additional valves in contrast with the mass reduction of the required inflation gas must be addressed for each mission separately. From a comparison of the values in Figure 4-5, it can be seen that

the extreme case to minimize the number of valves and complexity requires 24 valves and 156 gas units for the single tree without outlet valves. While minimizing gas use requires 64 valves and only 18 gas units for the fully connected tree with outlet valves on each cell. It should also be noted that these calculations assume that all valves and cells remain operational. In the case of the catastrophic failure of a cell or multiple cells, the damaged cells need to be isolated via the permanent closure of neighbouring valves. In this case, an architecture with increased valve connectivity has the added benefit of being able to isolate damaged cells and reroute gas flow in the case of failure.

The same analysis can be undertaken for the required electronic routing and the controller architecture and it also highly depends on the chosen application. The self-containing free flying colonies obtain their autonomous behaviour from their disaggregated control of each colony. While the size of satellites keeps on shrinking which will enable all functionality to be packaged into just a $10 \times 10 \times 10 \text{ cm}^3$ cube, the developed structure aims for target applications where a high area to mass ratio is required. Nevertheless, the miniaturization of the electronic hardware and the comparably low cost that the development of cube satellite electronics brought with itself opens up the possibility to further increase the area to mass ratio of the developed structure or even the whole satellite.

The flexibility of the system can be greatly increased by printing the circuit boards directly on a flexible substrate. This method is already used in multiple commercial electronic products like smart phones. In order to allow high packing efficiency during launch, subsystems such as computers, cameras, gyroscopes, accelerometer, etc. need to be miniaturized and distributed across the cells. The idea was to explode (disaggregate) a common cube satellite and place its components on the cells and make all the components communicate. The unique architecture of the inflatable structure opens the possibility of changing its shape to be adapted to various space mission stages or environmental conditions. By distributing the electronics over the surface of the inflatable smart structure, a very lightweight giant structure in space can be created without having the need for any rigid heavy substructures which would be dead weight.

These satellites with a high area to mass ratio would be a great way to ensure that the satellite will re-enter the Earth's atmosphere in the recommended 25 years to mitigate space debris.

4.2 Application I: Reflector & Concentrator

The first application discussed more in detail is the use of such a shape shifting structure as a concentrator. The shape changing reflector can alter its shape to adjust the beam width instantly to focus the energy on a specific point. The applications here are countless, not just for concentrating the sun's energy but also for radio frequency (telecommunication and broadband) applications. Nevertheless, the use of this structure as a sun concentrating system are discussed more in detail in the following through the initial motivation of this work to provide a means to collect large quantities of solar power.

4.2.1 Concept and System Design

The following subchapter shall give an overview on the general concept of the reflector application first as a sun concentrator for the Mirror Bees study [1] outlined in the introduction as an initiation of this work. In the Mirros Bees Study, an asteroid shall be redirected using solar sublimation. For this extensive amounts of energy are needed that can only be provided by nuclear power stations or large concentrators that focus the sun's energy. The second possible application that uses the same concept but instead is bringing the energy down to Earth is a Space Based Solar Power Satellite.

Mirror Bees – Asteroid Concentrator

A sun concentrator dish can be used to focus solar radiation on an asteroid directly in order to ablate the asteroid and therefore change its trajectory [2]. In this scenario, the dish must be capable of changing its focal point on the surface of the target and must

also account for the unusual shape and rotation of an asteroid, thus requiring an adaptive concentrator. During the mission, the concentrator changes its curvature in the out of plane direction in order to focus the sun's energy on the uneven surface of the asteroid.

Space Based Solar Power – GEO-Concentrator

By looking at the increase of energy consumption over the last decades, it becomes obvious that the energy sources here on Earth will be not enough to sustain the life standards that we are used to today. Especially when more developing countries become wealthier and therefore will increase their energy demands as well. A viable option would be the more efficient use of the sun as an abundant energy source. By changing the ground based to space based solar power plants the losses of energy through the atmosphere can be reduced to just fractions [7]. For space based solar power to become a viable alternative in terms of reduced costs, the structures in space must be larger than everything that has been launched into space up till now. For this reason the use of deployable structures becomes necessary to overcome the launcher payload restrictions of rockets available today.

In recent years, increasing interest has developed in space based solar power especially within the big space agencies ESA, NASA and JAXA as well as various academic institutions all over the world. In 2012 as part of the NASA's Innovative Advanced Concepts (NIAC) program, a team under the lead of John C. Mankins obtained funding to continue work on a modular solar power plant design called SPS-ALPHA [86]. The system shown in Figure 4-7 redirects the sun's energy via giant movable mirrors arranged in a bee hive kind of structure onto solar panels and then beams it to the ground via microwaves.

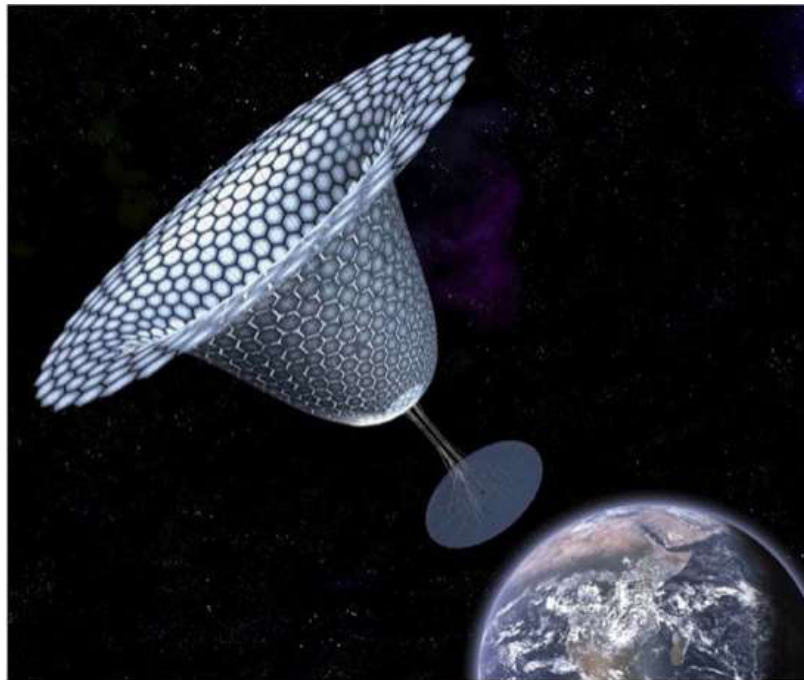


Figure 4-6: Artist Impression of SPS-ALPHA [86]

The proposed design of the space based power system has two distinct sections, one ground and one space based. Similar to SPS-ALPHA, concentrators will be used to redirect and focus the sun's energy on stationary solar panels (Figure 4-6). An important aspect of space based solar power is the safety of the system because the energy needs to be beamed down from space to ground in a reliable and safe fashion. For this reason only the use of a geostationary space platform with a distinct ground station location is viable.

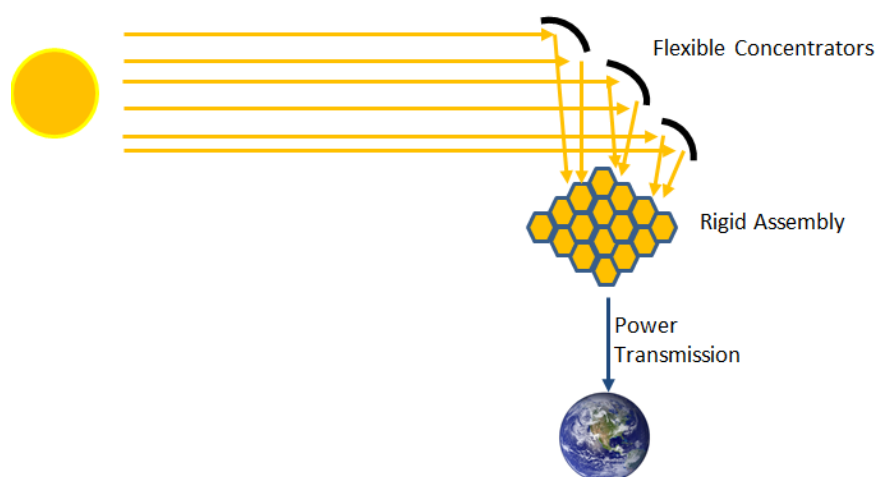


Figure 4-7: Schematic of functionality of space solar power space segment

As mentioned above, the orbital part of the SBSP station is based on a similar architecture to NIAC's SPS-ALPHA [86]. The design consists of mainly two components, the rigid solar panel/energy transmitter and a deployable concentrator that redirects the sun's energy on the solar panel [87].

Solar Panel/Power Transmission Assembly

The solar panel and power transmission assembly is made up of rigid hexagons which have a diameter of just less than five meters in order to stack a few of them in the launchers available today. The hexagon shells that can be seen in Figure 4-8 have a high efficiency solar panel on the top and a power transmission system on the bottom pointing towards the ground segment. The energy transmitting systems will use either laser or microwaves for power transmission to the ground. Power transmission via laser or microwaves have currently the same technology readiness level (TRL) but their application depends on the legal framework and safety concerns of using those technologies for power transmission through the atmosphere.

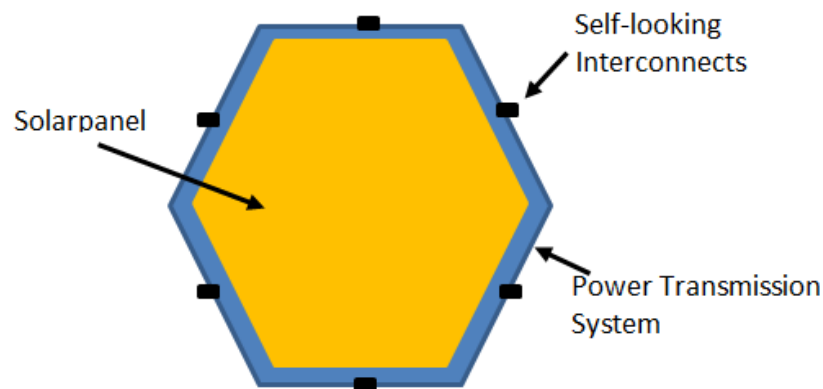


Figure 4-8: Schematic of rigid solar array / power transmission system

The rigid shells are assembled in space shortly after arriving at their destination in a geostationary orbit. Each hexagon has mechanical and electrical interconnects on each of its six sides with which each panel simply locks into place with its neighbour's. Over the interconnects, the panel shares health data with the other panels for transmission and

monitoring to the ground. It is envisioned to use assembly robots to build up the panels in orbit and perform maintenance tasks of exchanging broken panels in case of damage through space debris or micrometeoroids for example.

Deployable Concentrator

The deployable concentrator on the other hand has to be very large to redirect and concentrate the sun's energy on the stationary solar panel / power transmission assembly. The proposed design is a light weight flexible structure with low storage volume and high deployed volume which has the ability to change its global shape in space. The main concept of the proposed colony design is that a number of colonies, each composed of a number of individual cells, will be assembled together in space to form a global structure [88].

Each colony is either a two dimensional plane or a three dimensional cube made up of inflatable cells surrounding a central pressure source. The modular colonies as well as the cells are scalable to be adapted to a desired application ranging from nano scale to macro scale. The high pressure source is filled at the beginning of the mission and uses the gas stored in the pressure tank to inflate individual cells and change the overall shape of the structure until the tank is empty. The global structure is made up of a number of similar self-sustaining and self-controlling cellular colonies deployed from a payload fairing, which is only a small fraction of the volume of the deployed structure.

Each of the flexible dishes of the space based solar power plant can be either free flying (or formation flying) in a predefined distance to the solar panel assembly or it could be mounted on a very light substructure like it is proposed for SPS-ALPHA.

4.2.2 Simulation

In this subchapter, the simulation of the sun concentrator for the asteroid satellite as well as the GEO SBSP satellite are carried out. After the release of the satellite at its

dedicated orbit position, the structure will inflate itself to form the large deployable dish. To obtain the desired concentrator shape the cells in the structure need to be actuated. Different actuation pattern and their resulting shape are shown with the use of a PID controller to optimize the shape to focus the sun's energy. At the end, the code's capability to show the behaviour of the structure subjected to external forces and perturbation is shown for the asteroid satellite example.

Inflation

Figure 4-9b shows the qualitative displacement of the nodes of a 10x10x2 cell structure Figure 4-9a with an inflation time of 5 seconds. For this array of multiple cells, the sum of the forces at each node is formed creating an equal distribution and thereby modelling the inflation. It can be seen in b that the whole inflatable structure oscillates slightly after the inflation is complete. Each of the lines in this plot shows the displacement of each node in the structure over time.

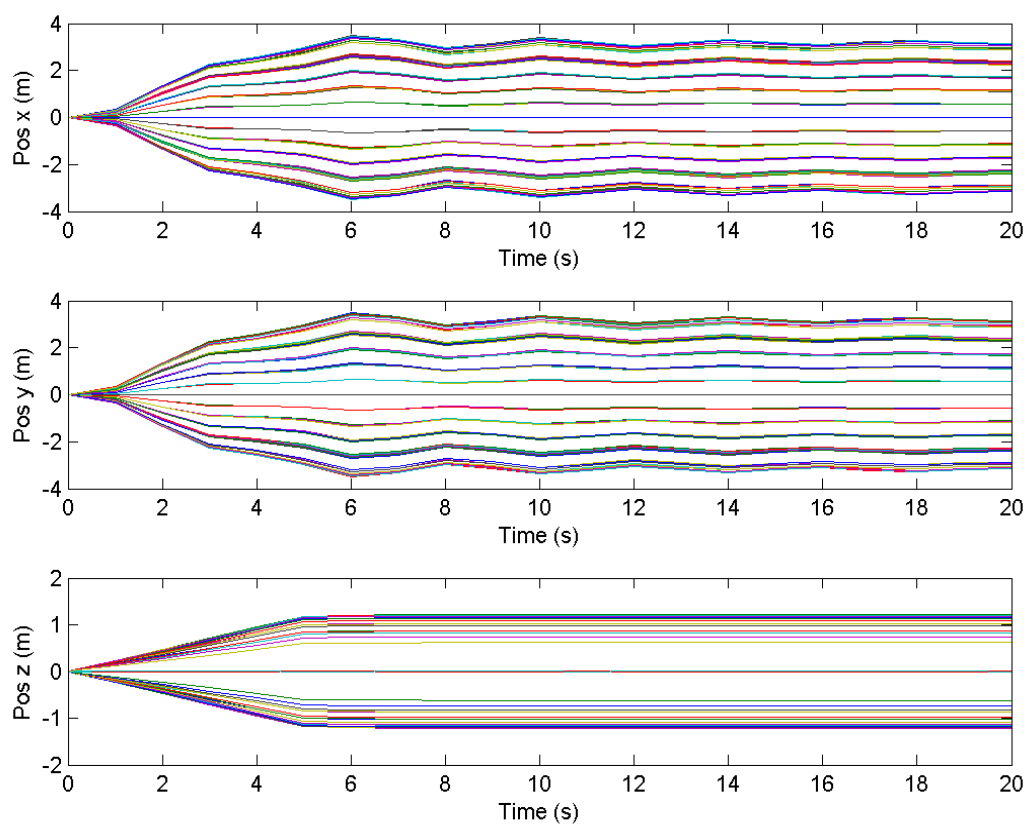
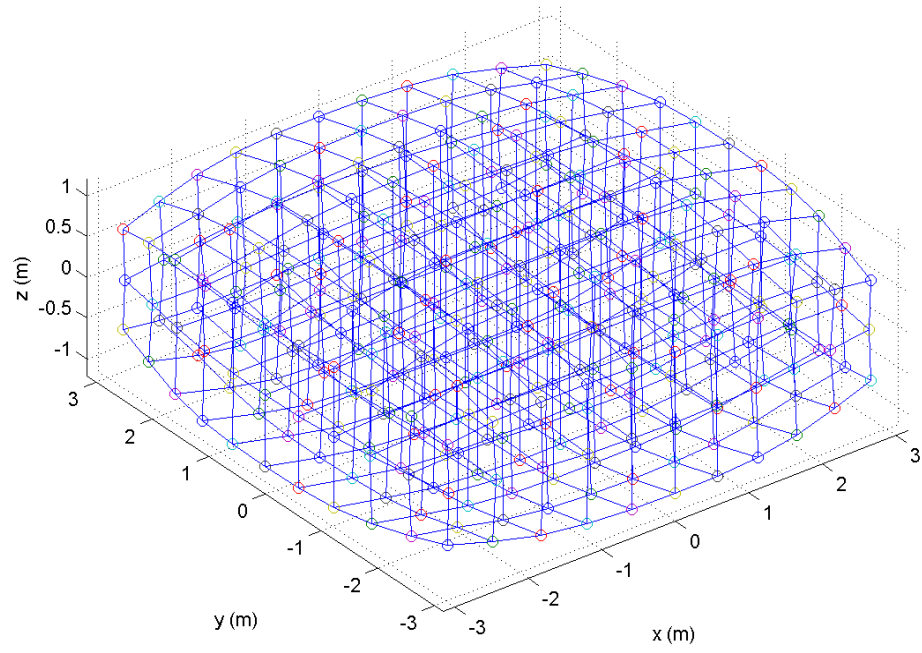


Figure 4-9: a) Inflated 10x10x2 cell array, b) Displacement of x-, y-, and z-positions

After inflation is complete, the differential pressure stays constant but it is also possible to apply a leakage to certain cells or the entire array of cells. In practice, this

leakage could be caused by micrometeoroid impacts, fabrication errors, degradation of materials, or natural leakage of an inflatable in the space environment.

Actuation

The inflated dish has to be capable of changing its focal point on the surface of the target. After the deployment through inflation has formed a flat sheet, the cells are actuated to form the curved concentrator dish. During this actuation process, air mass is transferred from the top cells to the bottom cells resulting in a positive curvature of the dish. Similar to the inflation, the forces on the cell corners change by the transferral of air mass. The sum of the internal forces will vary from cell node to cell node and therefore the whole structure will alter its shape. To change the focal point, the structure was actuated twice with the second actuation cycle having twice the air mass exchanged from the top to the bottom layer. Figure 4-10 shows the evolution of the deformation of cells from due to actuation. To increase the readability of the graphs, only the central section of the top layer of the full array from Figure 4-9 is displayed. Figure 4-10a shows the array before actuation, while Figure 4-10b shows the array after being actuated once, and Figure 4-10c shows the increased curvature of the structure after being actuated twice.

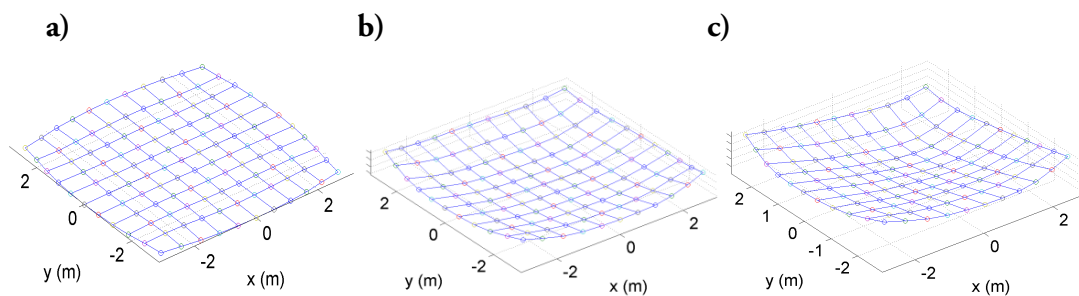


Figure 4-10: Central layer wireframe plot of a) inflated structure, b) structure actuated once and c) structure actuated twice

The position over time of all the nodes can be seen in Figure 4-11. In the first four seconds of the simulation the structure was inflated homogenously. After the oscillation was mostly settled, the first actuation was started at twenty seconds with a linear increase

for five seconds. The second actuation, also shown in Figure 4-11, was started at 40 seconds and also lasted for five seconds with a linear increase.

The displacement curves show clearly that most of the deformation of the structure occurs in the z-direction which was the desired response. The observed oscillation of the system is caused by the fast actuation time and the low damping nature of the structure.

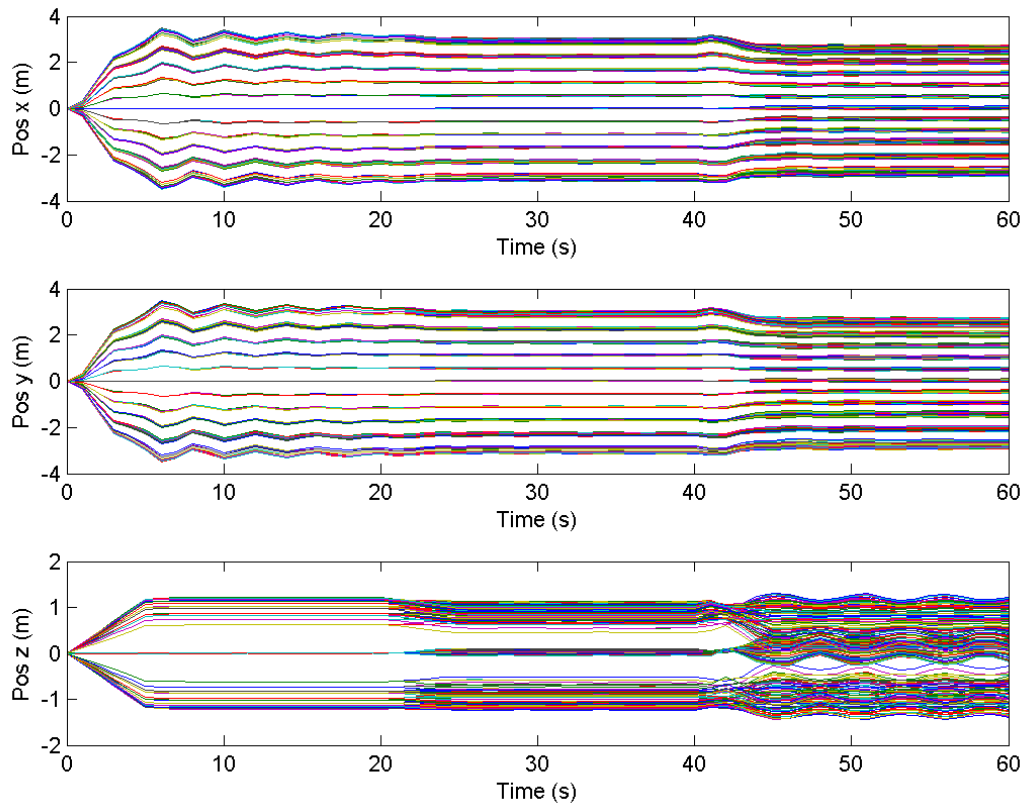


Figure 4-11: Displacement of nodes during inflation in all directions ($t < 5s$) and actuation ($t > 20s$)

The actuation that was leading to the displacement in Figure 4-10 and Figure 4-11 respectively was with an even distribution throughout the top and bottom cells. From Figure 4-11 it becomes obvious that by actuating the structure too fast and too strong, the whole system will start to oscillate. A slower actuation will lead to the smoother displacement profile as can be seen on page 75 of Chapter 3.3.3.

The deformation capabilities of the structure can be best seen by using different actuation patterns. The following simulation was carried out with a $13 \times 13 \times 2$ cell array instead of the smaller array used to demonstrate the inflation and actuation capabilities.

The increase of cell array size was mainly carried out to ensure that the actuation pattern is applied to the flat part of the array which forms in the centre in order to assess the results caused by the specific actuation pattern. The two patterns that were used here was firstly a cross like actuation pattern that can be seen in Figure 4-12a. This actuation pattern has the maximum actuation in the centre lines of the concentrator. The second chosen actuation pattern can be seen in Figure 4-12b which also has its maximum in the centre but decreases to the circumference cells in concentric circles.

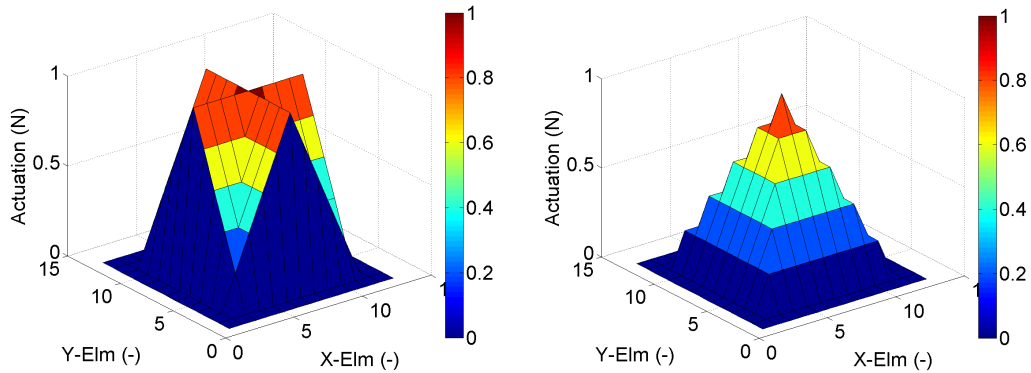


Figure 4-12: Actuation of cells for a) cross actuation and b) circle actuation

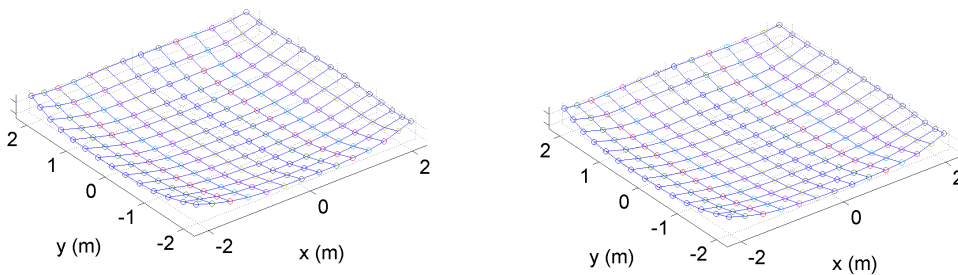


Figure 4-13: Shape change of array for a) cross actuation and b) circle actuation

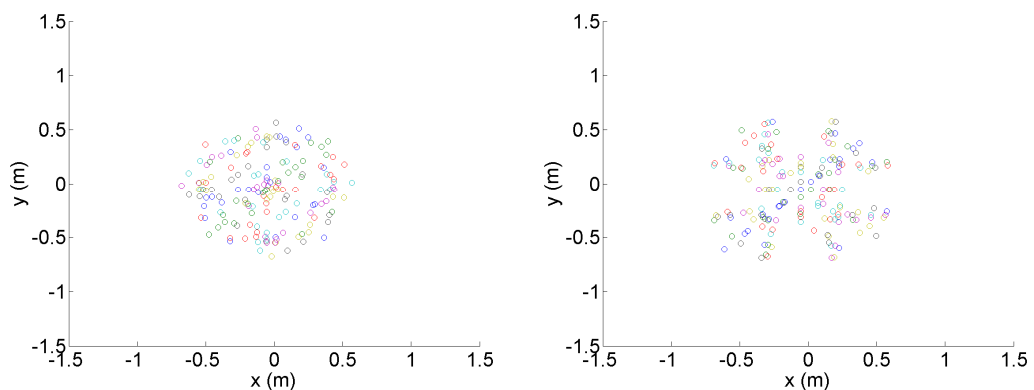


Figure 4-14: Focal area of array for a) cross actuation and b) circle actuation

Figure 4-13 and Figure 4-14 respectively show the results of the two folding patterns. In Figure 4-14 the minimum focal area for the cross actuation is at 4.6m and has a radius of $\sim 0.5\text{m}$ (Figure 4-14a), for circle actuation on the other hand, the minimum focal area is at 5.2m and has a radius of $\sim 0.7\text{m}$ (Figure 4-14b) . Each of the dots in the image represents the normal of one cell on the array projected to a focal plane in a certain distance. This chart gives an indication of the concentration capability of the concentrator. It can be seen that the cross actuation pattern has a slightly better performance than the circle actuation pattern.

In the next step the controller that was outlined in Chapter 3.4 was applied to the model to show the structure's capability to control the pressures in the cells of the reflector in a way that the shape can be optimized to focus all the energy in one point. As most of the reflectors and antennas that need to focus for example RF waves on a specific point, a parabolic reference shape is used.

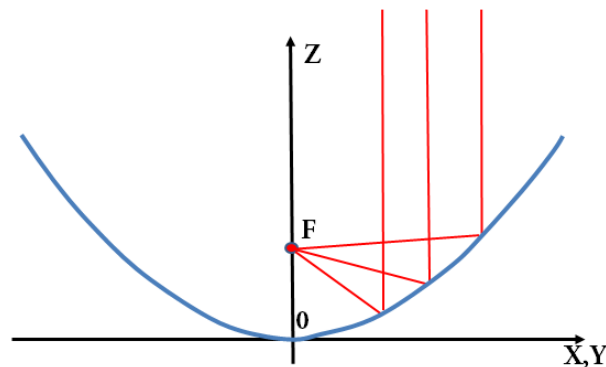


Figure 4-15: Path of rays in parabolic concentrator

Figure 4-15 shows the basic shape of the parabolic reflector as well as the path of the rays. For parabolic reflectors, the incoming rays are parallel to the reflector z-axis. Once reflected on the surface of the reflector, the rays cross their path at the focal point F (the focal length f is the distance between the base of the reflector 0 and the focal point F). To show the shape adaption capabilities of the structure, an axi-symmetric reflector was chosen as a baseline. The equation below was used to calculate the required z coordinate for each cell based on its x and y coordinates and as well as the focal point of the parabolic reflector f .

$$z = \frac{(x^2 + y^2)}{4f} \quad \text{Eq. 4-1}$$

In the simulation a 9x9x2 cell array baseline was used forming a reflector dish with a diameter of roughly 3m. It is common to specify the reflector in regards to its diameter with the focal length-to-diameter ratio F/D. To show the applicability of the control algorithm to different reflector shapes a focal length of 1.5m and 2m was simulated leading to a F/D of 0.5 and 0.66.

Using Equation 4-1, the necessary z displacement of all cells can be calculated and compared to the existing displacement.

F/D=0.66:

x/y	1	2	3	4	5	6	7	8	9
1	-60.0%	-46.3%	-34.6%	-23.0%	-17.2%	-20.1%	-30.2%	-42.2%	-53.3%
2	-46.2%	-27.8%	-14.4%	-2.1%	4.0%	1.0%	-9.6%	-23.1%	-38.7%
3	-34.6%	-14.4%	0.3%	13.4%	19.8%	16.6%	5.4%	-9.3%	-26.8%
4	-23.0%	-2.1%	13.4%	26.9%	33.5%	30.2%	18.6%	3.2%	-15.1%
5	-17.2%	4.0%	19.8%	33.5%	40.0%	36.8%	25.0%	9.3%	-9.2%
6	-20.1%	1.0%	16.6%	30.2%	36.8%	33.5%	21.8%	6.2%	-12.1%
7	-30.2%	-9.6%	5.4%	18.6%	25.0%	21.8%	10.4%	-4.7%	-22.5%
8	-42.1%	-23.1%	-9.3%	3.2%	9.3%	6.2%	-4.7%	-18.8%	-35.3%
9	-53.3%	-38.7%	-26.8%	-15.1%	-9.2%	-12.2%	-22.5%	-35.3%	-49.6%

FD=0.5:

x/y	1	2	3	4	5	6	7	8	9
1	-61.1%	-45.3%	-33.0%	-22.8%	-18.0%	-20.4%	-29.0%	-40.7%	-53.8%
2	-45.3%	-25.2%	-11.0%	-0.1%	4.9%	2.5%	-6.6%	-19.9%	-37.2%
3	-33.0%	-11.0%	4.4%	16.1%	21.3%	18.7%	9.1%	-5.3%	-24.6%
4	-22.8%	-0.1%	16.1%	28.1%	33.5%	30.8%	20.8%	5.8%	-14.2%
5	-18.0%	4.9%	21.3%	33.5%	38.9%	36.2%	26.1%	10.8%	-9.4%
6	-20.3%	2.5%	18.8%	30.8%	36.2%	33.5%	23.4%	8.3%	-11.8%
7	-29.0%	-6.6%	9.1%	20.8%	26.1%	23.4%	13.6%	-1.2%	-20.7%
8	-40.7%	-19.9%	-5.3%	5.8%	10.8%	8.3%	-1.2%	-15.0%	-33.3%
9	-53.8%	-37.2%	-24.6%	-14.3%	-9.4%	-11.8%	-20.7%	-33.3%	-49.2%

Figure 4-16: z-position error of 81 cells before shape control (top F/D=0.66, bottom F/D=0.5)

Figure 4-16 shows the normalized difference in percentage of the existing to the desired z-position of all the 81 cells for the two cases. 100% is the maximum (+40% at the 5x5 cell in the centre) minus the minimum error (-60% at the 1x1 cell in the top left corner). Similar to the spherical example case in Chapter 3.4, in the code the x and y

position of all the cells are continuously calculated and the difference of the existing position to the desired position is the error for the PID controller. The PID controller was converged with the parameters set to $K_p = 0.5$ (proportional gain), $K_d = 0.1$ (derivative gain) and $K_i = 0.5$ (integral gain). Figure 4-16 shows the resulting z-position error in meters for the $F/D = 0.66$ case of the 81 cells after 100 control cycles.

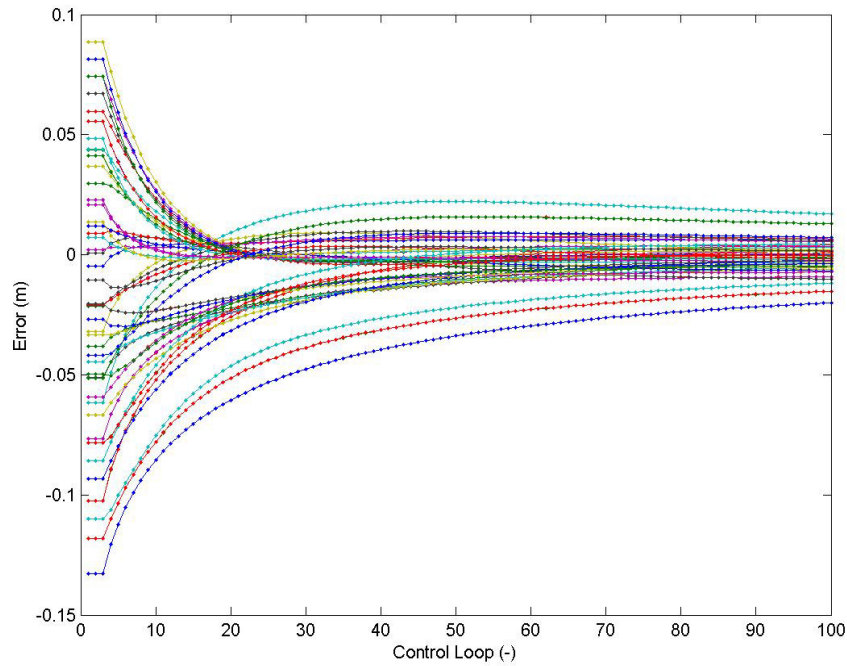


Figure 4-17: Development of error over 100 control loops ($F/D = 0.66$)

It can be seen in Figure 4-16 that most of the errors are approaching zero. Similarly to the error at the beginning of the simulation shown in Figure 4-16, the error at the end of the simulation can be seen in Figure 4-18 as percentage of the total z-position error from the perfect sphere at the beginning of the simulation.

$F/D = 0.66$:

x/y	1	2	3	4	5	6	7	8	9
1	-9.0%	1.8%	-4.1%	-2.2%	-1.6%	-2.4%	-2.7%	-1.1%	-6.9%
2	1.8%	7.7%	0.6%	2.8%	3.0%	2.4%	2.7%	5.8%	2.0%
3	-4.2%	0.6%	-4.5%	-1.6%	-1.6%	-2.4%	-3.0%	-0.8%	-3.3%
4	-2.2%	2.8%	-1.6%	0.8%	0.7%	0.1%	-0.4%	1.4%	-1.5%
5	-1.7%	3.0%	-1.6%	0.7%	0.6%	0.0%	-0.2%	1.6%	-1.0%
6	-2.4%	2.4%	-2.4%	0.1%	0.0%	-0.5%	-0.8%	0.9%	-1.7%
7	-2.7%	2.6%	-3.0%	-0.4%	-0.2%	-0.8%	-1.2%	0.7%	-2.1%
8	-1.1%	5.8%	-0.8%	1.4%	1.6%	0.9%	0.7%	3.3%	0.3%
9	-6.9%	2.0%	-3.3%	-1.5%	-1.0%	-1.7%	-2.1%	0.3%	-5.4%

F/D = 0.5:

x/y	1	2	3	4	5	6	7	8	9
1	-13.5%	1.2%	-4.5%	-2.8%	-2.2%	-3.0%	-3.3%	-1.9%	-10.1%
2	1.3%	8.5%	0.9%	2.8%	3.2%	2.5%	2.8%	6.4%	1.6%
3	-4.5%	0.9%	-4.3%	-1.7%	-1.4%	-2.4%	-2.9%	-0.5%	-3.6%
4	-2.9%	2.8%	-1.7%	0.5%	0.6%	-0.1%	-0.5%	1.3%	-2.1%
5	-2.2%	3.2%	-1.4%	0.6%	0.6%	0.0%	-0.2%	1.6%	-1.6%
6	-3.0%	2.5%	-2.4%	-0.1%	0.0%	-0.6%	-0.9%	0.9%	-2.2%
7	-3.3%	2.8%	-2.9%	-0.5%	-0.2%	-0.9%	-1.2%	0.8%	-2.6%
8	-1.9%	6.3%	-0.5%	1.3%	1.6%	0.9%	0.8%	3.4%	-0.2%
9	-10.1%	1.6%	-3.6%	-2.1%	-1.5%	-2.2%	-2.6%	-0.2%	-7.5%

Figure 4-18: z-position error of 81 cells after shape control (top F/D = 0.66, bottom F/D = 0.5)

Through the PID controller it was possible to greatly decrease the error especially in the centre of the parabolic reflector for both cases. There is still an error of 6-10% for the F/D = 0.66 case and 7-14% error for the F/D = 0.5 case but these few elements (4-8 out of 81) only have a minor effect on the overall performance.

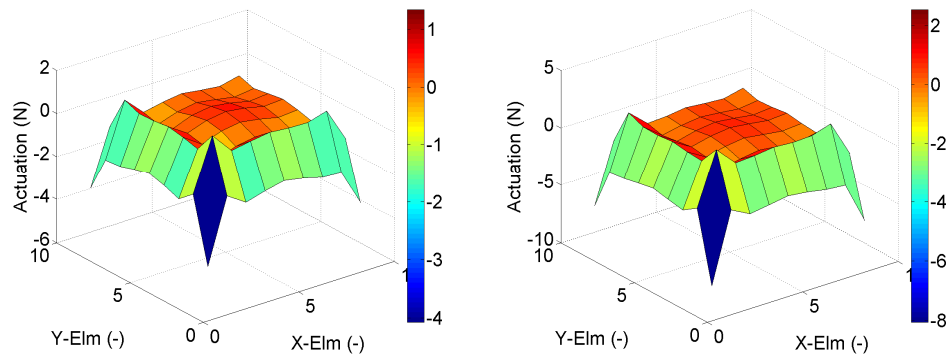


Figure 4-19: Actuation of cells for at the end of control cycle (left F/D = 0.66, right: F/D = 0.5)

The actuation of the top cell layer is shown in Figure 4-19 after the 100 control cycles. This actuation force is applied at the end of the inflation leading to a concentration of the reflective rays in the focal point with a radius of just 0.1m for the F/D = 0.66 case and a radius of for 0.2m the F/D = 0.5 case. This concentration is displayed in Figure 4-20.

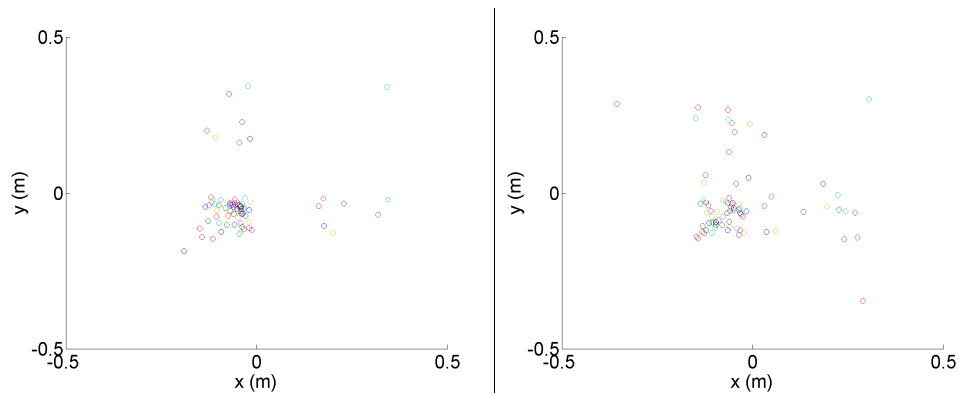


Figure 4-20: Position of all cell normals at the focal point (left: F/D = 0.66, right: F/D = 0.5)

With the results obtained by the PID controller after just 100 cycles, the focal area of the concentrator could be significantly decreased by an order of magnitude. The code also showed its capability to be adapted quickly to changing parameters.

Effect of External Forces (Asteroid Case)

The initial idea for this work came from the Mirror Bee project where large reflectors were needed to focus the sun's energy to sublimate the surface of an asteroid in order to deflect it. In this chapter, the GEO reflector design for the space based solar power application above is taken on as a solar concentrator to focus the sun's energy to provide power for the sublimation laser. The chapter above already showed that the developed structure is capable of deploying as well as optimizing its shape to focus the sun's energy on a specific point (focal point). For the Mirror Bee application (see Figure 2-2), the sun concentrator is mounted on a satellite that is flying over the surface of an asteroid.

As an example application for the deflection satellite mission, the Near Earth Object (NEO) 99942 Apophis was chosen. This asteroid will come close to Earth in 2029 and 2036. 99942 Apophis has an estimated mass of 4×10^{10} kg and an diameter of 325m (+/- 15m) [89].

Figure 4-21 shows a sketch of the satellite with the curved adaptable concentrator flying into the shadow of the asteroid. The asteroid as well as the satellite has an own inertial Cartesian coordinate system, X_{ast} , Y_{ast} and Z_{ast} for the asteroid and X_{sat} , Y_{sat} and

Z_{sat} for the spacecraft. The satellite is initially flying on a course along the satellite axis X_{sat} .

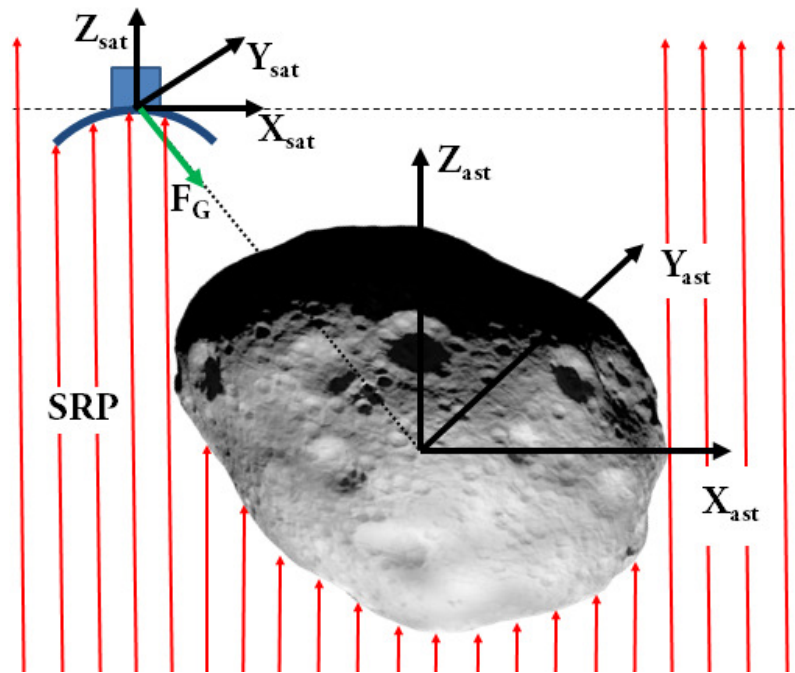


Figure 4-21: Sketch with external forces of satellite passing asteroid

The two external forces acting on the satellite, are firstly from the gravitational field of the asteroid and secondly from the solar radiation pressure originating from the sun. The gravitational force is calculated with the differential gravity equation (Equation 3-43) outlined in Chapter 3.3.3 with the mass of 99942 Apophis. The differential gravity acts on the entire structure; therefore it is applied to every node with its distance to the centre of mass.

The sun is located in the negative z-axis of the asteroid; the location of the asteroid towards the sun is not changing during the simulation. In order to observe an effect of the solar radiation pressure, total reflectivity of the structure as well as high solar activity and close approximation to the sun was assumed. With this an assumptions, a value of $200 \mu\text{N}/\text{m}^2$ of solar radiation force was used. The solar radiation pressure is only applied to the surface that it directly subjected to it; therefore it is only applied to the nodes in the sun facing surface of the satellite.

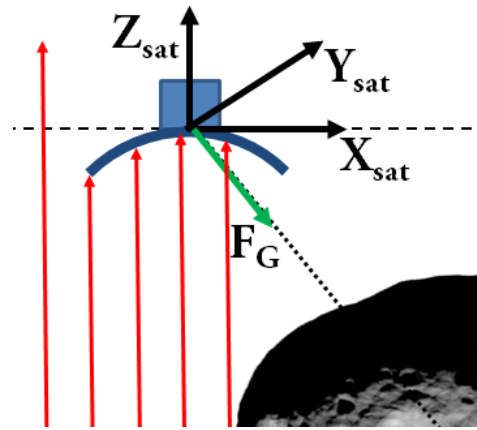


Figure 4-22: Satellite flying into the shadow of the asteroid

Figure 4-22 shows the time step as the satellite is flying into the shadow of the asteroid. In the shadow of the asteroid, the only external force acting on the satellite is the gravitational force from the asteroid. As the satellite moves into the shadow, its large concentrator will be partially in the shadow and partially in the sunlight as the right edge moves in the shadow first. It is expected that this introduces a positive torque around the y-axis (normal to the image plane in Figure 4-22).

As a concentrator baseline, a 10x10x1 cell structure was used. Each of the cells was inflated in the beginning of the simulation to a cell radius of $r_{cell} = 15\text{cm}$ leading to a concentrator of 3m x 3m and a total area of 9m². To initiate the simulation, the spacecraft was placed 10m above the surface (at closest encounter) and 200m before the asteroid. The initial velocity of the structure was set to $v=0.1\text{m/s}$ along the spacecraft x-axis. With this velocity, the spacecraft will be subjected to 400 seconds of solar radiation pressure before flying gradually into the shadow of the asteroid. It will take a total of 30 seconds until the full spacecraft is in the shadow of the asteroid. The simulation was carried out throughout the spacecrafts passage through the shadow of the asteroid until it emerged from the shadow. With this step, the effects of the gradual change of forces on the surface can be observed twice. Figure 4-23 shows the position and Figure 4-24 the velocity of the spacecraft in the asteroid coordinate system.

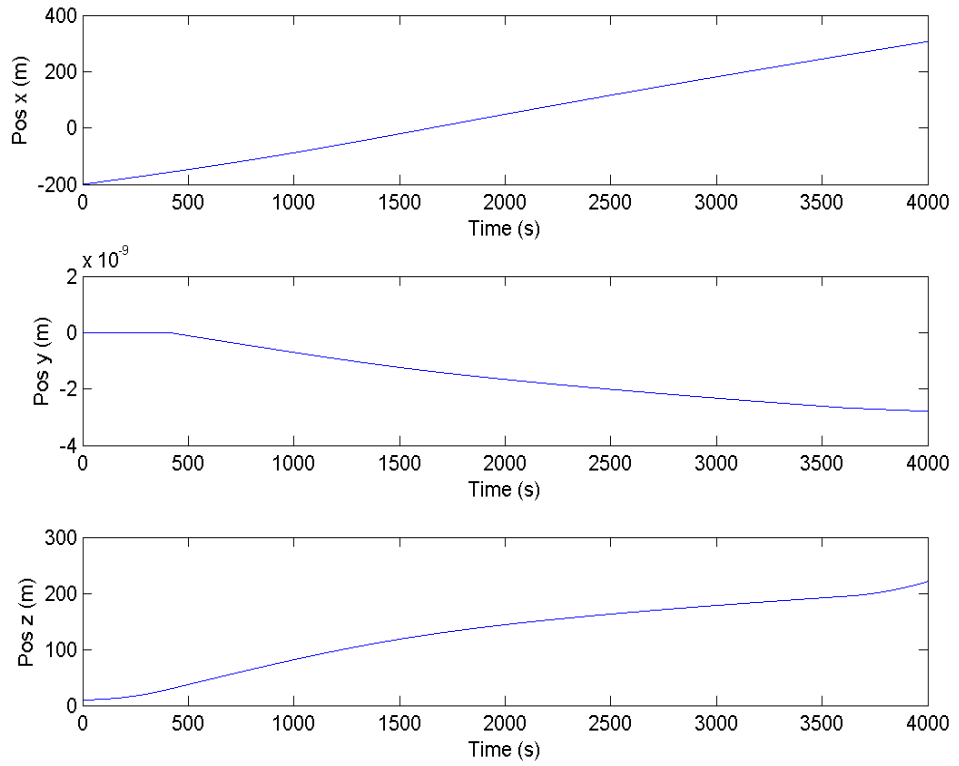


Figure 4-23: Mean position of the spacecraft over time (asteroid CS)

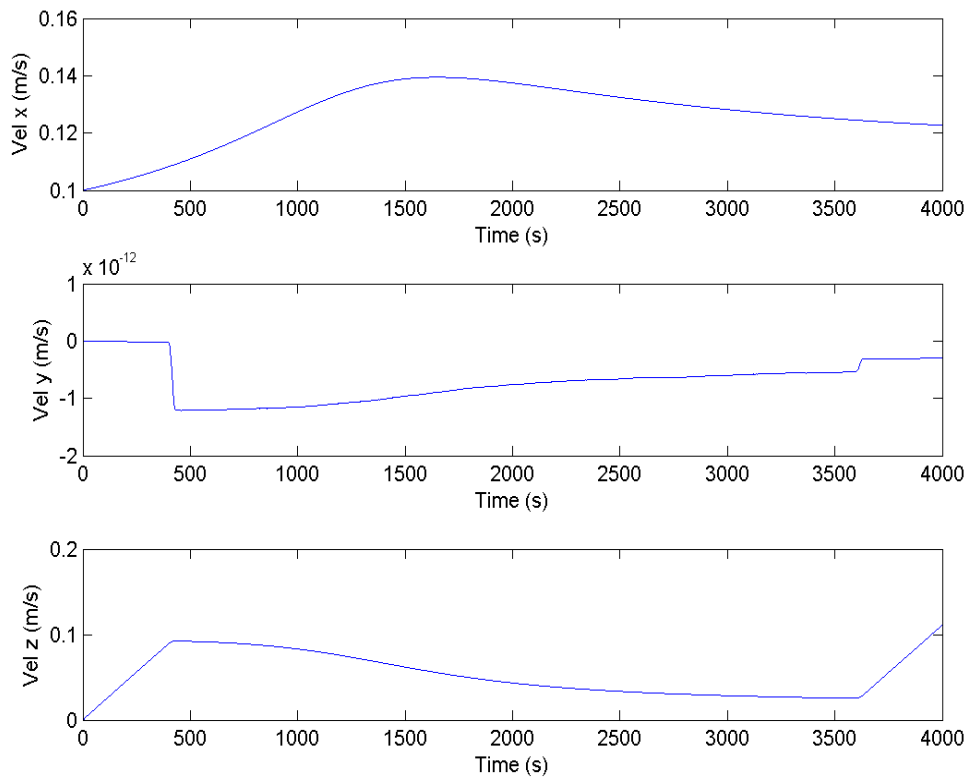


Figure 4-24: Mean velocity of the spacecraft over time (asteroid CS)

The x and z-axis plot in Figure 4-23 and Figure 4-24 shows that from the initiation of the simulation the spacecraft is propelled by the solar radiation pressure linearly in the positive z-direction and the initial velocity in the positive x direction. At around 400 seconds, the spacecraft moves inside the shadow of the asteroid and the gravitation force of the asteroid is the only external force acting on the spacecraft. The position slope of the z position and the velocity in x direction after 400 seconds indicates that the gravitational force is almost compensating for the momentum and displacement caused by the solar radiation pressure. At around 3500-3700 seconds, the spacecraft moves out of the shadow and the solar radiation becomes the dominant force again.

Looking at the spacecraft inertial coordinate system, Figure 4-25 shows the relative position of all the nodes of the deployed concentrator dish over the simulation time.

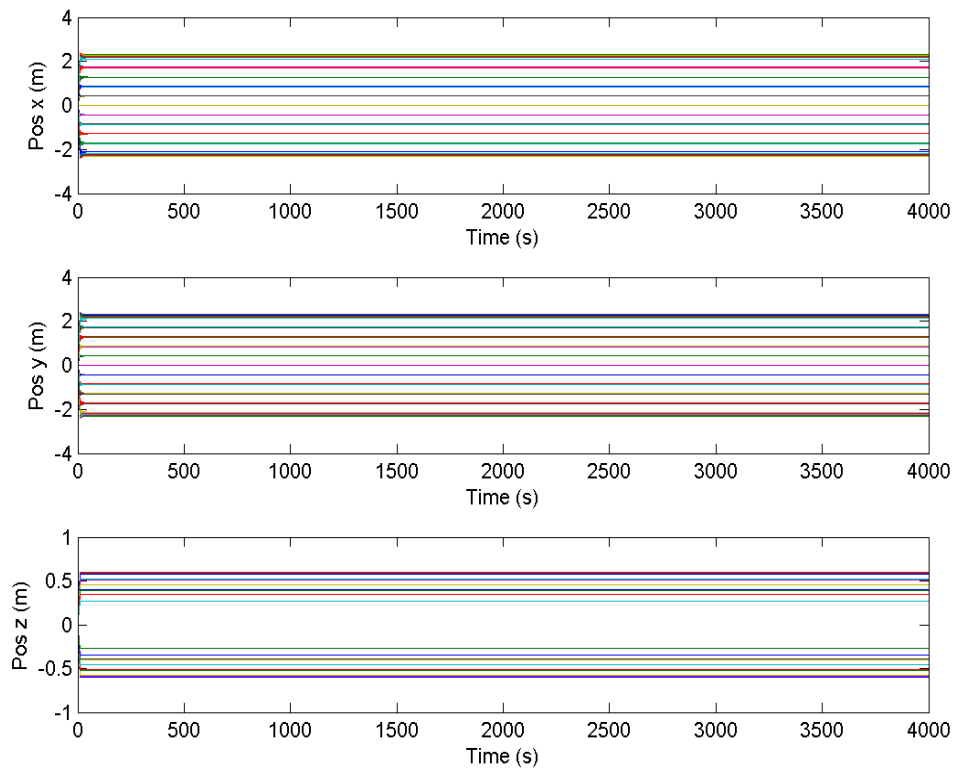


Figure 4-25: Position of spacecraft nodes (S/C CS)

From Figure 4-25 no large changes can be observed, therefore Figure 4-26 and Figure 4-27 only show the relative node displacement from the ideal state at the time the spacecraft moves in and out the asteroid's shadow.

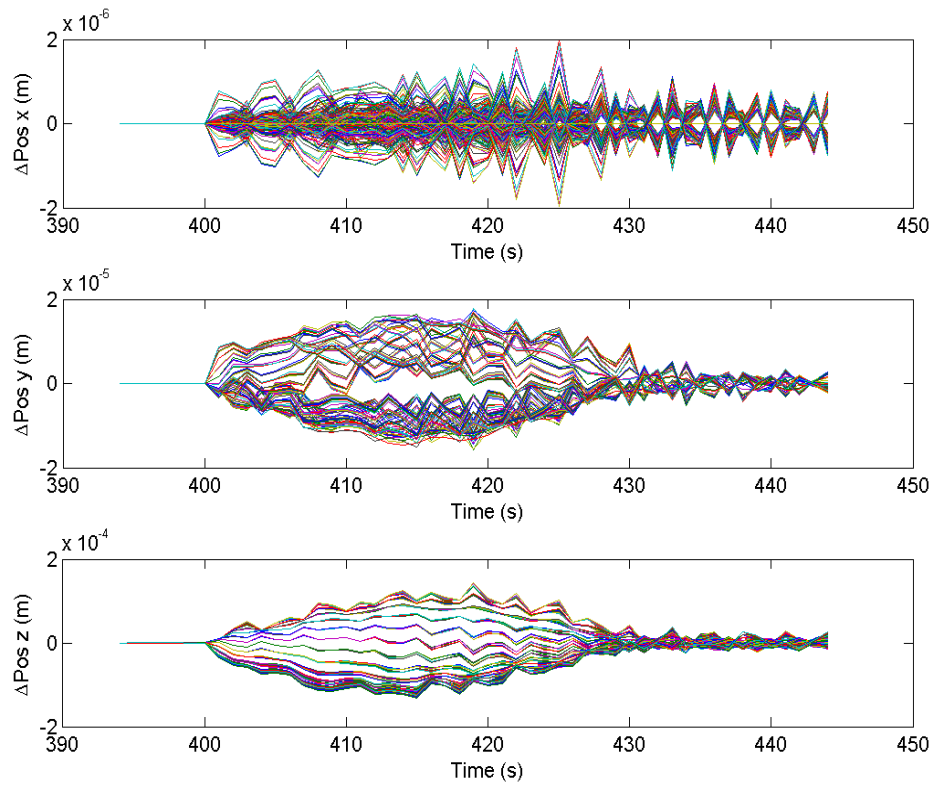


Figure 4-26: Rel. position change at entering shadow (S/C CS)

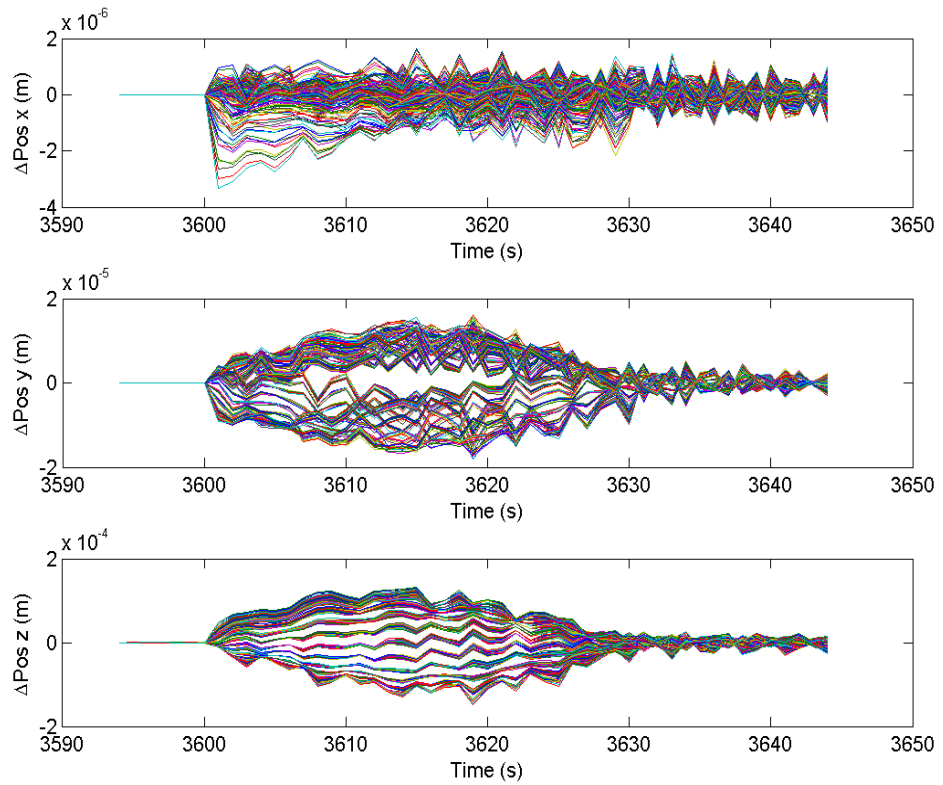


Figure 4-27: Rel. position change at leaving shadow (S/C CS)

Especially from the z-axis plot in the Figure 4-26 and Figure 4-27 the effects of the gradual passage of the concentrator into and out of the shadow can be observed. As Figure 4-26 and Figure 4-27 show the displacement of all nodes of the deployed structure from the ideal state, the shapes that all the nodes forming are an indication of the orientation of the whole structure. The shape in the z-axis plot shows a maximum thickness at around 415 seconds and 3615 seconds when half of the concentrator is in the shadow and the other half is in the light.

This subchapter showed that the code is capable to simulate the deployment and optimizing shape adaption for a reflector or concentrator. Furthermore, the effects of external influences like gravitational forces or solar radiation pressure are featured as well. To improve the simulation and the understanding of these deployable structures, experiments were carried out. First, StrathSat-R had the purpose to proof that its possible to deploy inflatable structures by using residual air inflation, while the iSEDE experiment took it a step further in trying to validate the concept of an all inflatable shape changing structure with disaggregated electronics. In the following the experiment StrathSat-R with its deployable concentrator like structure is described more in detail.

4.2.3 Experiment: StrathSat-R

An important aspect for validating this concept and to obtain material properties for the simulation of very large structures was the deployment of a structure in a micro gravity environment without any perturbing effects from gravity due to the very flexible and lightweight nature of the developed concept. To validate the concept of a structure deployed in space using inflation, a technology demonstrator mission was created and launched on a sounding rocket. The StrathSat-R [90], [42], [91], [92] experiment from the University of Strathclyde had the purpose to investigate the deployment behaviour using trapped air in a milligravity environment. A detailed description including experiment design, launch campaign summary and result evaluation of the StrathSat-R experiment can be found [41]. The experiment was

launched in May 2013 on board REXUS13 and in May 2014 on board the sounding rocket REXUS15 from the Swedish space range ESRANGE. Due to a procedural error during the REXUS13 launch campaign the free flying units were not ejected and therefore the mission objectives couldn't be achieved. The REXUS/BEXUS organisers therefore offered StrathSat-R a reflight on board REXUS15 a year later.

The experiment was deploying two different shaped inflatable structures from ejected free flying cube satellites. The first cube was deploying a pyramid shaped structure with inflatable booms giving shape to the Mylar covered pyramid. The use of a structure like this can be envisioned for a de-orbit device increasing the area of the cube satellite to decrease the orbital lifetime. The other cube satellite, named Self-inflating Adaptive Membrane (SAM) was deploying a technology demonstrator for the bio inspired concept presented in this thesis. The deployable structure itself consists of two layers two layers of spherical cells that are deployed by using the expansion of trapped air in the spheres when subjected to vacuum (space) conditions. The inflatable occupied forty percent of the cube satellite's structure, which led to a membrane diameter of 72.5cm once deployed with a packing efficiency of thirty percent. Over the two REXUS missions the design and fabrication of the inflatable structure improved which lead to two different deployable structures which are described in more detail below.

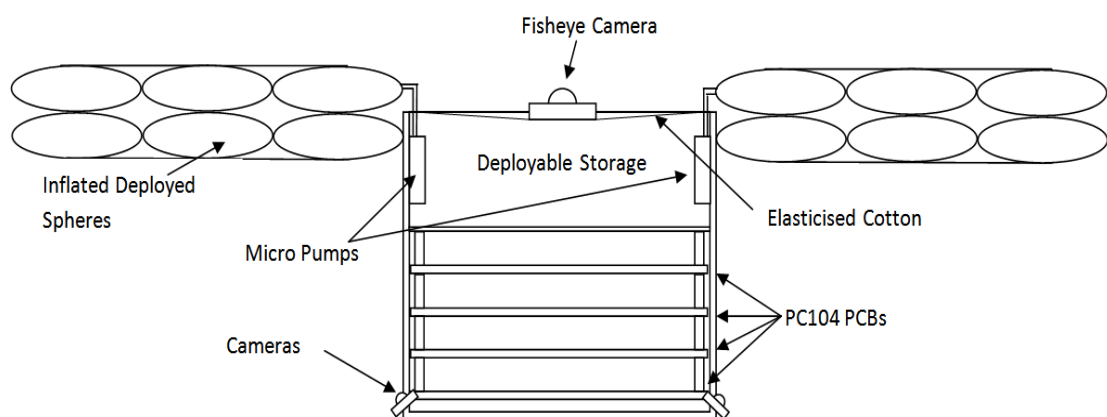


Figure 4-28: Cut-through schematic of StrathSat-R deployable SAM

The experiment had two main stages, the deployment phase and the adaptive phase. After ejection from the rocket, the reduced pressure of near vacuum conditions passively started the deployment and inflation of the structure from the storage configuration.

During the deployment and adaptive phase, images from cameras on the cube satellite and the rocket captured images from the dynamics of the membrane.

The shape changing structure is made of spherical cells that are inflated using residual air inflation which is described in the chapter above. The initial spheres are fabricated with similar volume and internal pressure. By changing the pressure between cells, the volume of one of them increases, the other decreases. With this local volume change, the shape of the global structure will change. A single actuator unit consists of two rows of inflatable spheres with a micro pump in between them to establish a pressure difference.

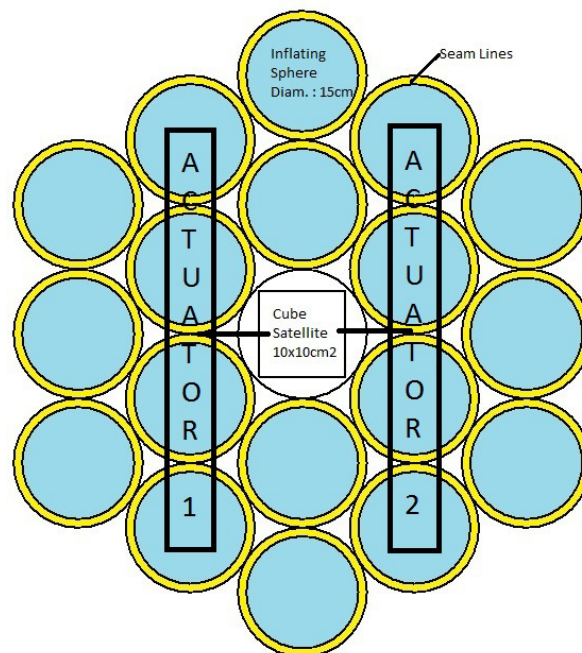


Figure 4-29: Actuator placement of Self-inflating Adaptive Membrane

There were two pumps mounted to the inside wall of the deployment storage (Figure 4-28). The rows of spheres closest to the sides of the cube are joined to form one big actuator as can be seen in Figure 4-29. The micro pumps will pump the residual air from the top to the bottom layer of Actuator 1 to lift up the left side in the figure, and from the top to the bottom layer of Actuator 2 to lift up the right side of the membrane.

Membrane and Cell Design

Over the course of the experiment development period from June 2011 until the successful launch in May 2014, the membrane design undertook an evolution in regards to deployment reliability and fabrication quality.

An important aspect to increase the maturity and viability of the concept was the investigation of possible cell fabrication techniques. Due to the wide range of applications and the possible sizes, only a couple of cell types could be manufactured and tested.

An inflated array of 5x2x1 (x,y,z direction) cells can be seen in Figure 4-30. The cells are ellipsoid cells with an uninflated length of 20 cm (z direction) and a width of 15 cm (x direction) per cell. The material used was 12 μ m thick Mylar that was joined on its circumference by a 3mm thick adhesive tape.



Figure 4-30: Prototype of 5x2cell inflatable smart structure

The first cell fabrication materials that were considered were polyamide films like PET, Mylar or Kapton. The big advantage of these materials is their availability for very thin sheets of thicknesses down to a few micro meters and their low weight but high in plane stiffness. The high in-plane stiffness is advantageous for providing a semi rigid inflated cell but disadvantageous for increasing the volume further once the cell is inflated. This is due to the high tensile stiffness of the material, keeping the cell surface area constant. Heat welding of the material, self-adhesive material and additional adhesive layer have all been considered as fabrication techniques.

Another option to fabricate these inflatable cells is the usage of hyperelastic material like latex or silicon rubber which is capable of expanding its surface area due to internal pressure change. The principle of heliotropism makes use of a volumetric increase and decrease of certain cells, enabling an overall structure to change its global shape. In order to mimic this behaviour and achieve an increase or decrease in volume, a cell requires a membrane material that is highly flexible and elastic so that small differential cell pressure changes result in a significant increase in volume. Additionally, this will allow sufficient differential pressure within an inflated cell to self-deflate when exposed to the vacuum of space. Although the requirements for elasticity and flexibility of the cell membrane are crucial, it is also important that the selected material can be incorporated with all other components into the overall design of the cell. For this reason, a silicone based polymer material has been selected as the cell material, which can be spun into thin sheets, cured, and then bonded at the cell borders.

The silicone rubber used for the bench test models is capable of elongating up to 900% of its original length before breaking and is useful at a temperature range of -53°C to 232°C , making it suitable for the manufacture of inflatable structures for space applications [93]. Nevertheless, further research has to be carried out into the materials property alteration due to UV radiation or atomic oxygen degradation occurring in the space environment.

The tools used for the mould of the inflatable cells were designed specifically for this purpose and manufactured using a 3D printer. It was found that the best way of manufacturing was in two parts; a top structure involving the cavity for the air to travel through and a base layer of thin silicone rubber that could then be adhered to make an enclosed assembly [94].

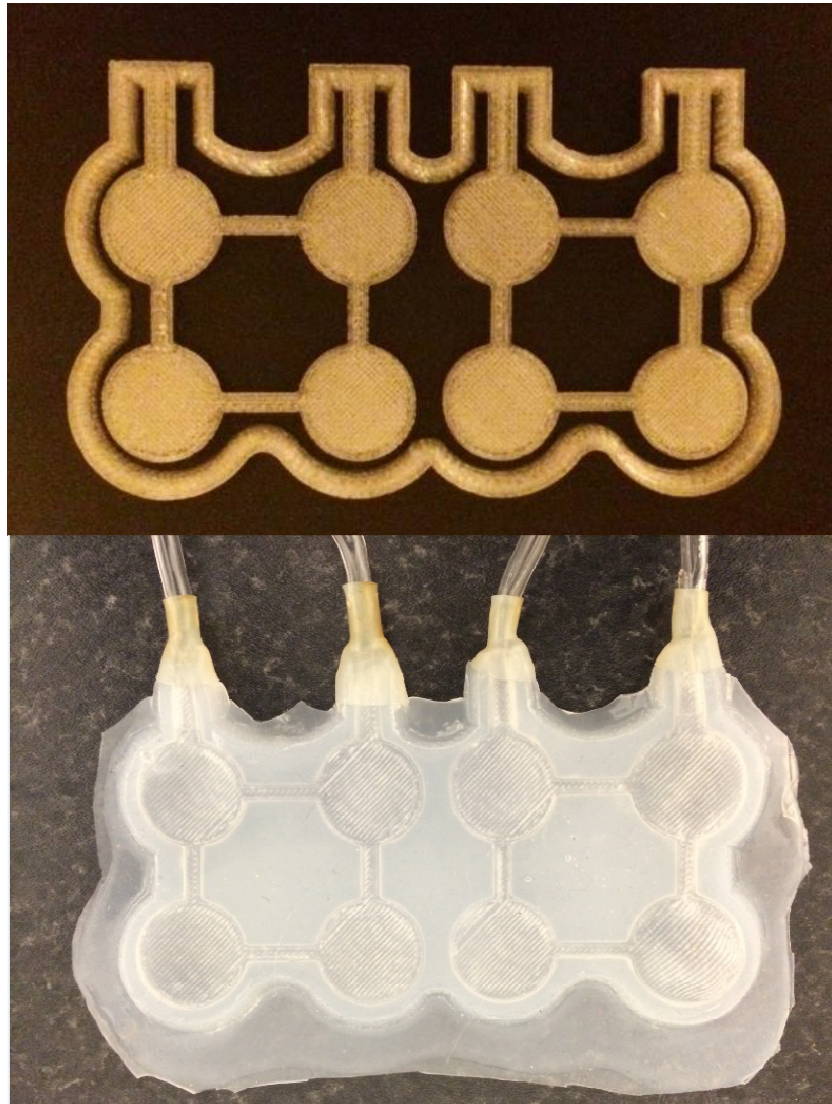


Figure 4-31: 3D printed mould (top) used to cast 4x2x1 cell structures (bottom)

The two layers were adhered using another layer of liquid silicone rubber mixture and allowing it to cure in order to seal the layers together. Several types of tools were tested in order to manufacture working prototypes of the inflatable cells. However it was found that moulds such as the one shown in Figure 4-31 (top) delivered consistent

results (see bottom) and was the most straightforward to use. It would be desirable to decrease the thickness of the cell walls in order to reduce the quantity of silicone used by adapting the mould but this causes difficulties in the fabrication process, often resulting in the silicone rubber being ripped on removal from the mould. If this problem was to be solved, it would improve the inflation of the cells and make the structure more lightweight and compact.

The inflation of the cells was undertaken with syringes to control the amount of air within each cell. The inflation of two adjacent cells can be seen in Figure 4-32.



Figure 4-32: Two fully inflated hyperelastic cells

The quality of the inflated shape highly depends on the fabrication method. Issues might arise due to air leaks between the air inlet and silicone cells. Additionally, the limited volume of air that could be input may not reach their full level of inflation yet an increased diameter of 200-300% can be observed. One of the manufacturing limitations is the even spreading of silicon rubber in the moulds causing variation in the thickness of the cell walls and resulting in uneven inflation of cells (as can be seen in Figure 4-33).



Figure 4-33: Inflated 4x2x1 cell array

The two designs that are discussed further here are the two designs that flew on the respective sounding rocket missions REXUS13 and REXUS15. Both designs have two layers of 18 inflatable cells oriented in a hexagon around the central cube satellite. The cells were manufactured by taking a $12 \mu\text{m}$ Mylar sheet and adding adhesive tapes around the circumference of all 18 cells simultaneously before adding the second layer of Mylar sheet to seal all the cells at the same time. The already flown structure can be seen to the right in Figure 4-34.

The deployable for the May 2014 REXUS15 mission on the contrary was built with the same $7.5 \mu\text{m}$ Kapton material that is used in DLR's Gossamer project [95] that will deploy a series of solar sail technology demonstrators between 2013 and 2015. The geometry of the cells was changed from a circular outline to a hexagon to increase manufacturability and quality of the structure. The hexagon structure before its flight can be seen in Figure 4-34 to the right. The hexagon structure fabrication also changed in regards to the REXUS13 structure by having a base layer of Kapton foil on which every hexagon was sealed with adhesive tape and an added layer of Kapton tape (yellow lines in Figure 4-34 left).

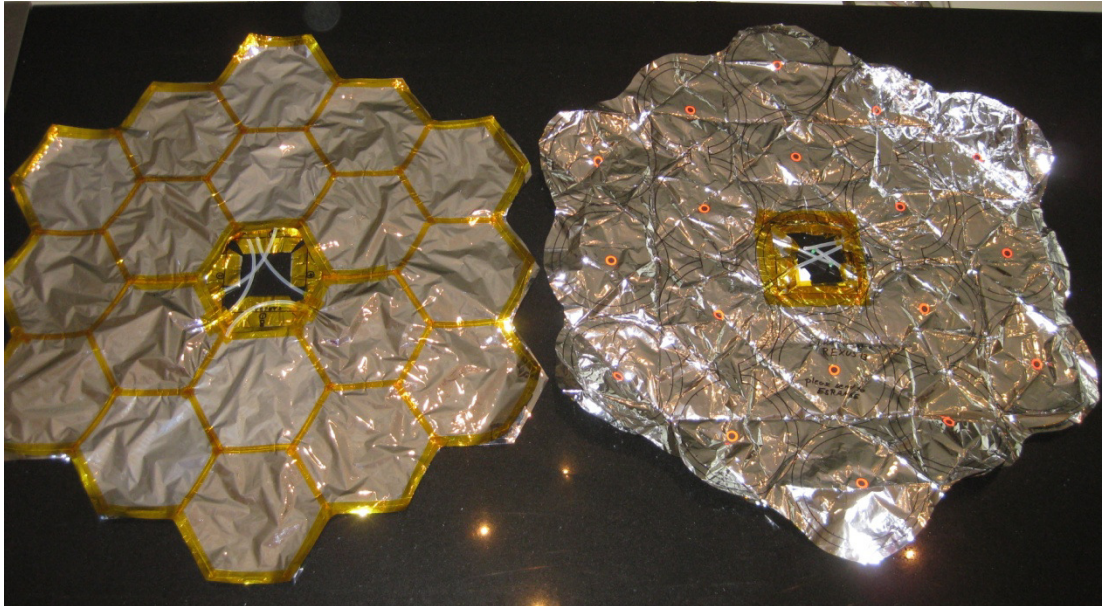


Figure 4-34: Inflatable cellular structures for 2014's REXUS15 mission to the left and 2013's REXUS13 mission to the right

The hexagon approach reduces the unused area between the cells (the triangular shapes in the 2013 structure) that also form enclosed volumes that inflate in vacuum and therefore creating unwanted side effects. With the hexagon approach only the volumes of the cells can inflate and the shape of the final structure becomes more controllable and comparable to undertaken simulations.

Storage and folding patterns

In order to achieve the deployment of such a large structure, storage options and folding patterns needs to be investigated very closely. The initial flat nature of the uninflated structure enables the use of highly efficient folding techniques to decrease the storage volume. Furthermore, the right choice of folding pattern can greatly increase the reliability of the deployment and also its shape adaption capability. One example here would be the Miura-ori folding pattern (Figure 4-35).

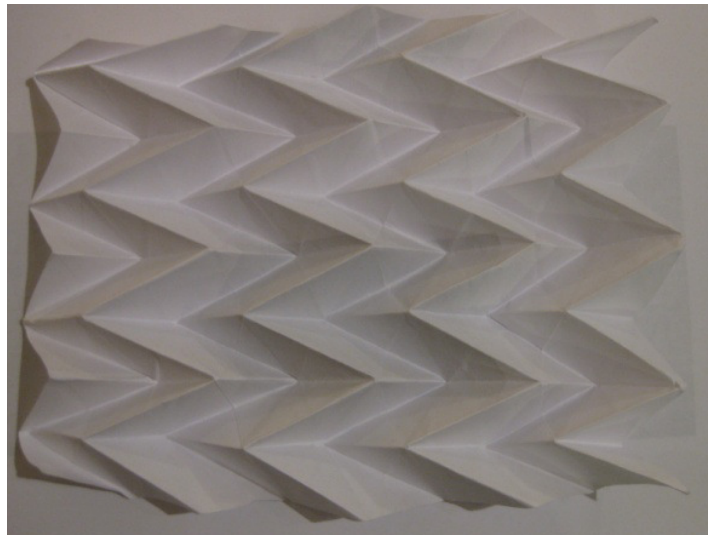


Figure 4-35: Miura-ori folding pattern on flat sheet of paper

The Miura-ori fold [96] can be packed into a very compact volume with its folded out of plane thickness which is only governed by the thickness of the material. The entire Miura-ori folded sheet can be easily unfolded by pulling on two corners of the membrane and likewise folded again by pushing the corners back together. This unfolding scheme can also be applied between just two folds of the Miura-ori fold which results in an unfolding of the entire structure. By applying this folding pattern to the multiple cell structure of the developed structure the deployment reliability of the entire structure is increased because even if a few of the spheres don't inflate, the other functional folds force a flat deployment with the Miura-ori fold.

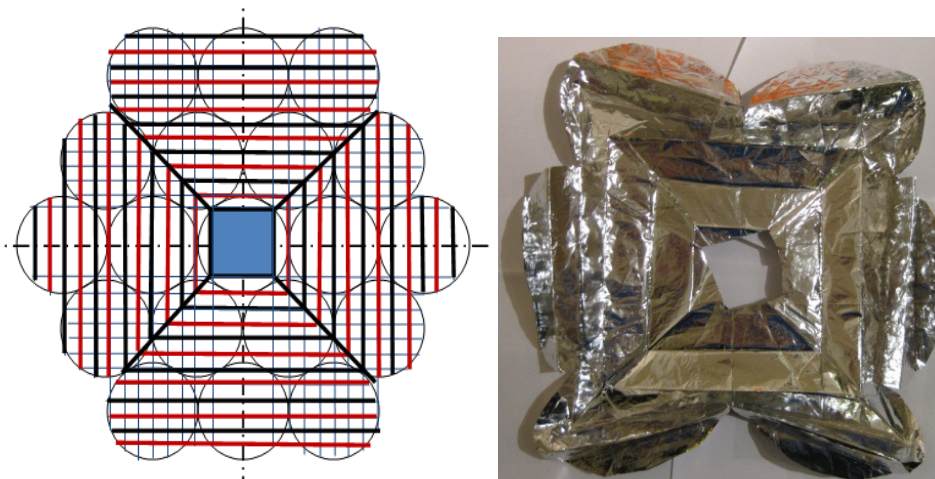


Figure 4-36: a) Schematic of star folding pattern and b) Benchtest structure consisting of six cells folded with star folding pattern

The star folding pattern is mostly used in the folding of solar sails. This folding pattern consists of valley and mountain folds rectangular arranged with a cross point at the edges. Figure 4-36a) shows the schematic of the folding pattern with cease lines in light blue, valley folds in black and mountain folds in black. Symmetric deployment from one central point can be achieved with this folding pattern. The corners of the initial rectangular sheet are longer after folding than the edges in-between the corners. The additional material can be wrapped around on central point for storage. The star folding pattern is quite complex and requires a pre ceasing of the membrane because of the interaction between various fold lines. Another disadvantage is that at the end of the folding operations the structure needs to be pushed from the outside of the box into the box. This might causes an entrapment of the structure during deployment.

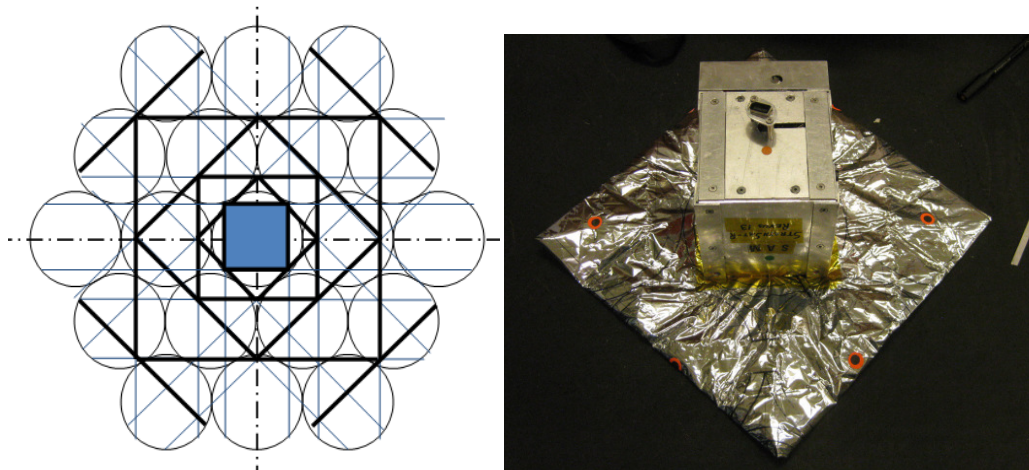


Figure 4-37: Schematic of flower folding pattern left and right StrathSat-R's deployable 36 cell structure during folding inside deployable cube

The simplest and therefore most reliable folding technique is the flower folding pattern. This folding pattern was used for REXUS13's as well as REXUS15's sounding rocket experiment StrathSat-R. The schematic of the flower folding pattern can be seen in a) where cease lines are light blue and the folding lines are black, the flower folding pattern only has valley folds as the corners will always be folded toward the centre. Figure 4-37b shows the StrathSat-R 36 cell deployable during crease operation with four folding towards the centre until the deployable is stored inside the storage box. This folding pattern is very simple and because through its folding from the outside towards

the inside in alternating 45 degrees folds, at deployment the folding pattern already pushes the structure outside the storage box. For this reason, this folding pattern is suggested to be used for this kind of cellular flat structure.

Deployment Simulation – LS-DYNA

To show that the inflation of the structure leads to desired shape, a LS-DYNA simulation was set up to show the feasibility of the concept. Only the inflation and not the actuation could be modelled in LS-DYNA due to the computationally demanding simulations. An array of 18 elements in two rows was modelled for the first deployment simulation for multiple cells. In the beginning of the simulation, the cells were flat in the plane of the 1U cube satellite deployment box. Inflation time was chosen to be again one second, similar to the single cell simulation.

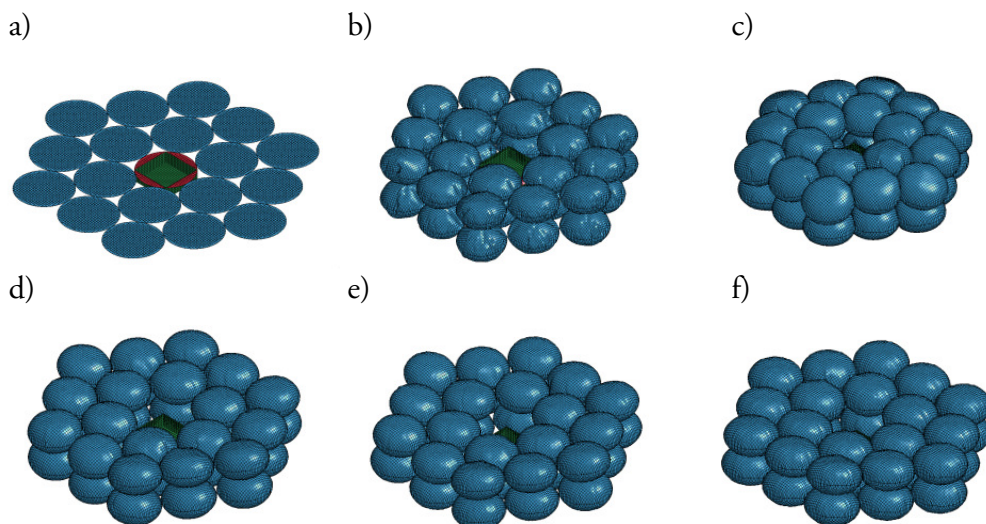


Figure 4-38: Deployment of inflating membrane (blue) out from flat case

The membrane is completely constrained with the deployment box. The deployment box is fixed and can be treated as a rigid body. Figure 4-38 shows the LS-DYNA™ inflation simulation from the flat case in six frames. The first five frames are each 0.1 seconds apart while the last frame is three seconds after initiation of inflation.

The last frame was chosen to be at three seconds to show the final result of the deployed membrane without any oscillation (see Figure 4-39).

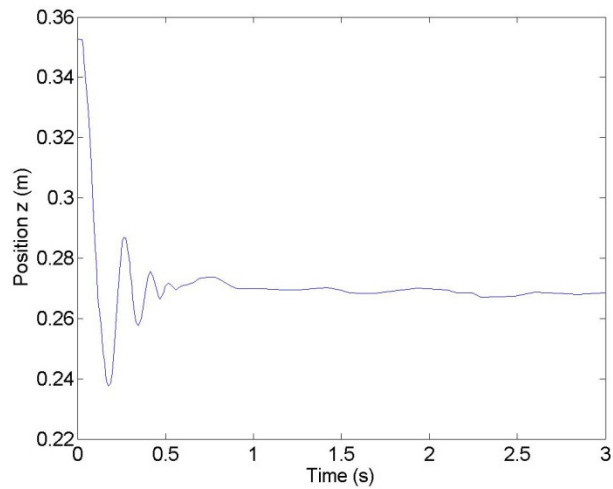


Figure 4-39: Radius of structure during inflation process from flat initial state

Figure 4-39 shows the variation of the radius of the 18 element structure over the inflation time. It can be observed that the radius starts with around 35 cm and levels at around 27.5 cm after an initial bouncing movement over the first 0.5 seconds.

For the second simulation of the multiple cell models, the membrane was compressed into the storage box that lies in the middle of the membrane. Rigid wall movement was used to compress the membrane before inflation.

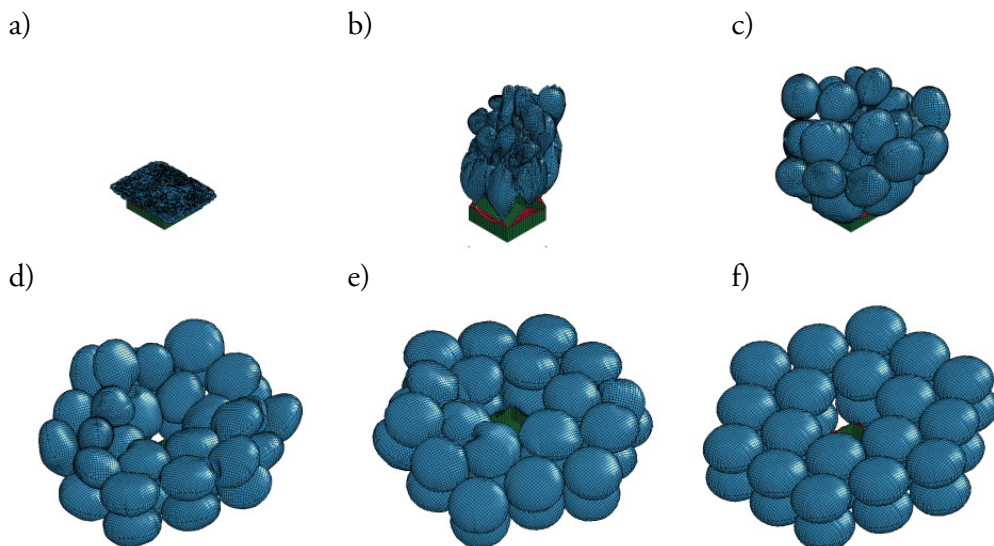


Figure 4-40: Deployment of inflating membrane (blue) out of constrained box (green)

The LS-DYNA deployment simulation can be seen in Figure 4-41. The first five frames are each 0.1 seconds apart while the sixth frame is captured after 3 seconds. The last frame shows that the structure is now the flat desired shape which is similar to the last frame in Figure 4-40. Figure 4-41 shows the radius of the membrane during packaging and inflation.

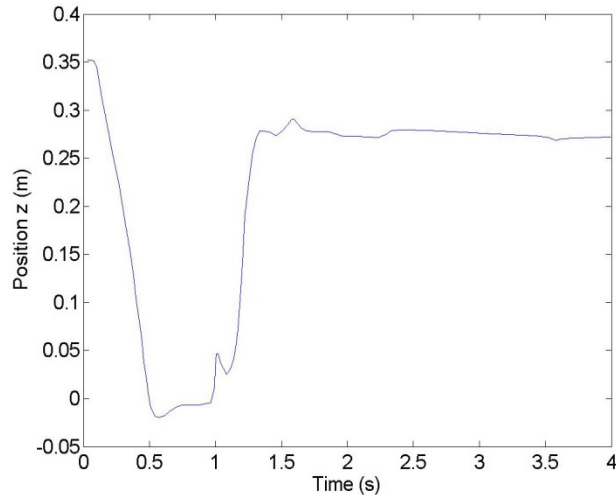


Figure 4-41: Radius of structure during packaging and inflation process from packaged initial state

In the first second, four rigid walls and one rigid wall from the top compress the structure into the deployment box. Inflation starts after the first second and also lasts for one second. Figure 4-41 shows that the initial radius is 35 cm which is leading to an inflated radius of 27.5 cm, the same result as the deployment simulation from the flat state. As expected, it can be seen that the structure obtained has inherently the same shape regardless of the packaging method.

Result of Experiment

At the second launch of StrathSat-R on board REXUS15 in May 2014, the two cube satellites got successfully ejected shortly before apogee at around 86km. Unfortunately, due to a loosen connection between the rocket based experiment and the cube of the shape changing membrane due to vibrations and high g-loads at take-off the experiment

did not start its timeline. Therefore the deployment of the structure could not be recorded. Nevertheless, the second cube satellite that was investigating the possibility of deploying a pyramid shaped inflatable successfully deployed its inflatable proving the concept of residual air inflation. Figure 4-42 shows two pictures taken from the free flying cube satellite deploying its inflatable structure shortly after ejection from the rocket. The structure of the deployed pyramid consisted of four triangular sides with inflatable boom elements at their edges giving the pyramid the necessary stiffness once deployed. Figure 4-42 top shows one of the fully inflated tubes from the cube towards the corner of the pyramid with Mylar material in-between. Figure 4-42 bottom shows one deployed triangular side of the pyramid with inflatable tubes on each edge.

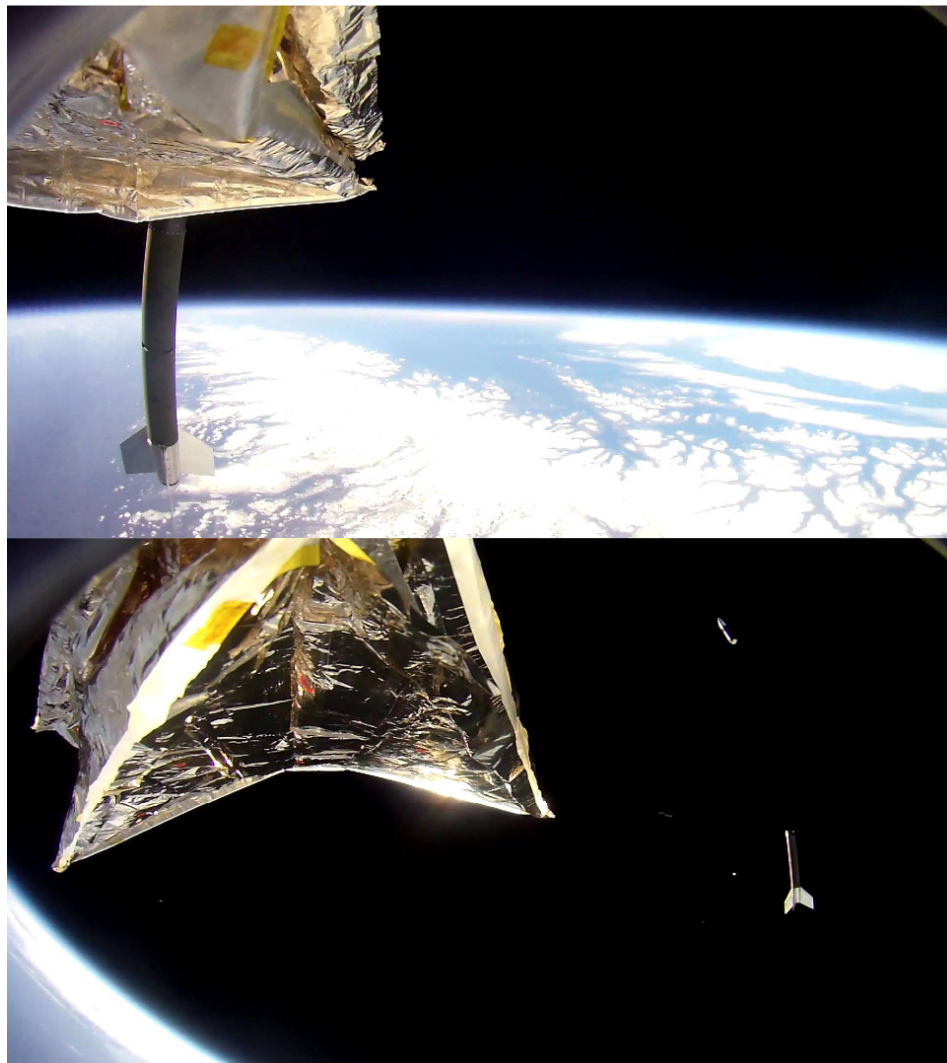


Figure 4-42: StrathSat-R's ejected cube satellite deploying residual air inflated structure

Many lessons were learned and knowledge was gained during the design, fabrication and flight of these inflatable structures. The knowledge gathered at Strathclyde during the sounding rocket and stratospheric balloon experiments enhanced the university's capability to continue research and fabrication of these inflatable structures [97]. In March 2016, the Strathclyde's follow up experiment, PICARD (Figure 4-43), was launched on a sounding rocket and successfully deployed a one meter large inflatable conical helix antenna in space [98],[99]. The experiment used a pressurized container to initiate the deployment and aluminium rigidization (similar to the ECHO balloon) was used to obtain a rigid structure that is not relying on the inflation gas anymore.



Figure 4-43: PICARD's inflated conical helix antenna

The StrathSat-R as well as the PICARD sounding rocket experiments showed that it is possible to obtain a rigid structure in space using inflation. Furthermore the material properties obtained will be used to simulate a larger structure in space.

4.3 Application II: Smart Beam Elements in Space

Another interesting application of the developed structure is the use as a long boom element. These large structures are needed to enable various different missions also from small satellites that require a large distance between the apertures. As an alternative to formation flying, very long booms can be used to keep the relative distance between parts of the spacecraft. Other applications could be the use of these long booms as structural connection elements to build an orbital infrastructure. Furthermore these booms could be used for space telescope applications where the optics need to be held at a large distance to the reflecting mirrors.

Similarly to the reflector application, this subchapter is also structured to first discuss the general concept and system design, then delve into the theoretical part on how the beam element could be simulate when orbiting around the Earth to be followed by a feasibility assessment with an stratospheric balloon experiment.

4.3.1 Concept and System Design

The LEO beam demonstrator needs to be designed that its length is much larger than its cross section. Furthermore the structure needs to be built in a way that it can quickly alter its shape. The idea behind this concept is that the multiple inflatable cells are joined together and due to their changing shape can alter the moment of inertia of the orbiting structure and perform attitude control tasks. To validate the performance of the developed model in an orbiting set up, an application in Low Earth Orbit was chosen.

4.3.2 Simulation

The simulation of the beam element orbiting the Earth had the main purpose to investigate if the flexible structure will be influenced throughout its orbit due to perturbing forces. To validate the analysis a 1 cell element was placed in an LEO orbit with a distance to the centre of 6771000 meter and an initial velocity of 7.6723 km/sec

which leads to a circular orbit with an orbital period of 92 minutes as expected. The velocity over position plot as well as the polar plot of the centre of the beam element is shown in the figures below.

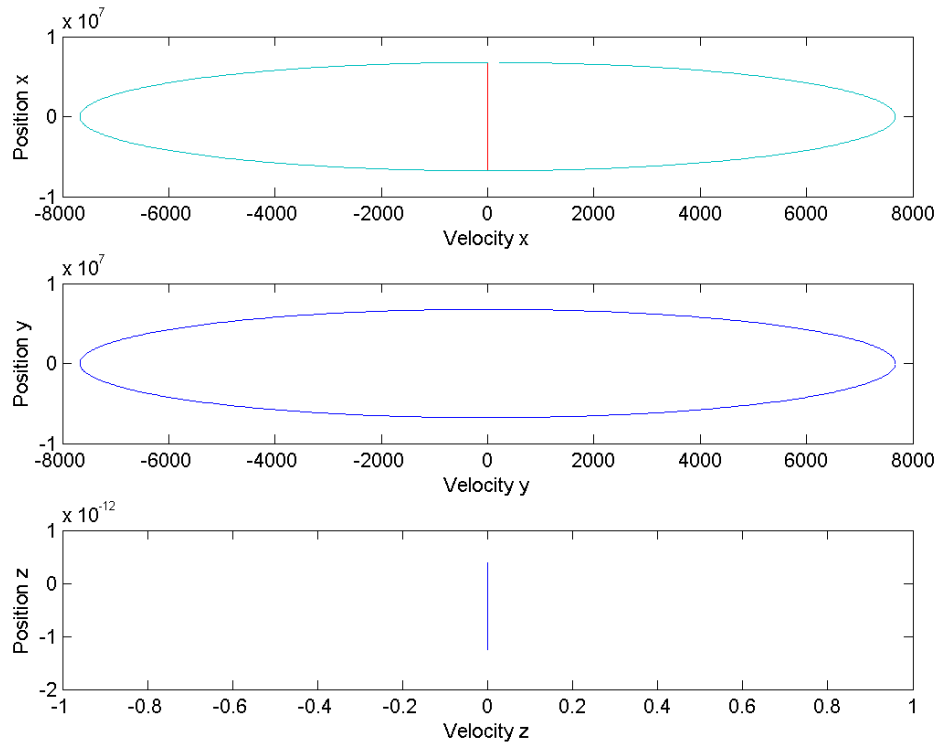


Figure 4-44: Position over velocity for orbiting structure

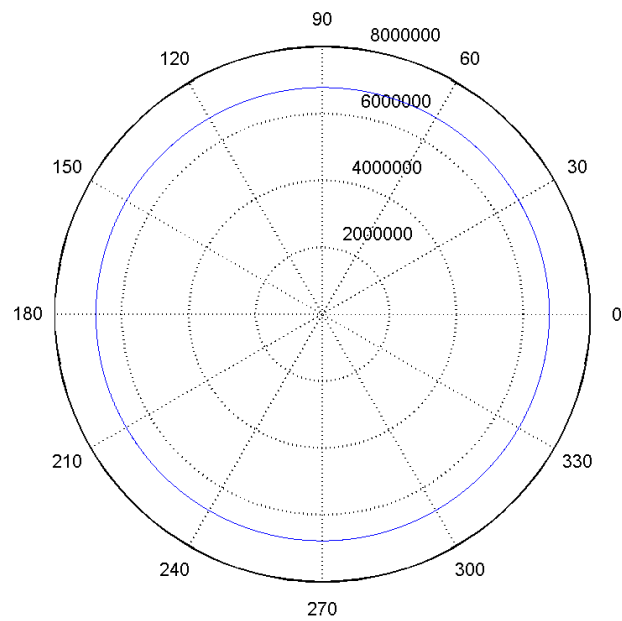


Figure 4-45: Polar plot of orbiting element structure

From the graphs it becomes obvious that the element is on a constant LEO orbit without any perturbation due to its small size. It was concluded that the code was working properly in balancing the differential gravity and the velocity introduced centrifugal force to stay in a circular LEO orbit. The relationship between the reference frame of the orbiting spacecraft to the reference coordinate system is given in Figure 4-46. The rotation matrix outlined in Chapter 3.3.1 is used to transform between the two reference frames.

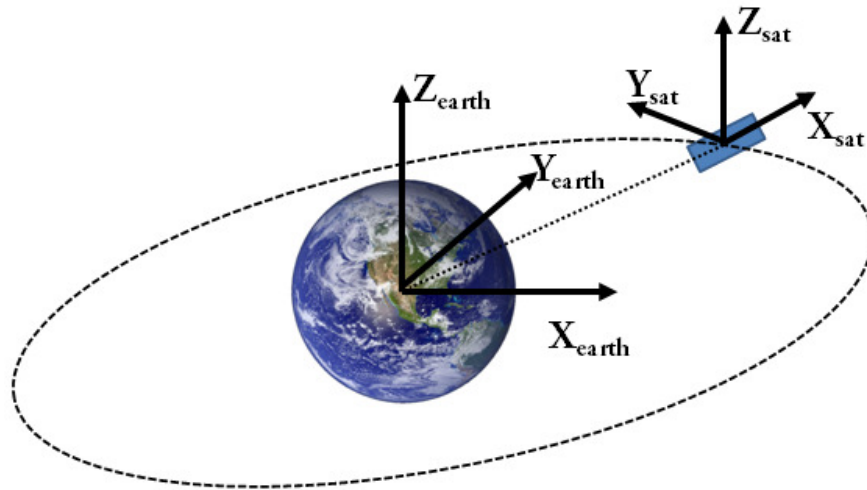


Figure 4-46: Relation between reference coordinate system of Earth and spacecraft

A beam architecture consisting of 50 inflatable cells joined in a 1x1x50 orientation was used to observe the behaviour of the structure during the orbit. The boom structure was oriented in three different configurations which can be seen in Figure 4-47. With this 1x1 cell cross-section, the structure cannot perform out of plane deformations due to actuation of opposite cells but also only the change of length of the cells through external forces can help to alter the orientation of the structure by itself. For this reason, the boom elements were just being deployed via inflation and set on orbital path around the Earth to investigate the deformation of the structure caused by external forces like the gravity gradient.

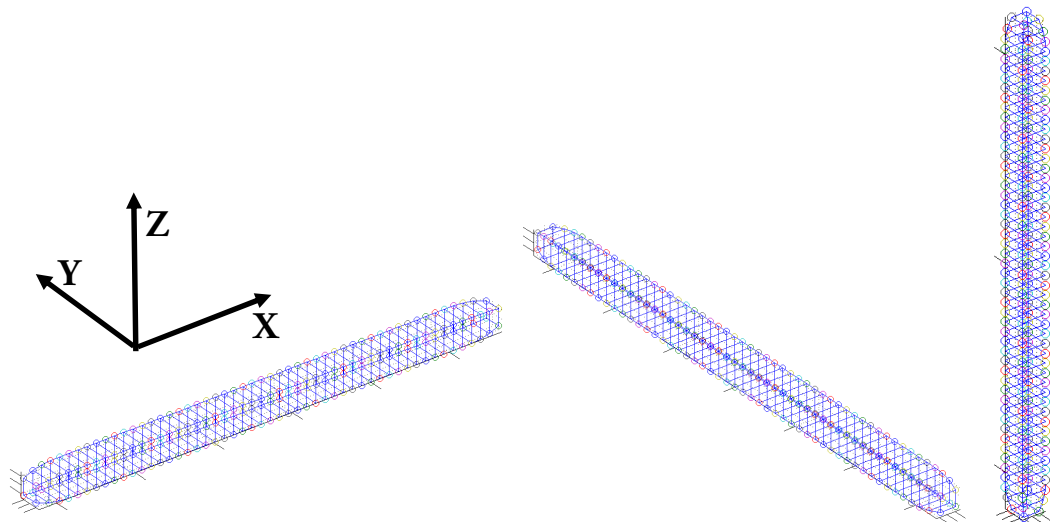


Figure 4-47: a) Beam element oriented in x-axis (50x1x1), b) in y-axis (1x50x1) and c) in z-axis (1x1x50)

The initial starting point of each of the configurations is at an x-displacement of 6771km and a velocity of 7.6723 km/sec in positive y-direction. At the beginning of the simulation, the axes of the Earth reference frame as well as the spacecraft reference frame are aligned. The simulations were run for more than one orbit leading to a total simulation time of 6000 seconds.

On the following three pages the results of the different configurations can be seen. Every configuration has two graphs, the first one shows the displacement of the centre of mass of the spacecraft from the ideal circular orbit shown in Figure 4-45. With these graph (Figure 4-48 for the beam oriented in x-direction, Figure 4-50 for y and Figure 4-52 for z) a prediction can be drawn of the path of the whole spacecraft.

The other graphs for each beam orientation (Figure 4-49 for x, Figure 4-51 for y and Figure 4-52 for z) show the position of each of the nodes of the deploying structure over the simulation time in the reference frame of the spacecraft. These graphs also show the deployment of the structure and any variation of the nodes with regard to the centre of mass of the spacecraft. Furthermore, these graphs can also be used as an indication of the size of the deployed structure in orbit which is in the order of 12m x 0,4m x 0,4m.

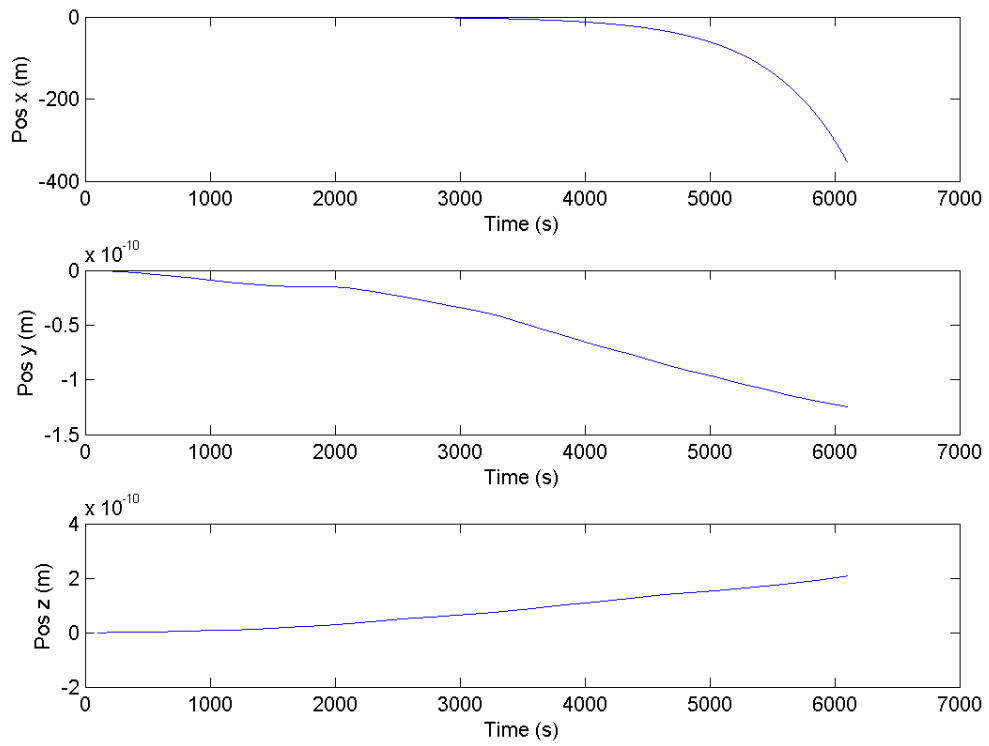


Figure 4-48: Difference to perfect LEO orbit for x-beam. (S/C CS)

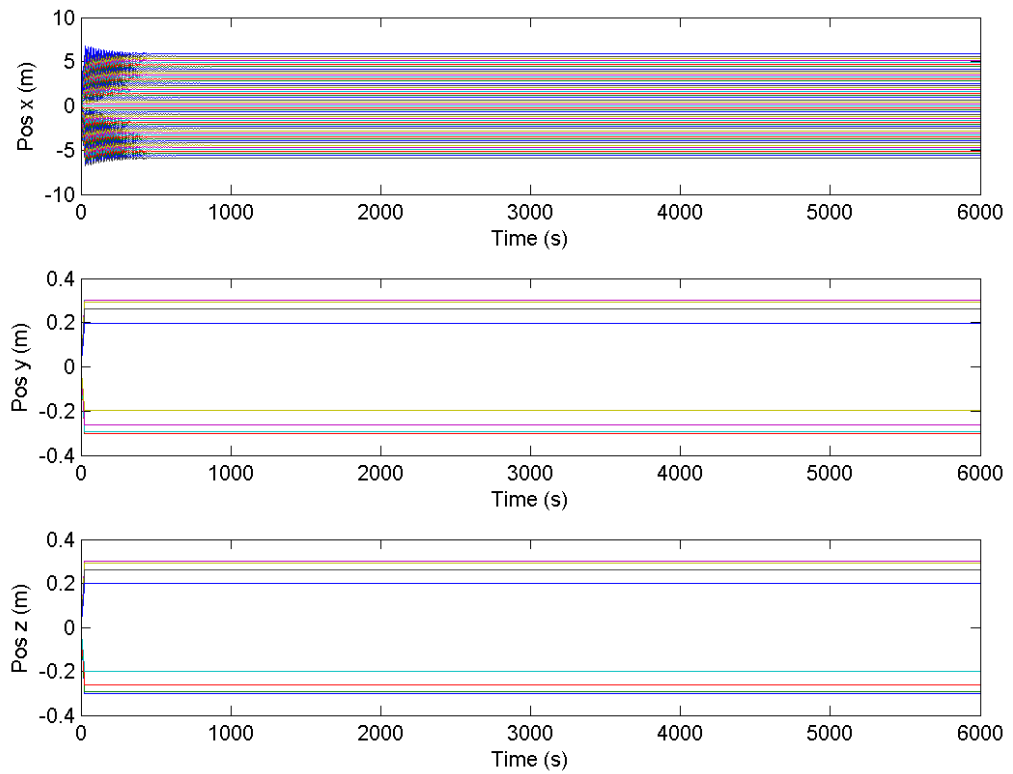


Figure 4-49: Displacement of nodes x-beam. (S/C CS)

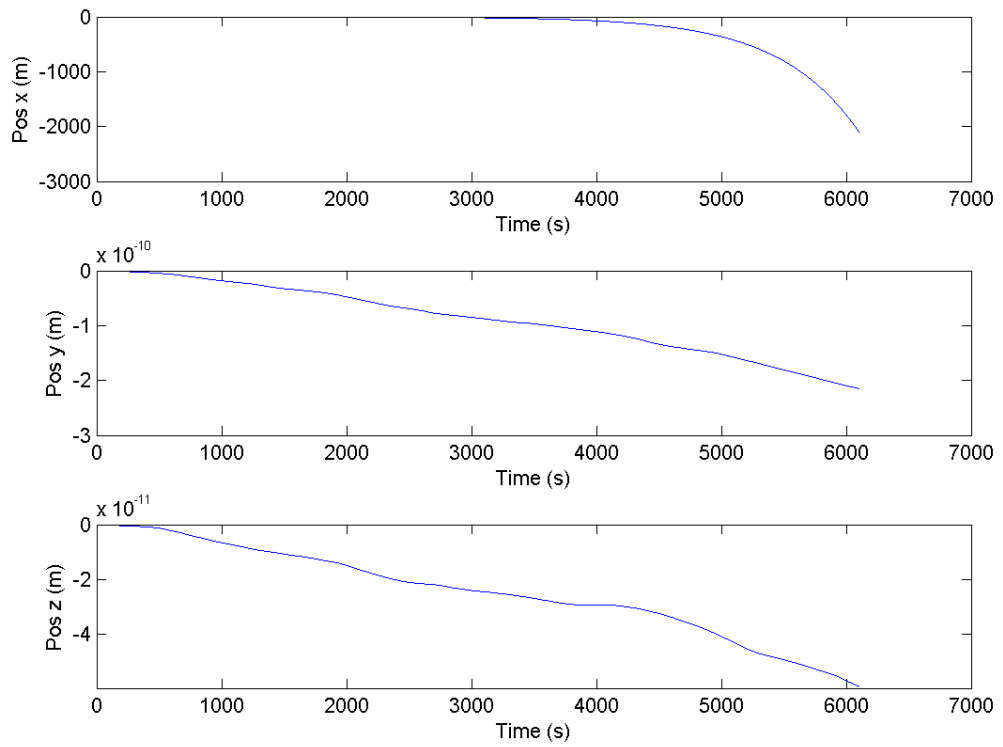


Figure 4-50: Difference to perfect LEO orbit for y-beam. (S/C CS)

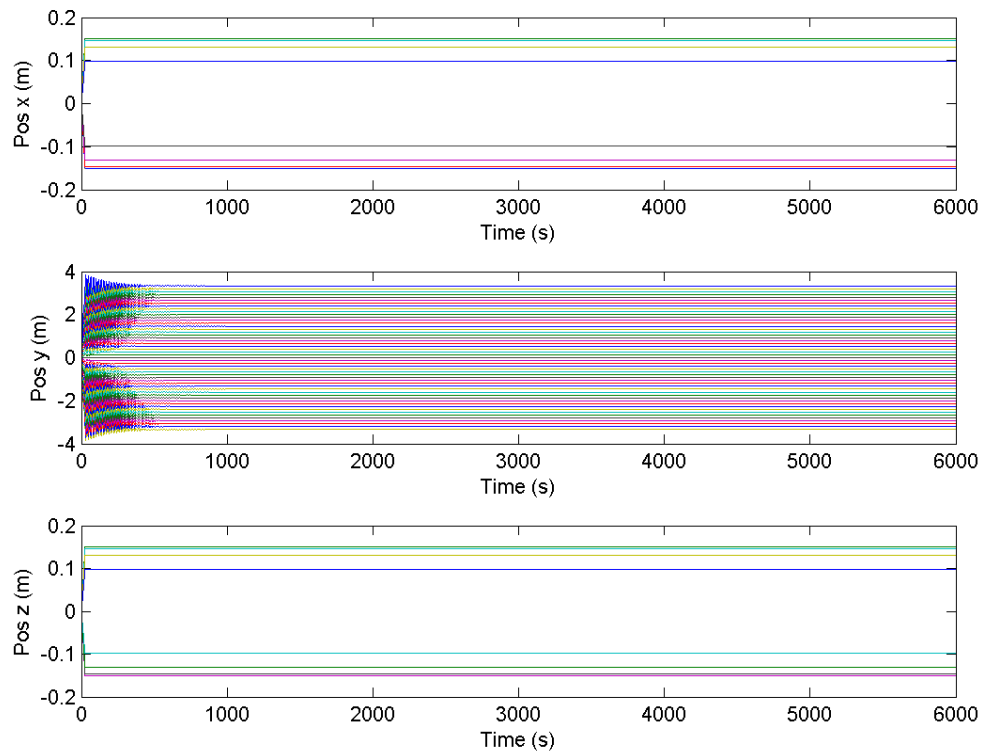


Figure 4-51: Displacement of nodes y-beam. (S/C CS)

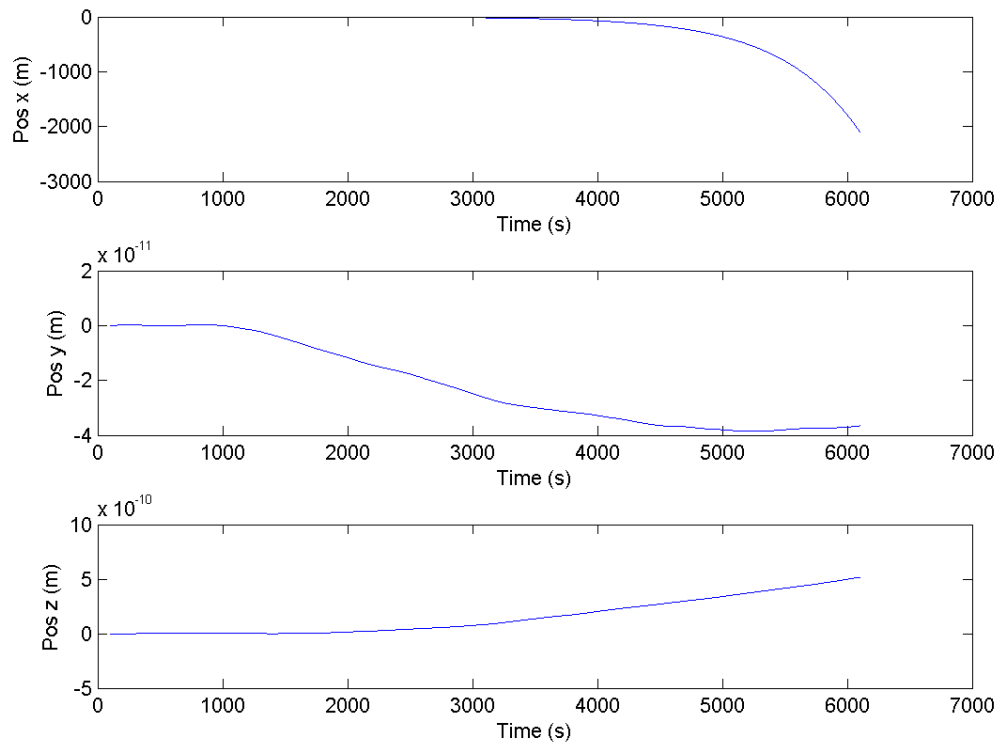


Figure 4-52: Difference to perfect LEO orbit for z-beam. (S/C CS)

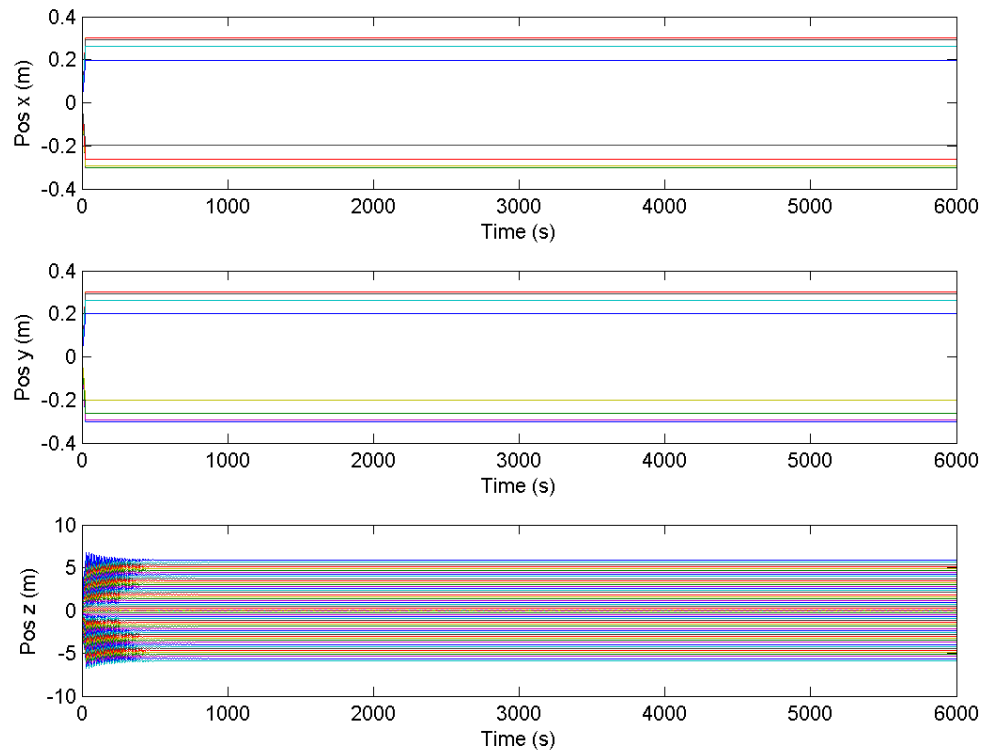


Figure 4-53: Displacement of nodes z-beam. (S/C CS)

The figures above showed that in each case, the orbiting beam element is being pulled towards the Earth (negative z-direction in spacecraft reference frame) by differential gravity. The simulation of a single cell with a concentrated mass in Figure 4-44 shows a undisturbed circular orbit. In comparison, the z displacement of the the long beam simulation is significant. For the x-axis beam the displacement is of the order of 400m while the displacement for the y-axis beam and z-axis beam is over 2000m. The displacements in y and z direction are negligibly small. The displacement in the second graphs of the nodes on the other hand showed no significant change over the simulation time.

In a second step to observe if there are other advantages of the flexible structure orbiting around Earth, the reference frames were changed. In the following simulation the axis of the spacecraft and the orbit stayed parallel but displaced from each other with the orbital distance (e.g. the x-axis of the Earth is the same as the x-axis of the spacecraft). With this simulation the beam element is oriented differently in each quarter. This resulted in interesting orbital dynamics; the polar plots of the centre of mass displacement from the perfect LEO orbit of the three booms are shown in the following figures.

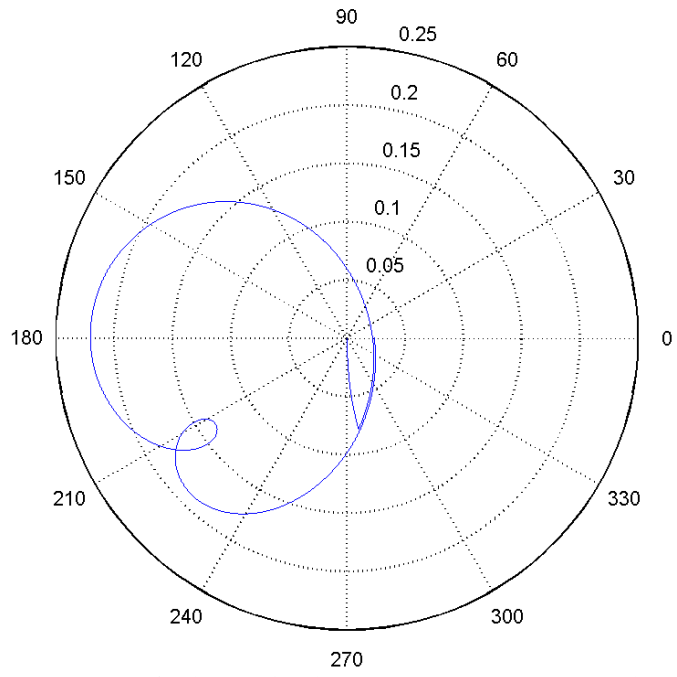


Figure 4-54: Polar plot of relative displacement in meters (x-axis beam)

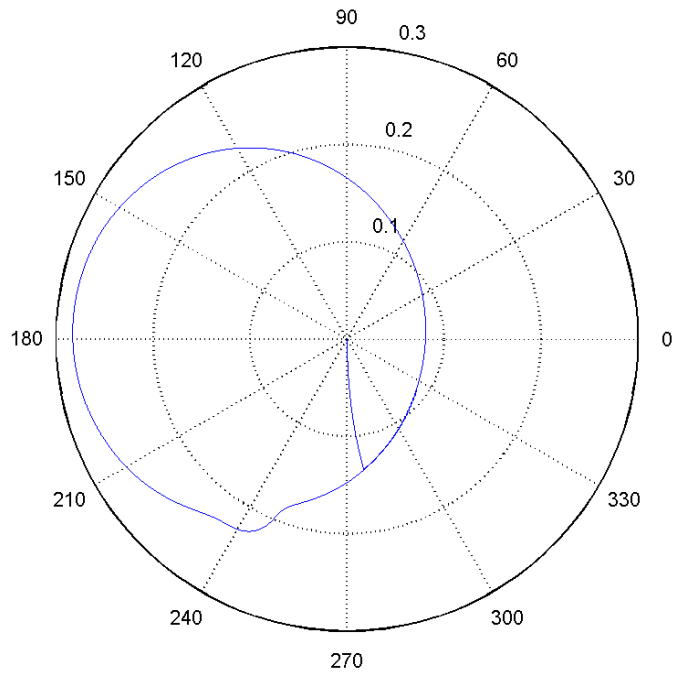


Figure 4-55: Polar plot of relative displacement in meters (y-axis beam)

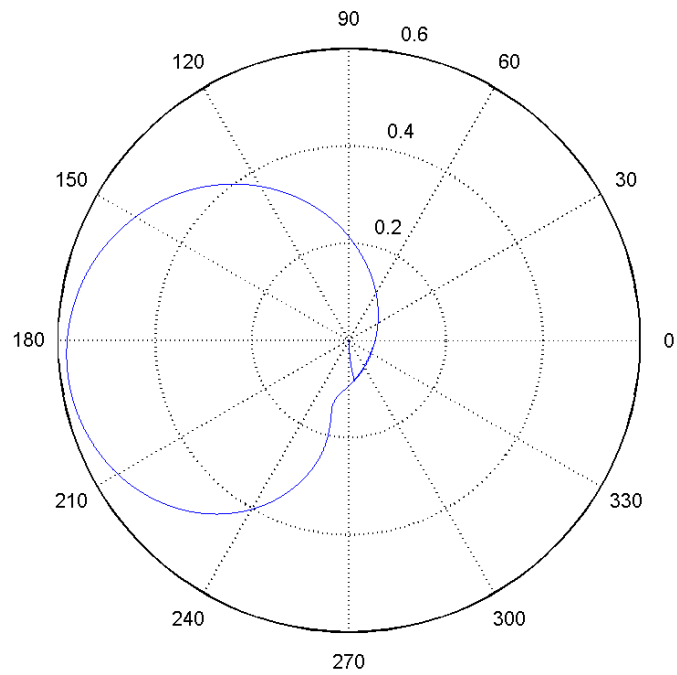


Figure 4-56: Polar plot of relative displacement in meters (z-axis beam)

These polar plots showed that these highly flexible structures can have an interesting behaviour and they might be suitable for missions that common spacecrafts offer no competitive solution.

Summary

In the simulation, a 50x1x1 beam element in three different orientations was deployed via inflation and set on an orbital path around the Earth to investigate the deformation of the structure caused by external forces like the gravity gradient. The simulation time was set to 6000 seconds (roughly one orbit) and the simulation showed that the beam is being pulled towards the Earth by gravity which was expected. Only small variations were recorded in the displacement of the beam itself which is most likely caused by the relatively short simulation time. Another approach of reorienting the beams during their orbit showed also promising results.

As a practical application for the long beam element, the iSEDE experiment investigating the creation of an all inflatable satellite with using disaggregated electronics is detailed in the following.

4.3.3 Experiment: iSEDE

iSEDE [100][100],[101] stands for Inflatable Satellite Encompassing Disaggregated Electronics and it was flown for 5 hours in the stratosphere at 29km as a payload of BEXUS 16. A detailed description including experiment design, launch campaign summary and result evaluation of the iSEDE experiment can be found [102].The experiment had the goal to deploy a prototype of an all-inflatable satellite with disaggregated electronics. The idea was to use inflatable, cellular structures as support for all the subsystems composing a typical nano-satellite. Each subsystem and component is mounted on a different cell. Cells are both individually inflated and individually controlled. The aim was to design and build a prototype for this new type of satellite, demonstrating the deployment and communication among components.

Experiment Design

The first objective of the iSEDE experiment was to deploy the satellites made up of multiple cells via inflation and observe the deployment behaviour and to verify existing LS-DYNA simulations. To demonstrate disaggregated electronics with wireless communication between satellites was the second objective. The third objective was to demonstrate autonomous behaviour of the whole system. The fourth and last objective it to alternate the shape of the satellite via integrated soft robotic actuators and micro pumps.

The concept of the iSEDE experiment was to have two inflatable satellites on board the BEXUS gondola and a central controller, the hub. One satellite is deployed before launch and the other was deployed when the balloon reached float altitude. When all

satellites were deployed, communication between the satellites and the hub commences. The hub communicates with the ground station through the BEXUS E-Link.

The main concern of the mechanical design was the size, shape, strength and mass of the experiment in order to fit inside the given volume of the BEXUS gondola. The iSEDE experiment consisted of the inflatable satellites, the deployment modules, the hub, the camera housing and associated interfaces.

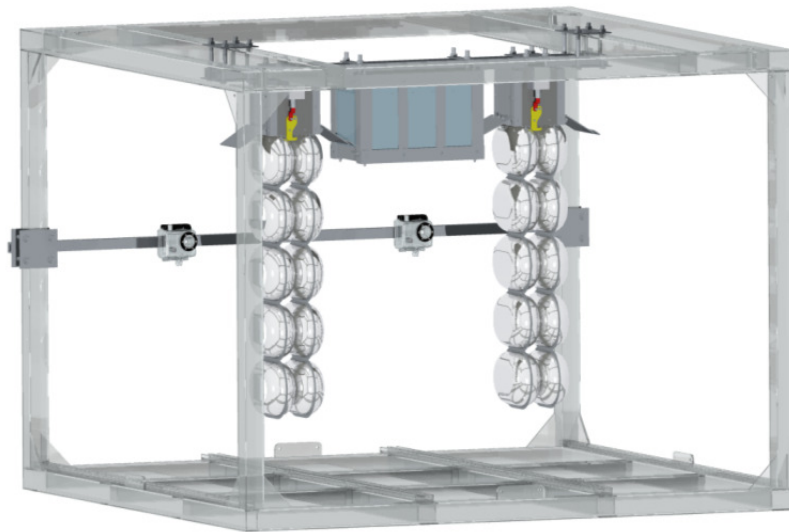


Figure 4-57: iSEDE experiment in BEXUS gondola

The deployed structure was entirely made of inflatable cells. It consisted of two rows of five elongated ellipsoid cells deployed using the expansion of trapped air inside the ellipsoids when subjected to vacuum conditions. These cells were manufactured from an outer layer of adhesive Kapton and an inner layer of Mylar. These films are lightweight, strong and can withstand the temperatures that the experiment will be subjected to. The three middle cells (2, 3 & 4) included a soft robotic actuator element. This actuation element was not affected by the harsh temperature but may degrade when subject to UV radiation.

Each cell has an un-inflated length of 18cm and height of 13cm with a 1cm seam. The deployable structure uses residual air inflation as a deployment mechanism. The

inflation deformation of the cell is modelled using the equations established for the inflation of a flat circular shape presented in [75].



Figure 4-58: Inflating iSEDE Mylar/Kapton cell in vacuum chamber

The adapted heliotropism principle described in Chapter 3.1.2 is used for the shape alteration of the inflatable iSEDE satellite. Initially the concept was based around micro pumps being attached between two adjacent cells to change the cell's pressure and therefore their volume resulting in a deformation of the entire structure. But due to the inflexible nature of the used material Mylar/Kapton composite, another solution had to be created. A solution is the use of soft robotic elements inside the Mylar/Kapton cells enabling the cells to contract once the soft robotic element is actuated. These soft robotic elements are made of highly flexible silicon rubber; soft robotic actuators are used to create dedicated motion using pneumatics in an application oriented design. The advantage of soft robotic elements is that they can be cast in every thinkable shape and their actuation performance can therefore be tailored. Soft robotic elements usually have a cavity inside them which can be inflated causing a deformation of the element. Applications of these softrobotic actuators lie within controllable tentacles or grapping

devices [59]. An actuator developed at the University of Strathclyde to investigate the shape deformation capability of a smart flexible structure with these actuators integrated will be described more in detail in the following.

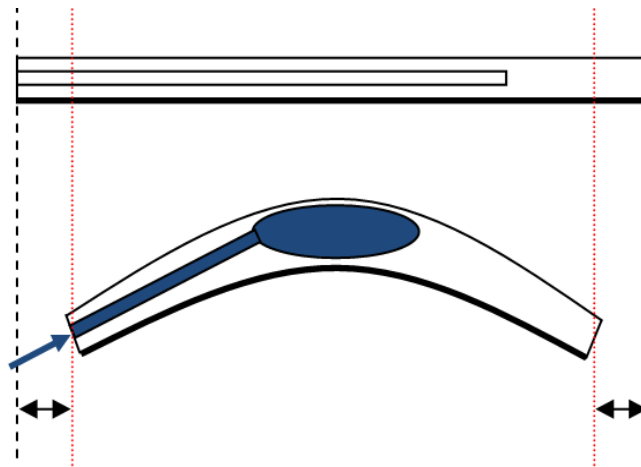


Figure 4-59: Principle functionality of a soft robotic actuator inside Mylar/Kapton cells of iSEDE

The functionality of a softrobotic actuator, which is placed inside the iSEDE Mylar/Kapton cells, can be seen in Figure 4-59. On the top, the actuator made out of silicon rubber has a cavity that runs through almost the entire length of the actuator. If this actuator cavity gets filled with fluid or gas, the actuator elongates due to the internal increased pressure of the fluid. But there are many applications where a shortening of the actuator is more useful like in the iSEDE experiment where a softrobotic actuator is used to change the shorten the length of semi rigid inflated cells to change the shape of the structure. To realise a shortening of the actuator, a stiffer but still flexible material is introduced on one side of the actuator making the structure to curve and bend when actuated. This principle can be seen in the bottom half of Figure 4-59. The bending of the soft robotic actuator results in a shortening of the whole actuator.

To observe the shape changing behaviour and to improve the design of the actuator, further experiments have been carried out. For these experiments a softrobotic actuator of 5mm x 5 mm with a 2mm diameter cavity with nylon wire on one side to increase the stiffness has been used. Antifreeze fluid (pink fluid in Figure 4-60) with a viscosity

similar to water was pumped via a MEMS micro pump with a mass inflow of 7 ml/min into the actuator.

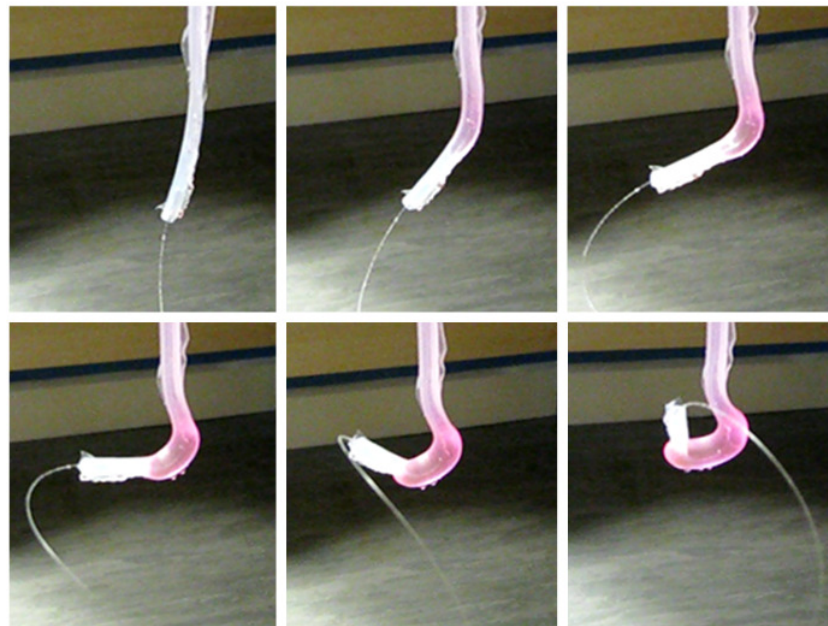


Figure 4-60: Deformation of actuated soft robotic actuator

The vertical and horizontal deformation of the actuator can be clearly seen in Figure 4-61 during the actuation time of 45 seconds. It also becomes obvious that increases in mass due to increased fluids leads the actuator in this experiment to elongate due to gravitational forces pulling downwards. This phenomenon would not appear in space and it is to be expected that the actuator would shorten even more.

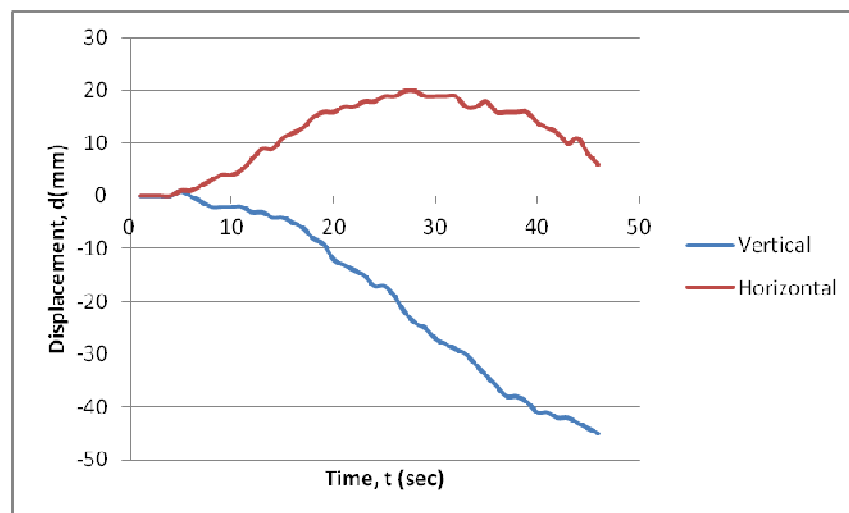


Figure 4-61: Displacement graph of actuated soft robotic actuator from Figure 4-60

The horizontal (red) and vertical displacement (blue) over the experiment time is displayed in Figure 4-62. From this experiment it can be taken that the shortening (vertical displacement) is linear and was used in the iSEDE beam actuation simulation with the developed code from page 146 onwards (Figure 4-66 and Figure 4-67). Figure 4-62 shows the soft robotic actuators (yellow lines) embedded in the centre cells of the iSEDE deployable. Once the soft robotic element is actuated, it shortens itself and compresses the cell. This compression in z direction (see Figure 4-30) for coordinate system definition) leads to a displacement of the structure in y direction.

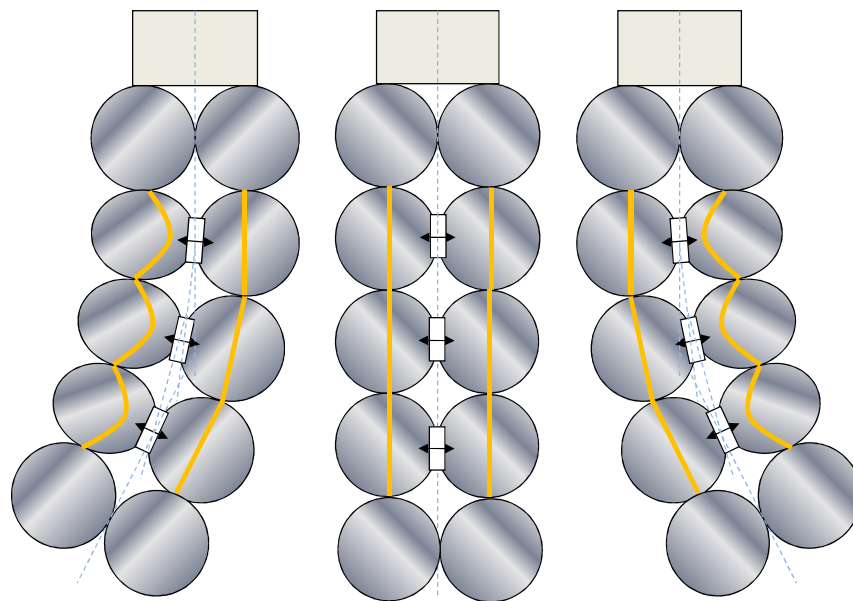


Figure 4-62: Actuation of satellites (soft robotic actuator = yellow lines)

By using the soft robotic principle with micro pumps, the iSEDE inflatable obtains the capability of changing its global shape. An actuator element consists of two soft robotic elements connected by a micro pump can be seen in Figure 4-63. The soft robotic actuators are placed in neighbouring cells (y-direction) with the micro pump in between the cells.

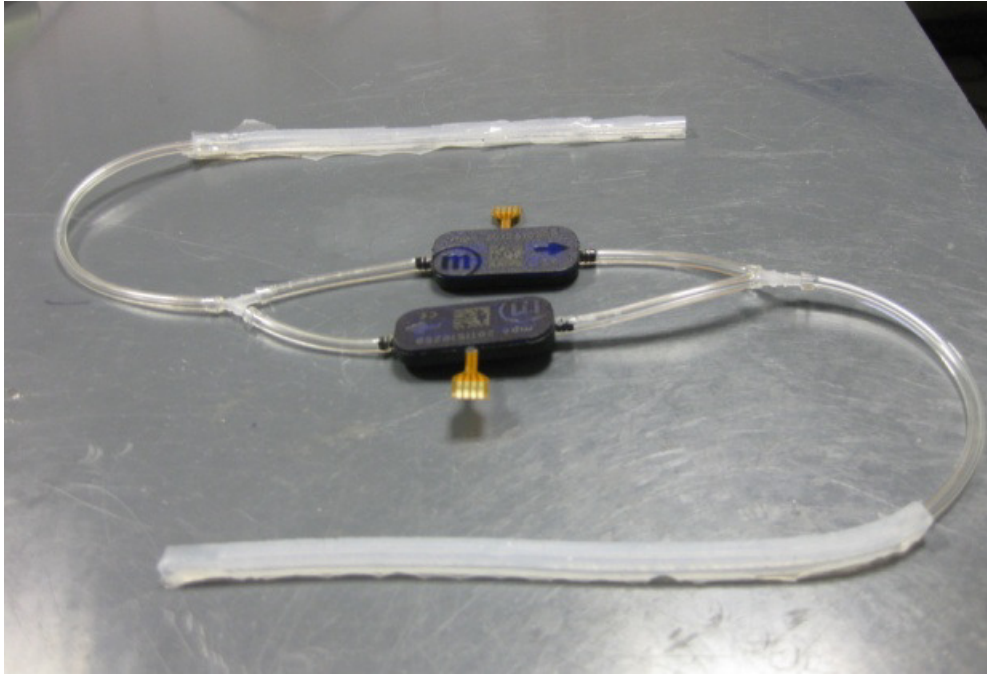


Figure 4-63: Actuator element consisting of two micro pumps for reversible flow and two soft robotic actuators

During fabrication, a cavity inside the soft robotic actuator was created with a metal rod. In order to create the necessary higher stiffness on one side of the actuator to force the actuator to bend and therefore shorten, a thin nylon string is placed inside the actuator. If the soft robotic actuator gets inflated which would normally cause an elongation is now getting transformed in a bending of the actuator, which means an in plane shortening with a comparably high actuation force. During fabrication the actuator tool is placed inside a vacuum chamber to remove small air bubbles from the soft robotic actuators to improve the quality of the actuator.

The deployment modules are simple 1U (10x10x10cm) boxes made of lightweight aluminium. The deployment method used contains a solenoid which is connected to a linkage arm which in turn is connected to a latch. All components in the iSEDE experiment were COTS and have been selected as they have low mass, volume and footprint. Regarding to their datasheets, they should also work within the harsh environmental operating conditions. The system architecture is designed to be robust and fulfill its purpose with the minimum components and simplest implementation.

The electrical system can be divided into two subsystems, the Hub and the satellites. Although the experiment launched two satellite units, the electrical systems on each are identical.

The Hub electronics consisted of a data acquisition system, a microcontroller, a power distribution system and wireless transmission system. The Raspberry Pi processing unit controlled the data acquisition system, communication with the satellites and ground station, experiment timeline, solenoid and operates the cameras.

All data received by the Hub over the wireless network is processed by the Hub for storage on the SD card and transmission through the BEXUS downlink to the ground support station.

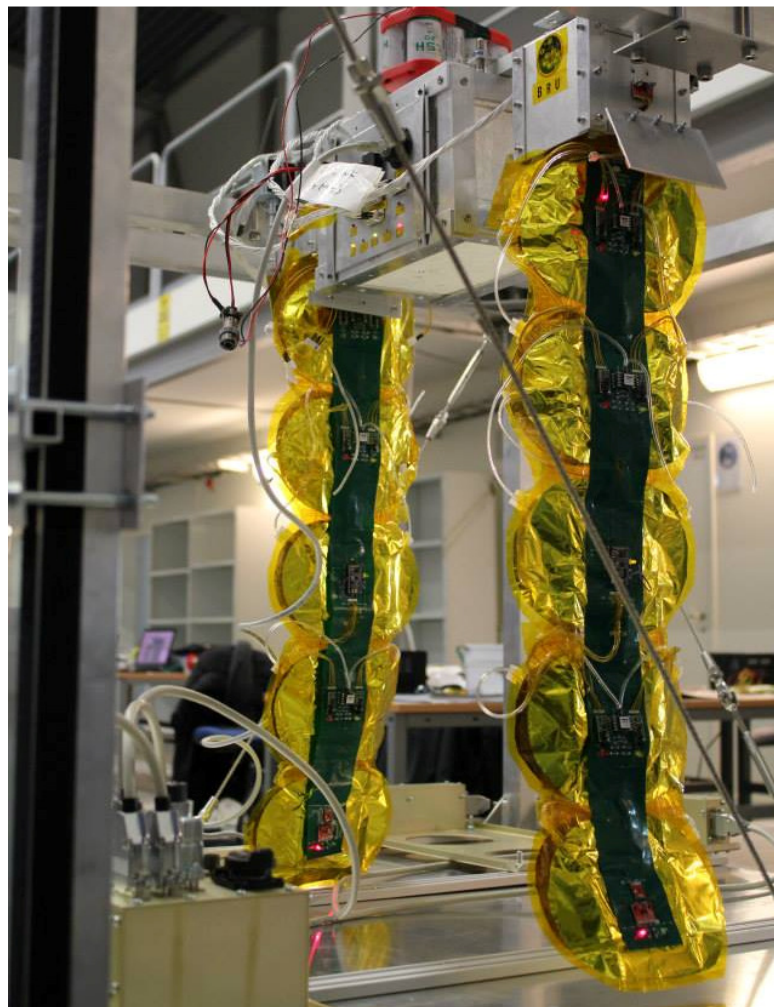


Figure 4-64: Full iSEDE experiment with the two deployed inflatable disaggregated electronics satellites satellite at the launch campaign within the balloon gondola

Each satellite (Figure 4-64) contains a microcontroller, micro-pump actuators with control system, and a number of sensors for environmental readings and housekeeping. The satellite microcontroller's task is to receive commands from the transceiver; carry out actions accordingly; read sensor data and transmit it to the Hub; actuate the micro pumps for shape alteration and implement closed loop control of the actuation process.

Each satellite forms the basis of what would be a concentrated control hub as part of a larger smart space structure. As such, its electronics are designed to facilitate an intelligent performance of various measurements to monitor and control the performance of the structure. Each satellite gathers ambient and component temperature readings along with important voltage sensing for housekeeping. Differential pressure measurements are also being taken to help characterise the inflation of the structure at deployment and throughout flight. The actuation is driven by Bartels micro pumps which are connected electrically to the microcontroller through their own sub-controller (Figure 4-65). The control of the actuation is provided through two accelerometers positioned on the structure. Data is not stored on each satellite; it is instead only acquired and transmitted to the Hub via the wireless link. The data is then processed, stored and sent to the ground support station.



Figure 4-65: Top cell of satellite with pump/pressure sensor unit (cables towards micro pumps).

iSEDE Deployment and Actuation

In the following, a simulation with the developed code has been carried out on the iSEDE structure. The first simulation of the iSEDE structure was intended to show the shape changing capability of the experiment. For this the actuation was based on the capability of the softrobotic actuators developed, tested and implemented in the flight hardware of iSEDE. The iSEDE experiment had an array of 1x2x5 cells and the top two cells were mounted rigidly at the deployment box. For the simulation this mounting situation was taken as a symmetry line for a free flying structure of the length of 1x2x10 cells. The deployed configuration of the 1x2x10 cells can be seen in Figure 4-66.

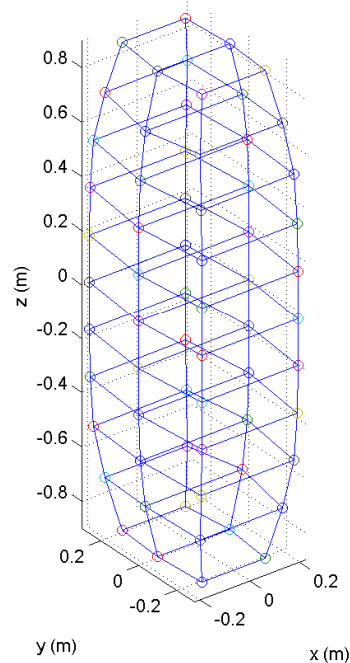


Figure 4-66: Fully deployed 1x2x10 array (iSEDE with symmetry)

To evaluate the shape changing capability of the iSEDE structure, the actual data obtained from the softrobotic measurements during the experiment campaign were used in the model (from the data displayed in Figure 4-61). Figure 4-66 shows the vertical displacement over time for the iSEDE softrobotic actuator.

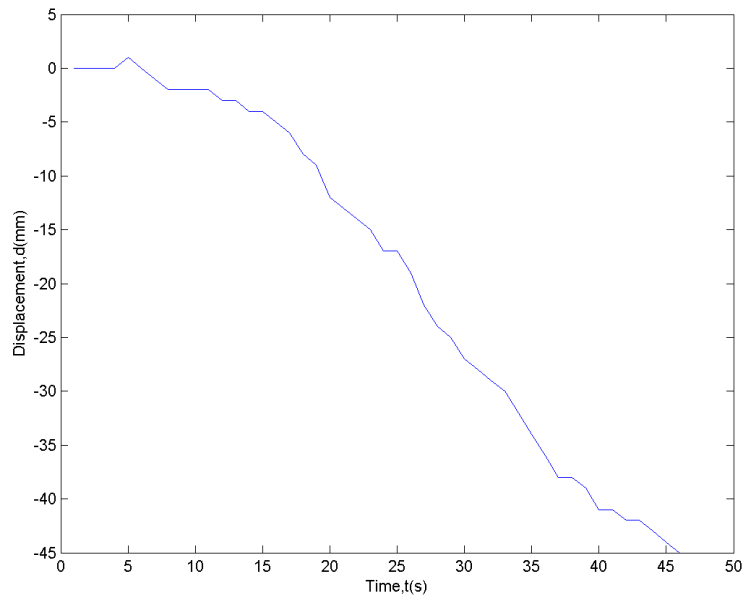


Figure 4-67: Vertical displacement of iSEDE softrobotic actuator

The iSEDE experiment had a pair of these softrobotic actuators in the three centre cells. Each of the actuators was connected to the neighbouring cell’s actuator over a micropump that would pump the fluid from the front to the back actuator. Similarly in this simulation, the front actuator pumps the fluid into the back actuator or vice versa resulting in a positive or negative elongation.

The following table gives the result of the y-displacement for different actuation cycles. In total 8 different actuation cycles are possible when only the flow in one direction is assumed. Only these cases are interesting for this application because these will influence the y-displacement on the bottom cell. A YES in the table indicates that the actuator is being used while the NO indicates that the actuator is unused.

Table 3: y-displacement at bottom for different actuation cycles

Act. Cycle	1	2	3	4	5	6	7	8
Actuator 1	NO	YES	NO	NO	YES	YES	NO	YES
Actuator 2	NO	NO	YES	NO	NO	YES	YES	YES
Actuator 3	NO	NO	NO	YES	YES	NO	YES	YES
y-Displ.	0.00	3.39	1.93	0.87	3.56	6.14	2.05	5.28

The table shows that the structure is capable of controlled deformations also with the iSEDE soft-robotic actuator. Especially the actuation of the top actuator influences the

displacement in the y-direction. An advanced control algorithm that recognises this behaviour could greatly reduce the power to displace the structure by only using the actuators that have the highest influence on the desired shape change.

Launch Campaign and Results

The BEXUS16/17 launch campaign took place in October 2013 from the Swedish rocket/balloon range Esrange. The BEXUS16 stratospheric balloon flew to an altitude of 27,3 km with a flight duration of five hours. During the mission all the disaggregated electronics worked well with wireless communication. Even more, all components were fully functional even at -50C, well below their specification. Unfortunately, the residual air inflation and the shape change of the satellites could not be achieved due to fractures of the soft robotic actuators during on ground handling. The leakage of the antifreeze actuation fluid caused a dissolving of the bonding line between the Mylar and Kapton layers thereby making the cells not airtight anymore.

Summary

The Chapter 4 showed how the concept outlined in Chapter 3 can be realized and brought to orbit with the shape changing colonies assembling versatile space structures. The multibody code was tested for a solar concentrator application that focused the suns energy using while flying by an asteroid. Also, the code was applied to a second application showing that the flexible structure can alter the orbit depending on their orientation. These theoretical results were enriched with the sounding rocket and stratospheric balloon experiments that gave valuable input.

Chapter V

Conclusions and Future Work

5.1 Discussion

The origin of the idea for this smart structure came from the need of large deformable structures in space which is also the field of interest of the author of this thesis. Nevertheless, this structure and principle can be replicated at almost every size with the only limiting factor being the fabrication techniques available today. But with the current trend in miniaturization, this will not be the case for very much longer. The developed structure and simulation code enables the creation of a smart 'sheet' of cells that can transform itself in almost every thinkable shape. This technology might become the next 3D printing because by commanding the structure to form for example a specific part, it is no longer required to bring spare parts to space or to any other remote location.

5.2 Conclusions

A bio inspired system was developed that facilitates inflation as the most promising deployment system and overcomes the gaps within available smart structures to enable a large shape changing structure. The adaption of the ability of certain plants of rather fast movements using pressure change in-between cells to a mechanical analogue bridges those gaps. The proposed mechanical structure is made up of an array of hyperelastic inflatable cells connected by valves and pumps to exchange air molecules and thereby change the internal pressure and therefore their size. The developed multibody dynamics code is computationally inexpensive and is able to run hour long orbital simulations also on a personal PC. With this code it is possible to simulate very large structures in the appropriate environment over longer time periods without the need for expensive fabrication and on ground testing. This was shown in example applications like for a shape changing solar reflector subjected to gravitation and solar radiation pressure

around an asteroid that then optimized its focal point to deliver energy to the asteroid sublimating laser. In conclusion it can be said that the developed technology in this thesis might one day change our daily life because it might be the step further for programmable matter that could be anything we want it to be.

5.3 Future Work

The countless applications and the multidisciplinary character of the developed structure open the room for various areas of future work:

- The principle can be adapted for various different applications but for every specific application and size of the structure a couple of parameters like mass, stiffness and damping matrices must be calculated or obtained through experimentation. To minimize mass and complexity, the structure should be designed specifically for each mission (e.g. which cells need to be deflated, placement of valves, etc.). Further work needs to be undertaken in regards to the proposed application and the used materials and technologies.
- The control of the structure and the architecture of the used electronics need to be investigated further to ensure the most optimal solution. The used PID controller showed good results but some research has been already undertaken at Strathclyde in using Artificial Neural Networks instead.
- An important issue that still needs to be tackled is the survivability of the used technologies and materials in the proper environment. The technologies in question are the electronics specifically the flexible circuits and micro pumps and valves performance under vacuum or low temperatures. The iSEDE experiment already proved that some of technologies worked during a stratospheric balloon flight but especially long duration testing is missing. Similar for the materials where Kapton and Mylar are already proven space materials but where more appropriate hyperelastic materials like Silicon

Rubber needs to prove their space survivability especially considering degradation issues through space radiation or UV-light.

- Another important aspect is the improvement of the manufacturing techniques for all kinds of sizes of the structure from nano to macro. The undertaken work in the fabrication of these structures was more focused on proving the general concept then to develop fabrication techniques for mass production. The selection of appropriate components depending on the size of the to be manufactured structure also needs to be investigated further meaning that the selection of micro pumps for the 10cm diameter cells will not be appropriate for any other size of cells. An important aspect here is the improvement of miniaturization of the subsystems because smaller cells enable an array with more actuators per square meter and therefore its actuation and deformation capability.
- Further space applications include a space telescope that can adapt its optic in space to account for unpredictable thermal expansion in order to increase its accuracy. Also application are envisioned in the field of solar sails where the morphing structure can replace the entire altitude control system by changing the solar sail surface area subjected to the solar wind. As in depth orbital dynamics were not part of this work on the smart deployable structure, detailed work on orbital determination is left for future work. Each of the possible applications would require a dedicated detailed analysis for its trajectory on its depending on its chosen mission.
- An application for planetary or terrestrial rovers can be envisioned as well. The smart cellular structure could be actuated to move similar to a snake over any kind of terrain, or even swim through water. Due to the fact that the actuation works with inflating and deflating the cells, the soft robot rover can actually squeeze through small openings giving it an advantage compared to conventional robots.

Appendix A - Silicon Rubber Benchtest

For the shape change experiments two 4x2x1 layers were joined by using a thin layer of silicon rubber to form a 4x2x2 array. To enable the shape change of the bench test model, the channels in between the cells can be closed or opened with a clip to allow or constrain airflow between the cells similar to the use of MEMS valves. To counteract the effects of gravity, the bench test model was hung by strings attached to two points. The attachment of the gravity off-load system can be seen in Figure A1 between the first and the second and the third and the fourth cell.

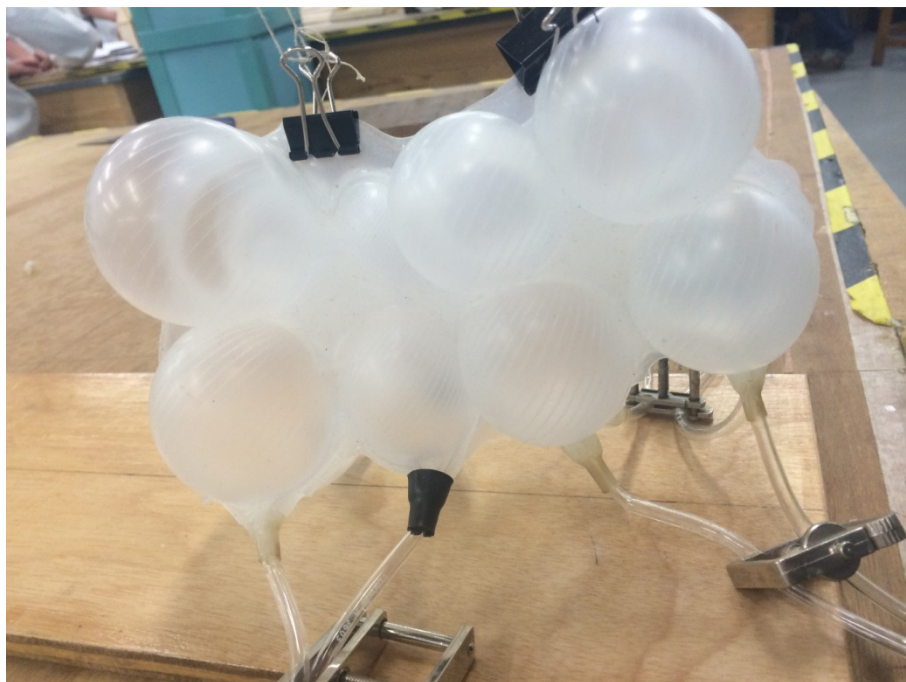


Figure A1: Shape alteration due to different cell volumes

Inflating the cells causes different cell volumes resulting in structure deformation. This can be clearly seen in Figure A2 where just the front 4x2x1 array is inflated and the top middle cell to the left is less inflated than the surrounding cells. This actuation causes the array to form a positive curvature of the centre line.

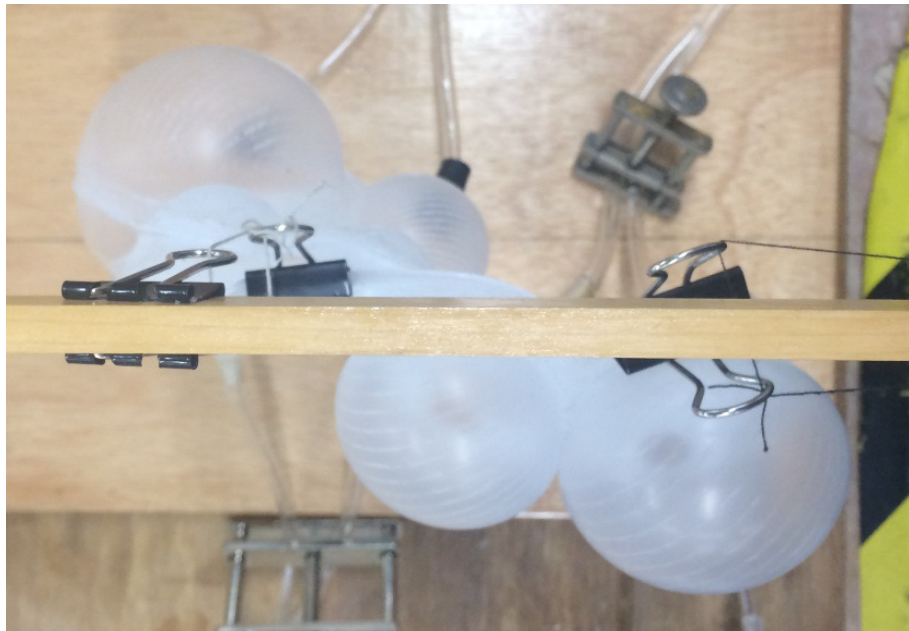


Figure A2: Shape alteration due to different cell volumes

By inflating the two opposing four cells of the array, an S-shaped structure can be obtained. This deformation can be seen in figure above. Bench test models with higher actuation and deformation capabilities and thereby more cells are possible but they require a proper gravity off-loading rig and a lighter smaller air distribution system between the cells.

Bibliography

- [1] J. P. Sanchez, C. Colombo, M. Vasile and G. Radice, “Multicriteria Comparison Among Several Mitigation Strategies for Dangerous Near-Earth Objects,” *Journal of Guidance, Control and Dynamics*, vol. 32, no. 1, pp. 121-142, 2009.
- [2] A. Gibbings, M. Vasile, I. Watson, J.-M. Hopkins and D. Burns, “Experimental analysis of laser ablated plumes for asteroid deflection and exploitation,” *Acta Astronautica*, vol. 90, no. 1, pp. 85-97, 2013.
- [3] M. Vasile, C. A. Maddock, G. Radice, C. McInnes and L. Summerer, “Final Report: NEO deflection through a multi-mirror system, Ariadna ID 08/4301,” European Space Agency, Noordwijk, Netherlands, 2008.
- [4] C. A. Maddock, M. Vasile, C. McInnes, G. Radice and L. Summerer, “Design of multi-spacecraft swarms for the deflection of apophis by solar sublimation,” in *1st IAA Planetary Defence Conference: Protecting Earth from Asteroids*, Grenada, Spain, 27 - 30 April 2009.
- [5] S. Pellegrino, Deployable structures. No. 412., Springer, 2001.
- [6] C. Mangenot, J. Santiago-Prowald, K. van 't Klooster, N. Fonseca, L. Scolamiero, F. Fonseca, P. Angeletti, M. Politano, C. Elia, D. Schmitt, M. Wittig, H. Florence, M. Arcioni, M. Petrozzi and M. S. Taboada, “Large Reflector Antenna Working Group Final Report, TEC-EEA/2010.595/CW,” European Space Agency, Noordwijk, Netherlands, 2010.
- [7] J. Mankins, The first International Assessment of Space Solar Power: Opportunities, Issues and Potential Pathways Forward, Toronto, Canada:

International Academy of Astronautics, 2011.

- [8] L. J. DeLucas, "International Space Station," *Acta Astronautica*, vol. 38, no. 4, pp. 613-619, 1996.
- [9] E. C. Stone, "Stone, E. C., The Voyager mission through the Jupiter encounters," *Journal of Geophysical Research*, vol. 86, no. A10, pp. 8123-8124, 1981.
- [10] S. Langlois and L. Scolamiero, "European Space Technology Harmonisation Technical Dossier: Deployable Booms / Inflatable Structures (TEC-MS/2010/26/ln/SL)," European Space Agency, Noordwijk, The Netherlands, 2010.
- [11] Y. Tsuda, O. Mori, R. Funase, H. Sawada, T. Yamamoto, T. Saiki, T. Endo, K. Yonekura, H. Hoshino and J. Kawaguchi, "Achievement of IKAROS - Japanese deep space solar sail demonstration mission," *Acta Astronautica*, vol. 82, no. 2, pp. 183-188, 2011.
- [12] T. Sinn, P. Seefeldt, A. Riemer, S. Meyer, T. Sprowitz, R. Hahn, S. Reershemius, M. Zander, L. Tiedemann, K. D. Bunte, T. Cardone and D. Teti, "Design, Analysis and Testing of the ADEO Passive De-orbit Demonstrator," in *European Conference on Spacecraft Structures, Materials and Environmental Testing (ECSSMET)*, Toulouse, France, 2016.
- [13] NASA, "Explore James Webb Space Telescope," NASA, [Online]. Available: <http://jwst.nasa.gov/index.html>. [Accessed 20 05 2014].
- [14] S. R. Martin, S. Shaklan, S. Crawford, S.-C. Lee, B. Khayatin, D. Hoppe, E. Cady and P. D. Lisman, "Starshade optical edge modeling, requirements, and laboratory tests," *SPIE Optical Engineering+ Applications*, pp. 88641A-88641A, 2013.

- [15] N. Headquarters, "NASA Space Flight human-System Standard, Volume 2: Human Factors, Habitability, and Environmental Health, NASA-STD-3003," national Aeronautics and Space Administration, Washington, DC, USA, 2011.
- [16] T. Sinn and O. Doule, "Inflatable Structures for Mars Base 10, AIAA-2012-3557," in *42nd International Conference on Environmental Systems (ICES)*, San Diego, California, USA, 15 -19 July 2012.
- [17] M. M. Cohen, "Testing the Celentano Curve: An Empirical Survey of Predictions for human Spacecraft Pressurized Volume," in *38th International Conference on Environmental Systems*, San Francisco, CA, USA, 2008.
- [18] J. R. Cruz, A. Cianciolo, R. Powell, L. Simonsen and R. Tolson, "Entry, descent, and landing technology concept trade study for increasing payload mass to the surface of Mars," in *4th International Symposium on Atmospheric Reentry Vehicles and Systems*, 2005.
- [19] M. W. Thomson, "The Astromesh deployable reflector," *IEEE, Antennas and Propagation Society International Symposium*, vol. 3, 1999.
- [20] C. Rando, J. Callies, L. Scolamiero, C. Ashcroft and D. Binns, "Ultra-Stable Deployable Structures Working Group Report, TEC-SB/0063/DB," European Space Agency (ESA), ESTEC, Noordwijk, The Netherlands, 2012.
- [21] T. Sinn, M. McRobb, A. Wujek, J. Skogby, F. Rogberg, J. Wang, M. Vasile and G. Tibert, "Results of REXUS12's Suaineadh Experiment: Deployment of a spinning space web in micro gravity conditions," in *63rd International Astronautical Congress (IAC)*, Naples, Italy, 1-5 October 2012.
- [22] T. Sinn, H. Mao, M. McRobb, A. Wujek, J. Skogby, F. Rogberg, J. Wang, M. Vasile, G. Tibert and G. Tibert, "The Experiment that came from the Cold: Results from the Recovered REXUS12's SUAINEADH Spinning

- Web Experiment,” in *22nd ESA Symposium on European Rocket and Balloon Programmes and Related Research*, Tromso, Norway, 7-12 June 2015.
- [23] H. Mao, G. Tibert, T. Sinn and M. Vasile, “Post-Launch Analysis of the Deployment Dynamics of a Space Web Sounding Rocket Experiment,” *Acta Astronautica*, vol. 127, pp. 345-358, 2016.
- [24] T. Sinn, M. McRobb, A. Wujek, J. Skogby, F. Rogberg, J. Wang, M. Vasile and G. Tibert, “Lessons Learned from REXUS12’s Suaineadh Experiment: Spinning Deployment of a Space Web in Milli Gravity,” in *21st ESA Symposium on European Rocket and Balloon Programmes and Related Research*, Thun, Swizerland, 9-14 June 2013.
- [25] T. Sinn, M. McRobb, A. Wujek, J. Skogby, F. Rogberg, J. Weppler, M. Zhang, M. Vasile and G. Tibert, “REXUS 12 Suaineadh Experiment: Deployment of a web in microgravity conditions using centrifugal forces,” in *62nd International Astronautical Congress (IAC)*, Cape Town, South Africa, 3-7 October 2011.
- [26] T. Sinn, M. McRobb, A. Wujek, J. Skogby, M. Zhang, J. Weppler, A. Feeney, J. Russell, N. Smith, M. Daibri, M. Selin, C. Bergesjö, N. Hansen, F. Rogberg, J. Wang and H. Mao, “EuroLaunch Student Experiment Documentation (SED) RX12_SUAINETHD_SEDv5-3_11FEB14,” EuroLaunch, Kiruna, Sweden, 2014.
- [27] M. P. Cartmel and D. J. McKenzie, “A review of space tether research,” *Progress in Aerospace Sciences*, vol. 44, no. 1, pp. 1-21, 2008.
- [28] L. Stiles and H. Schnaub, “Electron Flux Deflection Experiments with Coulomb Gossamer Structures,” in *AIAA-2012-1583, 13th AIAA Gossamer Systems Forum as part of 53rd Structures, Structural Dynamics, and Materials and Co-located Conferences*, Honolulu, Hawaii, USA, 2012.

- [29] M. C. Bernasconi, "Flexible-wall expandable structures for space applications: forty years of trying," in *1st European Workshop on Inflatable Space Structures, 21-22 May*, Noordwijk, The Netherlands, 2002.
- [30] C. H. M. Jenkins, "Gossamer Spacecraft: Membrane and Inflatable Structures Technology for Space Applications," *Progress in Astronautics and Aeronautics*, vol. 191, 2001.
- [31] R. Freeland, G. Bilyeu, G. Vea and M. Mikulas, "Inflatable deployable space structures technology summary," in *49th International Astronautical Congress*, Melbourne, Australia, 1998.
- [32] M. C. Bernasconi, "Chemically rigidized expandable structures (CRES): rigidization and materials," Tivoli, Italy, 2004.
- [33] B. Defoort, "Polymerization of composite materials in free space environmen," Noordwijk, The Netherlands, 2008.
- [34] C. McInnes, M. Vasile, D. Bennett, C. Colombo, C. Lücking, W. van der Weg, F. Zuiani and T. Sinn, "Low-cost Inter-orbit Transfer Demonstrator," UK Space Agency's National Space Technology Programme (NSTP), London, UK, 2012.
- [35] M. Thomson, "Mechanical vs. Inflatable Deployable Structures for Large Aperatures or Still No Simple Answers," Pasadena, CA, USA, 2008.
- [36] B. Freeland, "Deployable Antenna Structures Technologies," Pasadena, CA, USA, 2008.
- [37] M. Lake, "A Vision for Reflector Technologies," in *Large Space Aperatures Workshop, 10-12 November*, Keck Institute for Space Sciences, Pasadena, CA, USA, 2008.
- [38] M. Straubel, "On-ground Rigidised, Inflatable CFRP Booms for Various

- Deployable Space Structures,” Noordwijk, The Netherlands, 2011.
- [39] M. Garcia, “BEAM Expands to Full Size,” NASA Blog, 28 05 2016. [Online]. Available: <https://blogs.nasa.gov/spacestation/2016/05/28/beam-expanded-to-full-size/>. [Accessed 17 08 2016].
- [40] T. Sinn and M. Vasile, “Deployment Simulation of Very Large Inflatable Tensegrity Reflectors,” in *62nd International Astronautical Congress (IAC)*, Cape Town, South Africa, 3 - 7 October 2011.
- [41] R. Clark, T. Sinn, I. Dolan, N. Donaldson, C. Lowe, D. G. Yarnoz, R. Brown, T. Parry, S. Bertrand, W. Munnoch, L. Colley, P. Hammond, A. Mahmood, R. Bewick, C. Lücking and M. Plecas, “EuroLaunch Student Experiment Documentation (SED), RX15_StrathSat-R2_SEDv5-1_09AUG13, 2013,” EuroLaunch, Kiruna, Sweden, 2013.
- [42] R. Clark, T. Parry, N. Donaldson, T. Sinn, R. Brown, C. Lowe, D. G. Yarnoz and P. Hammond, “StrathSat-R2: Deployable Structure Demonstrator on REXUS15,” in *22nd ESA Symposium on European Rocket and Balloon Programmes and Related Research*, Tromso, Norway, 7-12 June 2015.
- [43] T. Sinn and M. Vasile, “Design and development of a self-inflating adaptive membrane,” in *53rd Structural Dynamics and Materials Conference*, Honolulu, Hawaii, USA, 23 - 26 April 2012.
- [44] M. Neal, “Meteoroid damage to filamentary structures(Micrometeoroid impact fracture rates in wire, flat tapes, and thin-walled hollow tubes),” NASA technical reports, 1967.
- [45] D. a. S. S. Cadogan, “Rigidizable materials for use in gossamer space inflatable structures,” 2001.

- [46] D. C. C. Lichodziejewski, "Inflatable power antenna technology," Reno, Nevada, USA, 1999.
- [47] E. J. Simburger, "Development, design, and testing of powersphere multifunctional ultraviolet-rigidizable inflatable structures," *Journal of spacecraft and rockets*, vol. 42, no. 6, pp. 1091-1100, 2005.
- [48] F. Carpi, D. De Rossi, R. Kornbluh, R. E. Pelrine and P. Sommer-Larsen, *Dielectric elastomers as electromechanical transducers: Fundamentals, materials, devices, models and applications of an emerging electroactive polymer technology*, Elsevier, 2011.
- [49] Y. Bar-Cohen, "Electroactive Polymers as Artificial Muscles - Capabilities, Potentials and Challenges," in *Robotics 2000 and Space 2000*, Albuquerque, NM, USA, 2000.
- [50] M. Morimoto and I. Masahiro, "A diarylethene cocrystal that converts light into mechanical work," *Journal of the American Chemical Society*, vol. 132, no. 40, pp. 14172-14178, 2010.
- [51] C. Barrett, "Polymers containing azobenzene as photo-mechanical materials," *APS Meeting Abstracts*, vol. 1, p. 17011, 2007.
- [52] E. Patoor, D. Lagoudas, P. Entchev, L. Brinson and X. Gao, "Shape memory alloys: Part I: General properties and modelling of single crystals," *Mechanics of Materials*, vol. 38, no. 5-6, pp. 391 - 429, 2006.
- [53] W. Huang and W. Toh, "Training two-way shape memory alloy by reheat treatment," *Journal of Material Science Letters*, vol. 19, no. 17, pp. 1549-1550, 2000.
- [54] B. Jaffe, *Piezoelectric ceramics Vol. 3*, Elsevier, 2012.
- [55] B. Woods, E. Bubert, C. S. Kothera and N. Wereley, "Design and testing

- of biologically inspired pneumatic trailing edge flap system, AIAA-2008-2046,” in *AIAA Structures, Structural Dynamics, and Materials Conference*, Schaumburg, IL, USA, 2008.
- [56] N. Tsagarakis and D. G. Caldwell, “Improved modelling and assessment of pneumatic muscle actuators,” *Proceedings of IEEE International Conference on Robotics and Automation (ICRA)*, vol. 4, pp. 3641-3646, 2000.
- [57] R. Vos and R. Barrett, “Pressure adaptive honeycomb: a new adaptive structure for aerospace applications,” *SPIE Smart Structures and Materials; Nondestructive Evaluation and Health Monitoring*, vol. International Society for Optics and Photonics, pp. 76472B-76472B, 2010.
- [58] R. Vos and R. Barrett, “Method and apparatus for pressure adaptive morphing structure”. U.S. Patent 8,366,057, 05 February 2013.
- [59] R. V. Martinez, J. L. Branch, C. R. Fish, L. Jin, R. F. Shepherd, R. Nunes, Z. Suo and G. M. Whitesides, “Robotic Tentacles with Three-Dimensional Mobility Based on Flexible Elastomers,” *Advanced Materials*, vol. 25, no. 2, pp. 205-212, 2013.
- [60] R. F. Shepherd, F. Ilievski, W. Choi, S. A. Morin, A. A. Stokes, A. D. Mazzeo, X. Chen, M. Wang and G. M. whitesides, “Multigait soft robot,” *Proceedings of the National Academy of Sciences*, vol. 108, no. 51, pp. 20400-20403, 2011.
- [61] E. Hawkes, B. An, N. M. Benbernou, H. Tanaka, S. Kim, E. D. Demaine, S. Rus and R. J. Wood, “Programmable matter by folding,” *Proceeding of the National Academy of Sciences*, vol. 107, no. 28, pp. 12441-12445, 2010.
- [62] K. Gilpin, A. Knaian and D. Rus, “Robot Pebbles: One Centimeter Modules for Programmable Matter Through Self-disassembly,” *IEEE*, pp.

2485-2492, 2010.

- [63] M. Rubenstein, A. Cornejo and R. Nagpal, "Programmable self-assembly in a thousand-robot swarm," *Science*, vol. 345, no. 6198, pp. 795-799, 2014.
- [64] A. S. Gladman, E. A. Matsumoto, E. A. Nuzzo, R. G. Mahadevan and J. A. Lewis, "Biomimimetic 4D Printing," *Natural Materials*, vol. 15, pp. 413 - 418, 2016.
- [65] J. F. V. Vincent, "Deployable structures in nature: potential for biomimicking," *Proceeding of Institut of Mechanical Engineers (IMEchE)*, vol. 214, no. C, 2000.
- [66] N. Kishimoto, M. C. Natori, K. Higuchi and K. Ukegawa, "New deployable membrane structure models inspired by morphological changes in nature," *American Institute of Aeronautics and Astronautics*, vol. May, pp. 1-10, 2006.
- [67] J. W. Hart, *Plant tropisms: and other growth movements*, Springer, 1990.
- [68] C. W. Whippo and R. P. Hangarter, "Phototropism: bending towards enlightenment," *The Plant Cell Online*, vol. 18, no. 5, pp. 1110-1119., 2006.
- [69] T. Sinn and M. Vasile, "Bio-inspired programmable matter for space applications," in *63rd International Astronautical Congress (IAC)*, Naples, Italy, 1-5 October 2012.
- [70] C. Galen, "Sun Stalkers: How Flowers Follow The Sun," *American Museum of Natural History, ETATS-UNIS, New York, US*, vol. 108, no. 5, pp. 49-51, 1999.
- [71] N. Moran, G. Ehrenstein, K. Iwasa, C. Mischke, C. Bare and R. L. Satter, "Potassium Channels in Motor Cells of *Samanea saman* A Patch-

- Clamp Study,” *Plant physiology*, vol. 88, no. 3, pp. 643-648, 1988.
- [72] A. D. o. Biology, Encyclopedia.com, 2004. [Online]. Available: <http://www.encyclopedia.com>. [Accessed 13 04 2014].
- [73] R. J. Lang, “Mathematical algorithms for origami design,” *Symmetrz: Culture and Science*, vol. 5, no. 2, pp. 115-152, 1994.
- [74] R. J. Lang, “Robert J. Lang Origami Homepage,” [Online]. Available: <http://www.langorigami.com>. [Accessed 25 March 2014].
- [75] I. M. Mladenov, “New Geometrical Applications of the Elliptical Integrals: The Mylar Balloon,” *Journal of Nonlinear Math. Phys.*, vol. 11, pp. 55-65, 2004.
- [76] T. Sinn and M. Vasile, “Multibody Dynamics for Biologically Inspired Smart Space Structures,” in *AIAA Science and Technology Forum and Exposition (SciTech)*, National Harbour, Maryland, USA, 13 - 17 January 2014.
- [77] M. Paz and W. Leigh, *Structural Dynamics: Theory and Computation*, Springer, 2003.
- [78] A. K. Chopra, *Dynamics of Structures*, Upper Saddle River, New Jersey, USA: Pearson Education Inc., 2007.
- [79] R. A. Serway, *Physics for Scientists and Engineers*, second edition, Saunders College Publishing, 1986.
- [80] F. P. Beer, “Chapter 9.6: Parallel-axis theorem,” in *Vector Mechanics for Engineers (10th edition)*, New York, McGraw-Hill, 2013, p. 481.
- [81] P. A. Tipler, “Chapter 12: Rotation of a Rigid Body about a Fixed Axis,” in *Physics*, Worth Publishers, 1976.

- [82] COSPAR, "COSPAR International Reference Atmosphere 2012 - Models of the Earth's Upper Atmosphere," Committee on Space Research, Houston, 2012.
- [83] F. Haugen, "Article: Discretization of simulator, filter, and PID controller," TechTeach, 10 05 2010. [Online]. Available: <http://www.mic-journal.no/PDF/ref/Haugen2010.pdf>. [Accessed 03 10 2015].
- [84] T. Sinn, D. Hilbich and M. Vasile, "Inflatable Shape Changing Colonies Assembling Versatile Smart Space Structures," in *64th International Astronautical Congress (IAC)*, Beijing, China, 23 - 27 September 2013.
- [85] D. Hilbich, T. Sinn, B. Gray and S. Shannon, "Large Scale Thick Film Metallization of PDMS Enabling Flexible Electronics in Space Applications," in *65th International Astronautical Congress (IAC)*, Toronto, Canada, 29. September - 03 October 2014.
- [86] J. Mankins, N. Kaya and M. Vasile, "SPS-ALPHA: The first practical solar power satellite via arbitrarily large phased array (a 2011-2012 NASA NIAC project)," in *10th International Energy Conversion Engineering Conference*, Atlanta, GA, USA, 2010.
- [87] T. Sinn, "Smart Shape Changing Structures for Space Based Solar Power Applications, SGAC/IAF Space Solar Power Competition Winning Paper," in *65th International Astronautical Congress (IAC)*, Toronto, Canada, 29. September - 03. October 2014.
- [88] T. Sinn, D. Hilbich and M. Vasile, "Inflatable shape changing colonies assembling versatile smart space structures," *Acta Astronautica*, vol. 104, pp. 45-60, 2014.
- [89] N. J. P. Laboratory, "JPL Small-Body Database Browse: 99942 Apophis (2004 MN4)," NASA Jet Propulsion Laboratory, 07 12 2007. [Online].

Available: <http://ssd.jpl.nasa.gov/sbdb.cgi?sstr=99942;cad=1>. [Accessed 16 04 2016].

- [90] R. Clark, T. Sinn, I. Dolan, N. Donaldson, R. Brown, T. Parry, C. Lücking and R. Bewick, “StrathSat-R: Deploying inflatable CubeSat structures in micro gravity, IAC-12-E2.3.7,” in *63rd International Astronautical Congress (IAC)*, Naples, Italy, 1-5 October 2012.
- [91] N. Donaldson, T. Parry, T. Sinn, D. G. Yarnoz, C. Lowe and R. Clark, “Ejection and recovery system for CubeSat sized ejectables on sounding rockets,” in *64th International Astronautical Congress (IAC)*, Beijing, China, 23-27 September 2013.
- [92] I. Dolan, T. Sinn, R. Clark, N. Donaldson, C. Lowe, D. G. Yarnoz, R. Brown, T. Parry and S. Bertrand, “StarthSat-R: Deploying Inflatable Structures from Cubesats in Milli Gravity,” in *21st ESA Symposium on European Rocket and Balloon Programmes and Related Research*, Thun Switzerland, 9-14 June 2013.
- [93] S.-O. Inc, “Ecoflex Series Product Overview,” Smooth-On Inc., Easton, PA, USA, 2013.
- [94] T. Sinn, T. Bogicevic and M. Vasile, “Self-folding Smart Structure inspired by Nature's Heliotropism,” in *European Conference on Spacecraft Structures, Materials and Environmental Testing (SSMET)*, Braunschweig, Germany, 1 - 4 April 2014.
- [95] U. Geppert, B. Biering, F. Lura, J. Block, M. Straubel and R. Reinhard, “The 3-step DLR-ESA Gossamer road to solar sailing,” *Advances in Space Research*, vol. 48, no. 11, pp. 1695-1701, 2011.
- [96] K. Miura, “Method of packing and deployment of large membranes in space. IAF-80-31,” in *31st IAF Congress*, Tokyo, Japan, 1980.

- [97] T. Sinn, R. Brown, M. McRobb, A. Wujek, C. Lowe, J. Weppler, T. Parry, D. G. Yarnoz, F. Brownlie, J. Skogby, I. Dolan, T. de Franca Queiroz, F. Rogberg, N. Donaldson, R. Clark, A. Allan and G. Tibert, “Lessons learned from three university experiments onboard the REXUS/BEXUS sounding rocket and stratospheric balloons,” in *64th International Astronautical Congress (IAC)*, Beijing, China, 23-27 September 2013.
- [98] M. J. Andling, D. M. Hoyland, P. S. Cannon, P. Harkness, M. McRobb, M. Vasile and T. Sinn, “Wideband Ionospheric Sounder Cubesat Experiment: A precursor mission for low frequency space radar,” in *Beacon Satellite Symposium*, Bath, UK, 8 - 12 July 2013.
- [99] M. J. Angling, D. M. Hoyland, P. S. Cannon, P. Harkness, M. McRobb, M. Vasile and T. Sinn, “Wideband Ionospheric Sounder Cubesat Experiment (WISCER): Phase II study,” Poynting Institute, University of Birmingham, Birmingham, UK, 2013.
- [100] T. Sinn, T. d. F. Queiroz, F. Brownlie, L. Leite, A. Andrew, A. Rowan and J. Gillespie, “iSEDE demonstrator on high altitude balloon BEXUS: Inflatable satellite encompassing disaggregated electronics,” in *64th International Astronautical Congress (IAC)*, Beijing, China, 23-27 September 2013.
- [101] T. Sinn, T. de Franca Quiroz, F. Brownlie, L. Leite, A. Allan, A. Rowan and J. Gillespie, “Results of the iSEDE Experiment Encompassing Disaggregated Electronics on an All Inflatable Satellite Onboard the BEXUS16 Balloon,” in *22nd ESA Symposium on European Rocket and Balloon Programmes and Related Research*, Tromso, Norway, 7 - 12 June 2015.
- [102] T. Sinn, T. de Franco Queiroz, F. Brownlie, L. B. Leite, A. Allan, J. Gillespie and A. Rowan, “EuroLaunch Student Experiment Documentation (SED), BX16_iSEDE_SEDv5-1_31JAN14,” EuroLaunch, Kiruna, Sweden,

2014.

- [103] D. Werner, "Space Ground Amalgam LLC -Adjusted for Inflation," *Space News International*, p. 16, 2012.
- [104] D. Werner, "Bigelow Aerospace: Inflatable Modules for ISS," Space.com, 24 01 2013. [Online]. Available: <http://www.space.com/19311-bigelow-aerospace.html>.
- [105] E. B. Wilson, "The Heliotropism Of Hydro," *The American Naturalist*, vol. 25, no. 293, pp. 413-433, 1891.
- [106] W. J. Larson and J. R. Wertz, Space mission analysis and design (No. DOE/NE/32145-T1), Torrance, CA, USA: Microcosm, Inc., 1992.
- [107] E. F. Crawley, "Intelligent structures for aerospace: a technology overview and assessment," *AIAA Journal*, vol. 32, no. 8, pp. 1689-1699, 1994.